UNIVERSITY OF CALIFORNIA
RIVERSIDE

Self-Assembly of Viral Particles

A Dissertation submitted in partial satisfaction
of the requirements for the degree of

Doctor of Philosophy

in

Physics

by

Siyu Li

June 2019

Dissertation Committee:

Dr. Roya Zandi, Chairperson
Dr. Leonid Pryadko
Dr. Umar Mohideen

The Dissertation of Siyu Li is approved:

Committee Chairperson

University of California, Riverside

Acknowledgments

I am very grateful to my advisor Roya Zandi and appreciate everything I have learned from her. The path to getting a Ph.D. in Physics is very hard, especially for female students. I had a lot of self-doubts and moments questioning my goals in life. Thanks to Roya, she offered me useful advice and helped me to choose the right path, without her, I would not have been here.

I would also like to express my deep thank to Gonca Erdemci-Tandogan, who speeded up the nucleation rate of my work, and Jef Wagner, whose beautiful algorithm dramatically lowered down my research energy barrier.

I would also like to thank Prof. Alex Travesset, Prof. Gregory M. Grason, Prof. Paul van der Schoot and Prof. Henri Orland, who gave me numerous suggestions and excellent feedbacks for the projects.

Additionally, I would like to thank Sanaz Panahandeh, Yinan Dong and Haoshan Zhu, without them my graduate life would be extremely boring.

Last but not least, the deepest appreciation to my parents, for their supporting and understanding all the time.

List of Publications

- Li, S., Erdemci-Tandogan, G., Wagner, J., van der Schoot, P. and Zandi, R. (2017). Impact of a nonuniform charge distribution on virus assembly. *Phys. Rev. E*, 96(2), 022401.

- Li, S., Erdemci-Tandogan, G., van der Schoot, P. and Zandi, R. (2017). The effect of RNA stiffness on the self-assembly of virus particles. *Journal of Physics: Condensed Matter*, 30(4), 044002.

- Li, S., Orland, H. and Zandi, R. (2018). Self consistent field theory of virus assembly. *Journal of Physics: Condensed Matter*, 30(14), 144002.

- Li, S., Roy, P., Travesset, A. and Zandi, R. (2018). Why large icosahedral viruses need scaffolding proteins. *Proceedings of the National Academy of Sciences*, 115(43), 10971.

- Panahandeh, S., Li, S. and Zandi, R. (2018). The equilibrium structure of self-assembled protein nano-cages. *Nanoscale*, 10, 22802.

- Li, S., Zandi, R. and Travesset, A. (2019). Elasticity in Curved Topographies: Exact Theories and Linear Approximations. *Phys. Rev. E*, in Press.

- Li, S., Travesset, A., Zandi, R. and Grason, G. M. (2019). Ground States of Crystalline Caps: Generalized Jellium on Curved Space. Submitted to *Phys. Rev. Lett.*

To my parents for all the support.

ABSTRACT OF THE DISSERTATION

Self-Assembly of Viral Particles

by

Siyu Li

Doctor of Philosophy, Graduate Program in Physics
University of California, Riverside, June 2019
Dr. Roya Zandi, Chairperson

Small spherical viruses spontaneously encapsidate their genome into protein capsids. The encapsidation free energy and genome profile have been extensively studied using field theory techniques with Ground State Dominance Approximation (GSDA). In the thesis we employ the self-consistent field theory (SCFT) to calculate the exact genome field confined in a spherical viral shell and examine the validity of GSDA. Furthermore, we study the impact of N-terminal domains of capsid proteins and the secondary structure of RNA on the assembly efficiency in the regions where GSDA is valid. Additionally, we investigate the origin of icosahedral order (IO) of viral capsids. It is believed that large viruses grow their pentamers on IO vertices through an irreversible pathway. Using continuum elasticity theory, we study the growth of spherical cap with a stress-free boundary. We show that for large viruses, the scaffolding proteins or an inner core are essential for the nonlinear geometry of the capsid. The combined effect of nonlinearity and the free edge of the cap conspire to give rise to the configurations with IO defects during the assembly pathway.

Contents

List of Figures

Part I

Introduction

Chapter 1

Introduction

1.1 Virus

Simple viruses consist of a protein capsid and the genomic material, either RNA or DNA. Some viruses, such as retrovirus HIV-1, may contain an envelope of lipids protecting their capsids. Viruses are categorized based on different factors: from the architecture point of view, viruses may have cylindrical shape (tobacco mosaic virus, as shown in Fig. 1.1a), spherical shape (cowpea chlorotic mottle virus in Fig. 1.1b), or conical shape (human immunodeficiency viruses, Fig. 1.1c); from the type of the genome viruses are distinguished as single stranded (ss) RNA, double stranded (ds) RNA, ssDNA and dsDNA. Other factors can further be considered as the classification factors. Examples include the host kind, the use of reverse transcriptase in replication, the existence of envelope and so on.

The life cycle of viruses includes adsorption, entry, transcription, assembly and release. Upon entry into the cell, the virus disassembles and releases the genome, which replicates and synthesizes identical capsid proteins. The new generated proteins sponta-

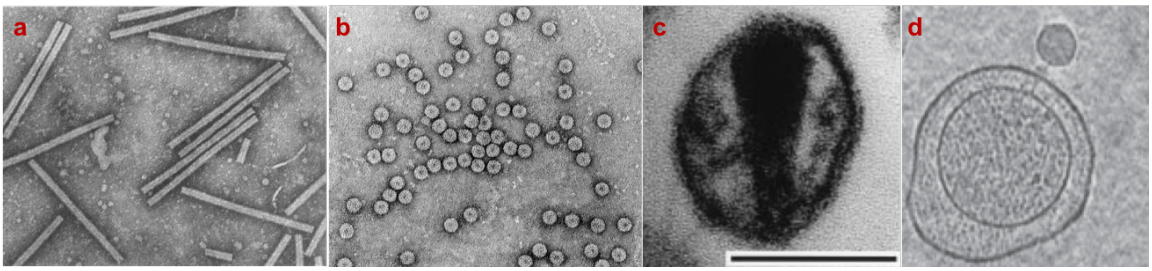

Figure 1.1: Cryo microscopy images of (a) tobacco mosaic virus (TMV) [1], (b) cowpea chlorotic mottle virus [2], (c) human immunodeficiency viruses (HIV) [3], and (d) bacteriophage P22 [4].

neously encapsidate the genome and co-assemble into new virions. One exception from this disassembly-assembly process is bacteriophage (Fig. 1.1d). Instead of endocytosis, it attaches to the cell receptor and injects its DNA into the cytoplasm. In the assembly process, the phage capsid proteins copolymerize with scaffolding proteins and form the empty capsid called prohead, the DNA is then packed afterward during the maturation process.

Considerable theoretical works have been done to decipher the mystery of the virus life cycle. Among those, elasticity theory has shed light on virus entry and the architecture of viral capsids [13–15], and polymer physics is widely applied for genome configuration in the co-assembly process [16–18]. In addition, classical nucleation theory and thermodynamics have been extensively used and provided a powerful physical tool to investigate the equilibrium and kinetic pathway of virus assembly [19, 20].

Although the life cycles vary in different families of viruses, there are two things universal, which are the focus of the thesis: (1) the self-assembly in case of RNA viruses, and (2) the icosahedral order (IO) in spherical viral capsids.

1.2 Self Assembly

Many small single-stranded RNA or ssRNA viruses have been shown to spontaneously self-assemble *in vitro*, which is, outside living cells in solutions containing virus coat protein subunits and genome. In this process the capsid proteins encapsidate genome (RNA or DNA) to a stable, protective shell. In fact, virus coat proteins are able to co-assemble with a variety of cargos, including RNAs of other and sometimes unrelated viruses, synthetic polyanions, and negatively charged nanoparticles [21–23]. The spontaneous assembly of properly structured viral capsids is due to the electrostatic interaction between the positive charges present on protein subunits and the negative charges of the cargos [24–31]. This encapsidation feature has made viruses ideal for various bio-nanotechnological applications including gene therapy and drug delivery.

Experimental and theoretical studies have shed light on the physical factors contributing to the efficient assembly and stability of small virus particles.

The self-assembly studies of Comas-Garcia *et al.* [32] reveal in particular the importance of RNA topology in packing efficiency. *In vitro* experiment features the role of pH and salt concentration in CCMV assembly [33]. In particular, X-ray scattering is being used to uncover the self-assembly pathways viral capsids packaging either RNA genome or other polyelectrolytes [34], and fluorescence spectroscopy has been applied to monitor RNA conformation which indicates a two-stage process in bacteriophage MS2 assembly [35].

Meanwhile, field-theoretic calculations have investigated the impact of RNA secondary structure, annealed branching, on the length of the encapsidated polymer [17, 36]. Simulations on encapsulation of polymers with a quenched level of RNA branching have

shown that the assembly efficiency is a sensitive function of the secondary and tertiary structures of the RNA [16, 37].

Unlike small ssRNA viruses, the assembly process of large viruses is more complicated due to the considerable amount of protein subunits. Instead of co-assembly of capsid proteins and genome, large viruses typically require scaffolding proteins to form their capsids. For example, bacteriophage P22 assemble to a pro-head in the presence of scaffolding proteins, the virus maturation is triggered after the capsid formation which followed by the DNA injection [38, 39]. Similarly, dsRNA virus infectious bursal disease virus (IBDV), belonging to birnaviridae, is built by VP2 with the help of scaffolding proteins VP3 [40], in the absence of VP3, no capsid could be constructed. Another family, reoviridae (bluetongue virus for instance), form multiple shells, where the assembly of the VP7 outer layer relies on the preformation of scaffolding VP3 inner layer [41]. Interestingly, an evolutionary connection has been suggested between birnaviridae and reoviridae, indicating a universal mechanism for large virus assembly [42].

1.3 Triangulation Number

While the sizes of the small and large viruses vary from 20nm to 100nm, the universal icosahedral order (IO) is quite unexpected. To faciliate the understanding of virus IO, Capsar and Klug built the model of viral capsid with triangulation (T) number, where the proteins occupy the so-called "quasi-equivalent" environment on the capsid. Intuitively, triangulation number is the number of triangles on each icosahedron's face. Indeed, triangulation number with $T = 1^2,\ 2^2 .. \ n^2$ can be sketched by subdividing the "big" face of

icosahedron, as shown in Fig. 1.2a. However, this simple construction could not include all icosahedral symmetric shells. A more generalized way, as proposed by Capsar and Klug, is to map an icosahedral triangle face on a triangular lattice, illustrated in Fig. 1.2b. The triangulation number is therefore $T = h^2 + hk + k^2$ where h and k are the lattice coordinates followed in the two axes. The example of T=3 capsid is shown in Fig. 1.2c,d, where the net image of an icosahedron is mapped on the triangular and hexagonal lattice correspondingly.

Note that the triangular sheet (Fig. 1.2c) is usually used when the trimers are the subunits of the capsid, where each trimer consist of three identical proteins and the total protein number is 60T. Other than trimers, some viruses may assemble with dimers or hexamers (capsomers) as the building block (Fig. 1.2d). In these viruses, the number of capsomers is $10T + 2$, which one probably familiar in many virus assembly articles.

The comparison of the triangulation model and the viral capsid structure is shown in Fig. 1.3. Since triangulation number is proportional to the capsid protein number, which spreads on the capsid surface, T number is often scaled as the capsid area, and therefore the radius has the relation $R \sim \sqrt{T}$.

Extensive works have been done to explain why viral capsid form IO. Using capsomers (pentamer and hexamers) as building blocks, Zandi *et al.* [15] performed a series of Monte Carlo simulations and revealed that IO is a natural consequence of the free energy minimization. Similarly, Panahandeh *et al.* [43], using trimers as subunits, found IO is the dominant symmetry when investigating the minimum energy nano cages. Other than the equilibrium structures, Wagner *et al.* [44] employed a minimal model to investigate the kinetic growth of a virus. Their results show even following the local minimum energy

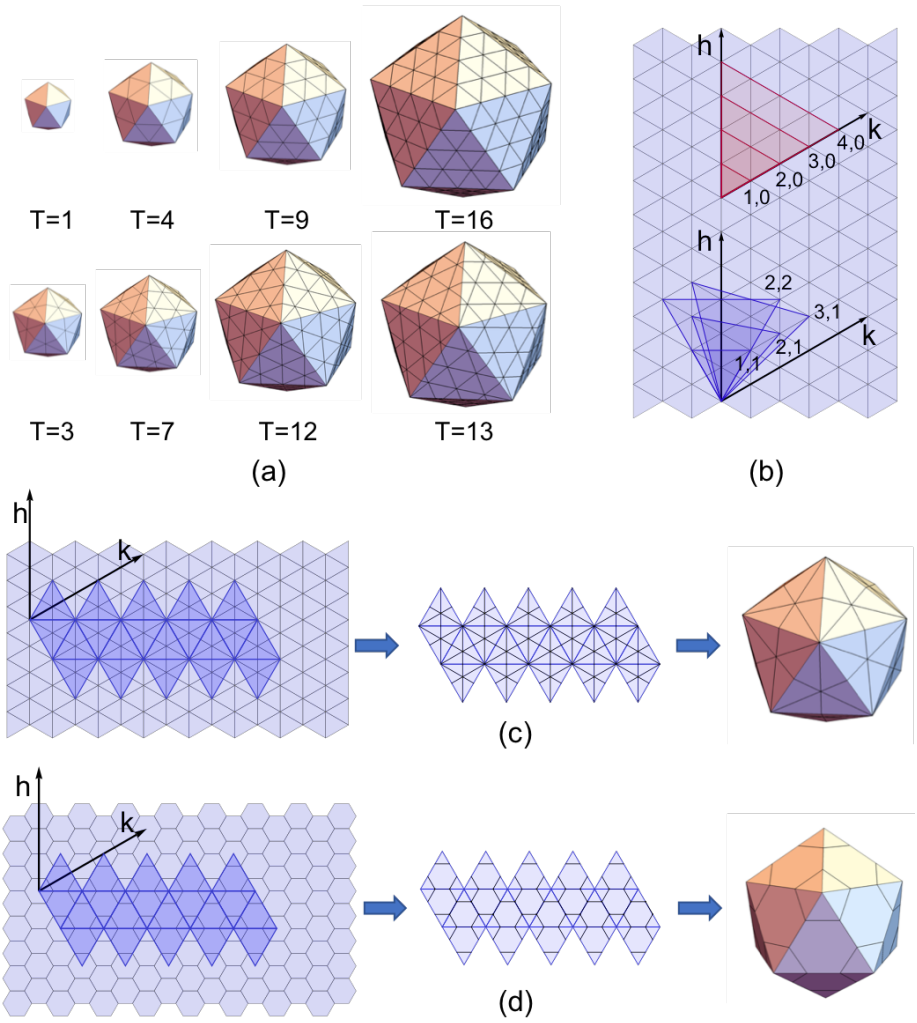

Figure 1.2: Illustration of icosahedral symmetric capsid with different triangulation number. (a) Examples of $T = n^2$ capsids (upper) and other T numbers (lower) with triangular subunits. (b) Mappings of one icosahdron face on triangular sheet to retrieve $T = 1, 4, 9, 16$ (upper) and $T = 3, 7, 12, 13$ (lower). (c) Construction of a $T = 3$ capsid from a map of icosahdron net image on triangular sheet. (d) Construction of a $T = 3$ capsid from a map on hexagonal sheet.

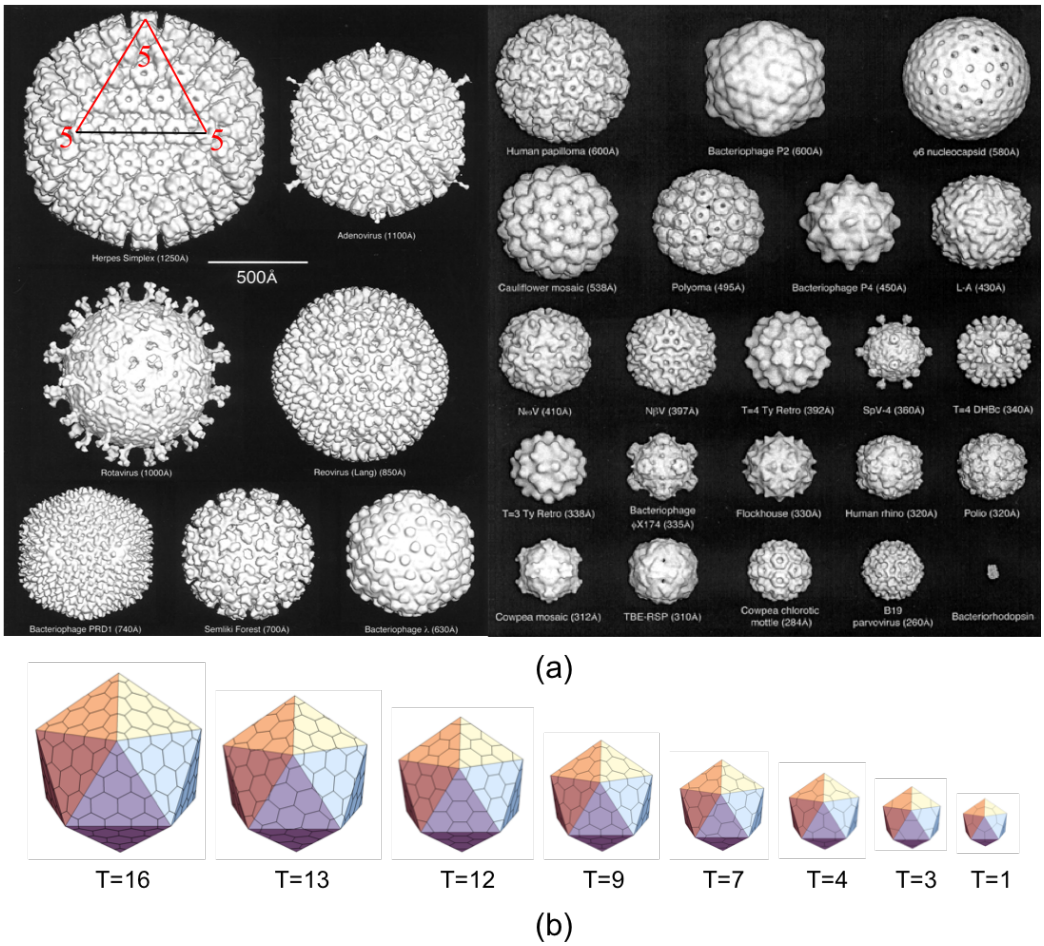

Figure 1.3: (a) Cryo microscopy images of spherical viruses [5] and (b) the icosahedral symmetric capsid models with different T number.

pathway, IO is still the prevalent symmetry.

In the co-assembly process of small viruses, genome plays an important role in presuming capsid with IO. For example, Hu et.al [45] showed that the length of genome controls the final capsid size, Krol et.al [46] observed that BMV CPs package natural BMV genome to T=3 but encapsidate engineered mRNA to a T=2 capsid. Additionally, Sun et al [21] showed that the purified BMV capsid proteins were able to encapsulate synthetic charged hard core to virus-like particles (VLP). With the modification of the core size, they observed variable sized VLPs with common icosahedral symmetries T=1, T=2 and T=3.

As counterparts in large viruses, scaffolding proteins or inner capsids perform the function in obtaining IO. For instance, bacteriophage P22 require copolymerization of gene 5 coat proteins and gene 8 scaffolding proteins to build T=7 proheads [38,39], the absence of scaffolding proteins would result in aberrant structures, either smaller T=4 shapes or large spirals. IBDV as mentioned previously, form T=13 shell in the presence of the scaffolding protein, without the helper protein, the capsid proteins can only assemble to T=1 subviral particles [42]. Other than preserving the IO, the scaffolding proteins also act as an initiator to speed up CPs aggregation. The bluetongue viruses, for example, do not assemble in the absence of T=2 inner capsid [41].

While the experiments have put forward in exploring their roles, how genome, scaffolding proteins or cargos regulate the virus assembly and what is the universal mechanism underlying virus assembly to assume an icosahedral structure are still unknown. To remedy this, we use the field theory and elasticity theory, combined with numerical and simulation skills, to study the process of virus assembly.

The thesis is arranged as follows. In part II we use the field theory to investigate the self-assembly of a virus particle. In chapter 2, we use self-consistent field theory to solve the exact encapsidation free energy, and investigate the validity of ground state dominance approximation (GSDA) used in many virus papers. In chapter 3 and 4, we apply the GSDA to explore the impact of nonuniform charged capsid and genome stiffness on the efficiency of virus assembly. In part III we focus on the icosahedral symmetry of viral capsid. We generalized the classical continuum elasticity theory to incorporate the spherical manifold in Chapter 5, then we use the elastic energy to investigate the growth pathway and find that the disclinations (pentamers) appear consequently in an icosahedral order as a result of the geometry nonlinearity. Finally, in conclusion part we summarize everything and raise up many open questions to be solved in the future.

Part II

Field Theory of Virus Assembly

Chapter 2

Self consistent field theory on virus assembly

2.1 Introduction

Viruses have evolved to optimize the feat of genome packaging inside a nano-shell called the capsid, built from several copies of either one or a few different types of proteins. Quite remarkably, under many circumstances the capsid proteins of single-stranded RNA viruses can assemble spontaneously [16,21,24–28,47,48] around the cognate and non-cognate RNAs and other negatively charged cargos [21–23, 49, 50]. It is widely accepted that the electrostatic interaction is the main driving force for the assembly [24–31] and it is this feature that has made viruses ideal for various bio-nanotechnological applications including gene therapy and drug delivery.

Despite their great interest in biological and industrial applications, the physical

factors contributing to the efficient assembly and stability of virus particles are not well understood [44,51]. The difficulty emerges from the considerable number of variables in the system including the genome charge density, the persistence length, the surface geometry and the charge density of surface charges. The adsorption of genome to the inner wall of capsid, the interplay between long-range electrostatic and short-range excluded volume interactions and the issue of chain connectivity make the understanding of the problem quite challenging. The presence of salt makes the adsorption process even more complicated. The salt ions can screen the electrostatic interaction between the charges and modify the persistence length of the genome leading to a change in the profile of the genome in the capsid.

Because of the difficulties noted above, in all previous studies on the encapsidation of viral genome by capsid proteins, the ground state dominance approximation, in which only the lowest energy eigenstate of the system is considered, has been exclusively used [17, 18, 36, 52–55]. In this chapter, we investigate the validity of GSDA in different regimes as a function of salt concentration, genome charge density and surface charge density. Note that viral RNA is relatively long compared to the capsid inner radius. For example for many plant viruses, RNA is about 3000 nucleotides while the inner capsid radius is around 10 nm [32]. While it is well-known that GSDA works well for long chains [56], in many recent virus assembly experiments short pieces of RNA have been systematically employed, to study the impact of genome length on the virus stability and formation [57]. Thus the time is ripe to explore the conditions under which GSDA does not apply and self consistent field theory has to be solved to obtain the correct solution. Comparing the solutions of

SCFT and GSDA shows that GSDA is less accurate when the interaction of genome with the capsid wall is weak even if the genome is long.

2.2 Theory

In order to calculate the free energy of a virus particle in a salt solution, we model the capsid as a positively charged shell, in which a negatively charged flexible linear polymer (genomic RNA) is confined. Defining by N the number of monomers, N_+ the number of salt cations and N_- the number of salt anions, the partition function of the system can be written as

$$\begin{aligned} Z &= \sum_i^{N_+}\sum_i^{N_-} \frac{1}{N_+!}\frac{1}{N_-!} e^{\beta\mu N_+} e^{\beta\mu N_-} \int \mathcal{D}r_i^+ \mathcal{D}r_i^- \mathcal{D}r_s \exp\left\{ -\frac{3}{2a^2}\int_0^N ds\dot{r}_s^2 \right. \\ &\quad \left. -\frac{1}{2}\int dr dr' \hat{\rho}_m(r) u(r-r') \hat{\rho}_m(r') - \frac{\beta}{2}\int dr dr' \hat{\rho}_c(r) \upsilon_c(r-r') \hat{\rho}_c(r') \right\} \end{aligned} \tag{2.1}$$

where a is the Kuhn length of the monomers. We assume that the salt is monovalent (charge e per ion), and the charge per monomer is τ. The monomer density $\hat{\rho}_m(r)$ and the charge density $\hat{\rho}_c(r)$ are given by

$$\hat{\rho}_m(r) = \int_0^N ds\delta(r-r_s) \tag{2.2}$$

$$\hat{\rho}_c(r) = \rho_0(r) + \tau\int_0^N \delta(r-r_s)ds + e\left(\sum_i^{N^+} \delta(r-r_i^+) - \sum_i^{N^-} \delta(r-r_i^-) \right) \tag{2.3}$$

where $\rho_0(r)$ denotes the charge density of the viral shell. In Eq. (2.1), the term $u(r) = u_0\delta(r)$ represents Edwards's excluded volume interaction, and $\upsilon_c(r) = 1/4\pi\epsilon r$ is the Coulomb interaction between the charges, where ϵ is the dielectric permitivity of the solvent.

2.2.1 Self Consistent Field Theory

To obtain the genome profile inside the virus capsid, we use Self-Consistent Field Theory (SCFT [58]) and the grand canonical ensemble for the salt ions with their fugacity λ corresponding to the concentration of salt ions in the bulk. Performing two Hubbard-Stratonovich transformations and introducing the excluded volume field $w(r)$ and the electrostatic interaction field ϕ (see Appendix A.1), Eq. 2.1 simplifies to

$$\mathcal{Z} = \int \mathcal{D}w(r)\mathcal{D}\phi(r) e^{\log Q - \int dr\{\frac{1}{2u_0}w^2(r) + \frac{\beta\epsilon}{2}(\nabla\phi(r))^2 - 2\lambda\cosh(i\beta e\phi(r)) + i\beta\rho_0(r)\phi(r)\}}$$

where Q denotes the partition function for a single chain

$$Q = \int \mathcal{D}r_s e^{-\frac{3}{2a^2}\int_0^N ds\dot{r}_s^2 - i\int dr\hat{\rho}_m(r)[w(r)+\beta\tau\phi(r)]}. \tag{2.4}$$

The Self-Consistent Field Theory equations are obtained by performing the saddle-point approximation on the two integration fields w and ϕ, see Appendix A.1. The equations are

$$w(r) = u_0\rho_m(r) \tag{2.5}$$

$$-\epsilon\nabla^2\phi = -2\lambda e\sinh(\beta e\phi(r)) + \rho_0(r) + \beta\tau\rho_m(r) \tag{2.6}$$

where

$$\rho_m(r) = \int_0^N ds\ q(r, N-s)q(r,s) \tag{2.7}$$

is the monomer concentration at point r. Equation 2.6 is the Poisson-Boltzmann equation for the charged monomers-salt ions system [59].

In Eq. 2.7, we have introduced the propagator $q(r,s)$, which is proportional to the probability for a chain of length s to start at any point in the viral shell and to end at point

r [60]. It satisfies the SCFT (diffusion) equation [61],

$$\frac{\partial q(r,s)}{\partial s} = \frac{a^2}{6}\nabla^2 q(r,s) - V(r)q(r,s) \tag{2.8}$$

$$V(r) = w(r) + \beta\tau\phi(r) \tag{2.9}$$

with the following boundary condition

$$q(r,0) = \frac{1}{\sqrt{Q}} \tag{2.10}$$

for r anywhere in the virus shell. The single chain partition function Q is given in Eq. 2.4 and is determined through the normalization condition on $q(r,s)$

$$\int_0^N dr q(r,N-s)q(r,s) = 1 \text{ for any } s \tag{2.11}$$

Note that the SCFT Eq. 2.8 can also be written as an imaginary time Schrödinger equation in the form

$$\frac{\partial q(r,s)}{\partial s} = -Hq(r,s) \tag{2.12}$$

with the Hamiltonian H given by

$$H = -\frac{a^2}{6}\nabla^2 + V(r) \tag{2.13}$$

Once we obtain the propagator q then we can calculate the chain persistence length or stiffness as explained in the next section.

2.2.2 Persistence Length

Polymers may have some bending rigidity or stiffness, due either to their intrinsic mechanical structure or to the Coulombic interaction between charged monomers, which has a tendency to rigidify the chain. This stiffness results in a strong correlation between

the orientation of successive monomers. Eventually, at large separations, the directions of monomers become uncorrelated. The persistence length of a polymer is the correlation length of the tangents to the chain [61,62]. It is the typical distance over which the orientation of monomers becomes uncorrelated. The chain can be viewed as a set of independent fragments of length equal to their persistence length.

In order to compute the persistence length, we calculate the correlation function of tangents to the chain

$$C(s,s') = \langle \dot{r}(s)\dot{r}(s')\rangle. \tag{2.14}$$

We show in Appendix that within the SCFT, this correlation function can be expressed as

$$C(s,s') \;=\; \frac{a^4}{9}\int dr dr' \left(\frac{\partial}{\partial r} q(r, N-s)\right)\left(\frac{\partial}{\partial r'} q(r', s')\right) \times \langle r|e^{-(s-s')H}|r'\rangle \tag{2.15}$$

where we assumed that $s > s'$. In this equation, for brevity we have used the standard quantum mechanical representation for the matrix elements of the evolution operator, see for example Eq. A.5, A.9, A.28 in Appendix.

For large separation $s - s' \gg 1$, this function behaves as

$$C(s,s') \approx e^{-(s-s')/l_p} \tag{2.16}$$

where by the above definition, l_p is the persistence length of the chain.

2.2.3 Ground State Dominance Approximation

The set of non-linear partial differential equations given in Eqs. 2.6, 2.8 are very tedious to solve. In the case of a confined chain, or more generally for a system with a gap in the energy spectrum of the Hamiltonian H, it is convenient to use the so-called Ground

State Dominance Approximation as noted in the introduction. This approximation consists of expanding the propagator q (Eq. 2.8) in terms of the eigenfunctions of the Hamiltonian H. We thus write

$$q(r,s) = \sum_{k=0}^{\infty} e^{-E_k s} q_k \psi_k(r) \tag{2.17}$$

where $\{E_k, \psi_k(r), k = 0, 1, 2, \ldots\}$ are the set of normalized eigenvalues and eigenstates of H, respectively,

$$\begin{aligned} H\psi_k(r) &= E_k \psi_k(r) \\ \int dr\ \psi_k^2(r) &= 1. \end{aligned} \tag{2.18}$$

Using the boundary condition Eq. 2.10, we find

$$q_k = \frac{1}{\sqrt{Q}} \int dr \psi_k(r) \tag{2.19}$$

with

$$Q = \sum_{k=0}^{\infty} e^{-NE_k} \left(\int dr \psi_k(r) \right)^2 \tag{2.20}$$

We assume that the eigenvalues are ordered as $E_0 < E_1 < \ldots < E_k < \ldots$. When the energy gap between the ground state E_0 and the first excited state E_1 is large, the ground state dominates the expansion Eq. 2.17 and we may write

$$q(r,s) = e^{-E_0 s} \left(q_0 \psi_0(r) + e^{-s\Delta} R(r,s) \right) \tag{2.21}$$

where $\Delta = E_1 - E_0$ is the energy gap, and the function $R(r,s)$ is the remainder of the expansion. When $s\Delta \gg 1$, the second term above becomes exponentially negligible, and we may write

$$q(r,s) = e^{-E_0 s} q_0 \psi_0(r) \tag{2.22}$$

and then Eqs. 2.20, 2.19 and 2.7 become respectively equal to

$$Q = e^{-NE_0} \left(\int dr \psi_0(r) \right)^2 \tag{2.23}$$

$$q_0 = e^{NE_0/2} \tag{2.24}$$

$$\rho_m(r) = N\psi_0^2(r) \tag{2.25}$$

The Poisson-Boltzmann (Eq. 2.6) and diffusion (Eq. 2.8) equations then become

$$-\epsilon\nabla^2\phi = -2\lambda e \sinh(\beta\phi) + N\tau\psi_0(r)^2 + \rho_0$$

$$-\tfrac{a^2}{6}\nabla^2\psi_0(r) + Nu_0\psi_0(r)^3 + \beta\tau\phi(r)\psi_0(r) = E_0\psi_0(r) \tag{2.26}$$

and the energy E_0 is determined so that ψ_0 is normalized as

$$\int dr \ \psi_0^2(r) = 1 \tag{2.27}$$

Similarly, we can compute the correlation function Eq. 2.15 within the GSDA. Using Eq. 2.24 and the fact that

$$\langle r|e^{-(s-s')H}|r'\rangle = e^{-(s-s')E_0}\psi_0(r)\psi_0(r') \tag{2.28}$$

in GSD, we obtain

$$\begin{aligned} C(s,s') &= \frac{a^4}{9}\left(\int dr \psi_0(r) \frac{\partial \psi_0}{\partial r} \right)^2 \\ &\equiv 0 \end{aligned} \tag{2.29}$$

since the integral is identically 0. We conclude that in the GSDA, the persistence length vanishes. In order to have a non-vanishing persistence length, we need to include more than the ground state in the eigenstate expansion of all quantities. Including the next

leading order term (first excited state with energy E_1 and wave function ψ_1), we obtain (see Appendix A.2)

$$C(s,s') \approx A_1 e^{-|s-s'|\Delta} + A_2 e^{-(N-|s-s'|)\Delta} \tag{2.30}$$

which shows that the persistence length is the inverse of the gap

$$l_p = \frac{1}{\Delta} \tag{2.31}$$

The persistence length can be computed using the GSDA as it follows: having solved the GSD Eqs. 2.26, we know E_0, $\psi_0(r)$ and $\phi(r)$ from which we can calculate $q(r,s)$ and the Hamiltonian H. We can then compute the first excited state of H with energy E_1, and then the persistence length l_p from Eq. 2.31.

2.3 Results

Due to the complexity of the problem, we numerically solve the non-linear coupled equations given in Eqs. 2.6 and 2.8. We consider two different cases for the interaction of genome with the capsid. First we study the adsorption of the chain to the capsid inner wall in the absence of the electrostatic interactions, as explained in section III A below. This way we decrease the number of parameters in the system, which helps us to gain some insights before solving the full problem. Then in section III B, we assume that both the capsid and chain are charged in salt solution.

2.3.1 Confined RNA with Adsorption on Capsid

We consider the confined RNA adsorbed on the capsid wall with no electrostatic interaction present. Thus, the external field (V_{ext}) in Eq. 2.8 contains only the excluded

volume interaction between monomers(u_0), with an extra attraction from the capsid γ_s. To solve the diffusion Eq. 2.8 with this surface term is not trivial, the strategy we introduce therefore is the effective boundary condition [63]:

$$\left[\frac{\partial}{\partial r}q(r,s) - \kappa q(r,s)\right]_{r=R} = 0 \tag{2.32}$$

where κ^{-1} is the extrapolation length and is proportional to the inverse of γ_s.

We employ both SCFT and GSDA to solve the problem of a chain confined in an adsorbing spherical shell. To obtain the exact solutions for SCFT, we solve Eqs. 2.6 and 2.8 recursively until conditions in Eqs. 2.10, 2.11 and 2.32 are satisfied. We employ Crank-Nicolson scheme and Broyden method [64,65] to solve the relevant equations. For the approximative solutions of GSD, we operate on the coupled nonlinear equations (Eq. 2.26) with finite element method and deal with the convergence issue using Newton method.

The results of our calculations are presented in Fig. 2.1, which shows the confined RNA density profile as a function of r, the distance from the shell center, for various extrapolation length (κ^{-1}). The goal is to compare our findings obtained through GSDA and SCFT methods for both short and long RNAs. The dashed lines in Fig. 2.1 are obtained using GSDA while solid lines are calculated based on the SCFT method. As illustrated in the figure, GSD only makes a good approximation for long chains and/or short extrapolation lengths (strong adsorption regime or large κ). With short RNA or long extrapolation length(weak adsorption regime), GSDA profile deviates considerably from self-consistent profile. As illustrated in Fig. 2.1, for $N = 5000$ regardless of the strength of interaction κ^{-1}, the solutions of GSDA and SCFT match almost perfectly and completely cover each other. However, the agreement between the two methods becomes less for $N = 100$ and

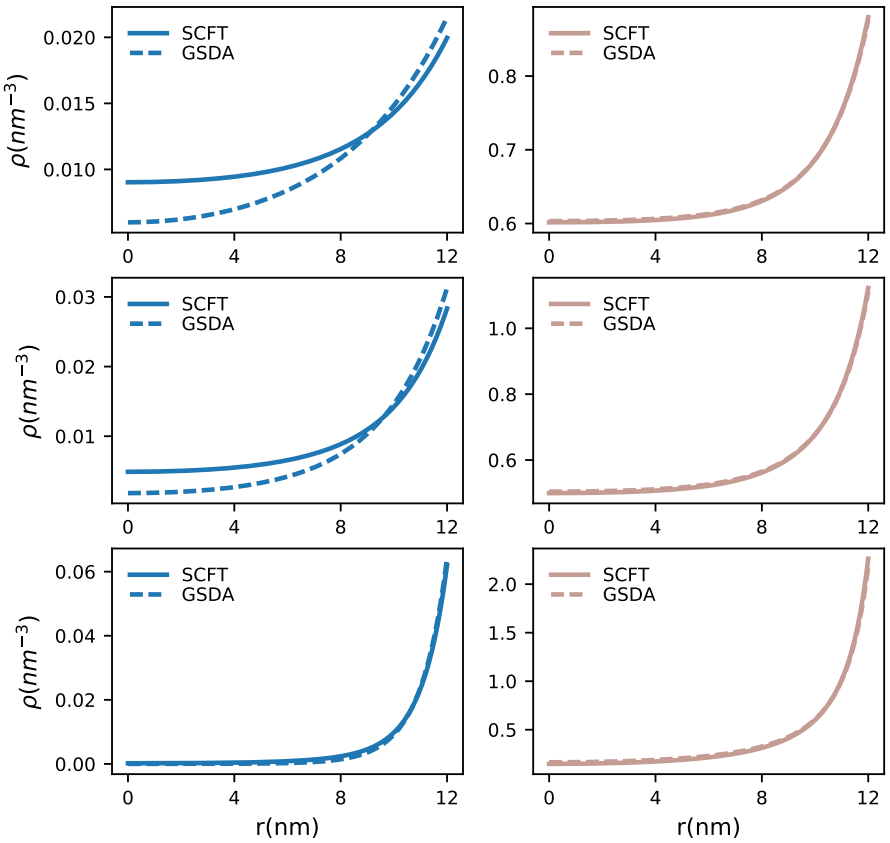

Figure 2.1: Confined RNA density profile vs r the distance from the capsid center for various extrapolation lengths, κ^{-1}=10.0, 5.0, 2.0 nm for top to the bottom of the figure. The total monomer number is N=100(left), N=5000(right).

small values of κ. In the next section, we investigate the impact of electrostatic interaction on the profile of RNA inside the capsid.

2.3.2 Confined RNA with Electrostatic Interaction

Since RNA acts like a negatively charged polyelectrolyte in solution, we need to take into consideration the electrostatic interactions term $\beta\tau\phi(r)$ given in Eq. 2.8. We assume that positive charges on the capsid are uniformly distributed. The coulombic interaction does usually overwhelm other forces responsible for the adsorption of chain to the

wall, so instead of applying Robin boundary condition (Eq. 2.32) as in Sect. 2.3.1, we use Dirichlet boundary condition ($q(R, s) = 0$) for monomer density by assuming the V_{ext} is infinity beyond the capsid wall. The physical basis for this assumption is that RNA monomer has stiffness, and the excluded volume interaction between the capsid wall and the RNA is such that the density of RNA could never sit at the wall.

We then solve Eqs. 2.6 and 2.8 to obtain the RNA density through both GSDA and SCFT methods. The genome concentration profiles are shown in Fig. 2.2 for various RNA length (total monomer number), capsid charge density, chain charge density and salt concentrations. As expected, there is alway a perfect match between GSDA and SCFT for longer RNAs (large N), while for short RNAs (small N), the energy gap becomes considerable and important, with ground state less dominant in the whole expansion series (Eq. 2.17) and GSD approximation becomes less valid.

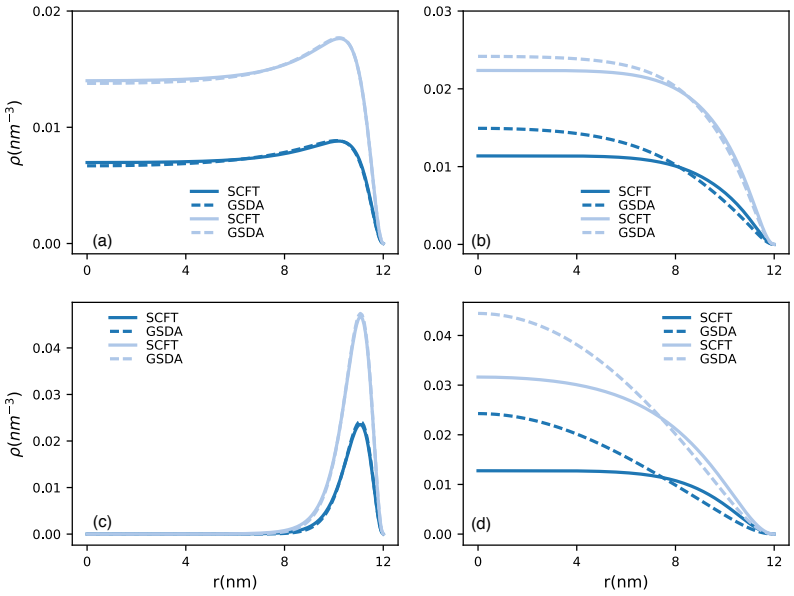

Figure 2.2: Confined RNA concentration profiles with various RNA length N=50(darker), N=100(lighter) under SCFT calculation(solid lines) and GSD approximation(dashed lines) with (a) linear chain charge density τ=-1.0e, capsid surface charge density σ=0.8e nm^{-2} and salt concentration λ=500mM; (b)τ=-1.0e, σ=0.4e nm^{-2} λ=500mM; (c)τ=-1.0e, σ=0.4e nm^{-2}, λ=100mM. (d)τ=-0.1e, σ=0.1e nm^{-2}, λ=100mM; Other parameters used are kuhn length a=1nm, excluded volume u_0=0.05nm^3, capsid radius R=12nm.

We also find that the stronger the electrostatic interaction due to the higher capsid surface charge density or genome linear charge density, the better GSDA and SCFT results agree with each other. Fig. 2.2a shows that regardless of length of genome, at high surface charge density, GSDA and SCFT give the same results. Note, as we decrease the surface charge density, their difference becomes noticeable, as illustrated in Fig. 2.2b. However, with lower salt concentration for the same surface charge density as in Fig. 2.2b, the difference between the two methods once again becomes negligible, Fig. 2.2c. Quite interestingly as we decrease the chain linear charge density even at low salt, we find again that the agreement between the two models becomes detectable, Fig. 2.2d.

All results presented above show that GSDA is less valid when genome localizes close to the center. To this end, we investigate this transition point where the wall attraction

becomes so weak that depletion shows up, corresponding to the disappearance of the genome peaks in graphs of Figs. 2.2a and b and also 2.4a and 2.4b below. We calculate the excess genome at the wall by integrating the genome peak area, which is proportional to adsorbed monomers. Then we investigate the impact of the salt concentration and surface charge density on the adsoprtion-depletion transition. The resulting phase diagram is illustrated in Fig. 2.3. The white shade in the figure corresponds to the maximum adsorption. As the color gets darker, less genome is adsorbed to the wall. In the darkest region there is no adsorption. The line separating the darkest region indicates the onset of the depletion transition.

Figure 2.4 describes the genome profile details for two different cases. For a fixed salt concentration but varying surface charge density ($\sigma = 0 - 0.4\, e\,\mathrm{nm}^{-2}$) we observe that the peak next to the wall slowly disappears as the capsid charge density decreases and most of the genome becomes localized at the center, Fig. 2.4a. Similar behavior is displayed in Fig. 2.4b for fixed surface charge density but various salt concentrations. Figs. 2.4a and 2.4b together tell us that the higher salt concentration, or the lower surface density charge, causes genome to stay away from the capsid wall and to localize toward the center, constructing the region where GSDA is not valid any more.

2.4 Discussion and Summary

The results of previous sections show that the GSDA validity depends on the genome localization: when the genome is absorbed on the wall, GSDA works perfectly,

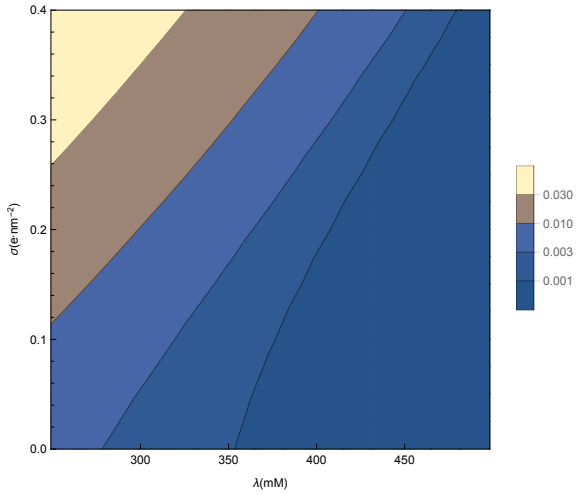

Figure 2.3: Genome excess phase diagram with respect to salt concentration and capsid surface charge density. The white shade corresponds to the region with the maximum genome density and black to the depletion regime next to the wall. Other parameters used are $N = 500$, a=1nm, u_0=0.05nm^3, R=12nm.

however when the adsorption becomes weaker and the genome starts moving to the center, GSDA stops being reliable. Fig. 2.2 illustrates this statement, where perfect match between GSDA and SCFT is obtained in lower salt concentration and higher surface charge (localized genome); significant deviation appears at higher salt concentration and lower surface charge in which case the genome is delocalized. The same effect is observed for the linear charge density of short genomes.

For longer genome with 500 monomers or more, the difference is almost undetectable. Quite interestingly, the effect of the electrostatic interaction range and strength, salt concentration and surface charge density in Sect. III B is similar to that of the extrapolation length in Sect. III A. While low salt concentration (longer Debye length, strong attraction) and high surface charge correspond to larger κ, high salt concentration (short Debye length, weak attraction) and low surface charge on the contrary correspond to small κ in which case the GSDA does not work well as illustrated in Fig. 2.1.

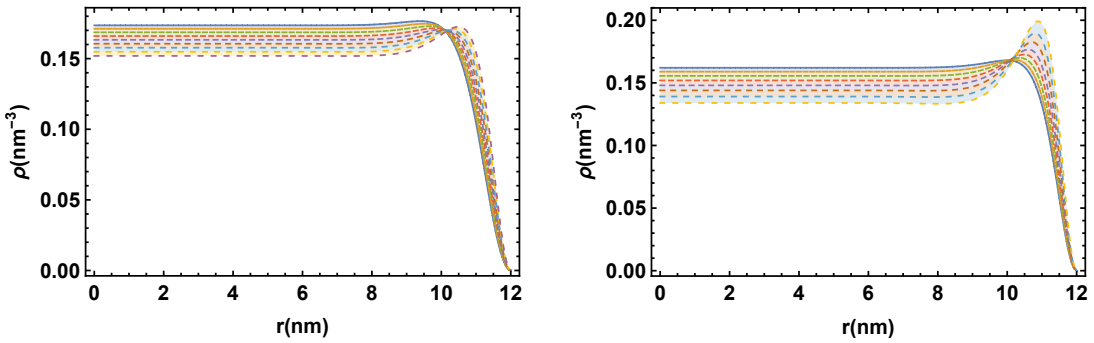

(a) (b)

Figure 2.4: Genome density profile for $N = 1000$ and (a) various surface charge density (0-0.4 $e\,\mathrm{nm}^{-2}$) with salt concentration λ=400mM; (b) various salt concentration(250-500 mM) with fixed surface charge $\sigma = 0.4e\,\mathrm{nm}^{-2}$. Other parameters correspond to kuhn length a=1nm, excluded volume u_0=0.05nm^3, capsid radius R=12nm.

Another important difference arising from using GSDA and SCFT approaches corresponds to the tangent-tangent correlation function or persistence length of the polymer. While the persistence length obtained through GSDA is zero, the persistence length calculated using SCFT is inversely proportional to the energy gap between the ground state and the first excited state, Eq. 2.31. The vanishing persistence length in GSDA is due to the fact that the chain constraint or connectivity is absent, and all monomers are independent. In the case of SCFT, the persistence length increases with the length of genome until it saturates to a finite value. Then indeed, as N increases, $l_p \ll N$, explaining again why GSDA becomes more and more valid as the length of the genome increases.

While the persistence length corresponds to the stiffness of the polymer, there is another important length scale in the problem but it is associated with the adsorption of polymer on the inner shell of the capsid. The adsorption of polymers to flat surfaces have been thoroughly studied, but the adsorption to spherical shells is less understood [66–69]. In case of flat surfaces, the Edward's correlation length determines the distance from the

wall over which the adsorption layer decays. It goes as $\xi \sim 1/\sqrt{u_0\phi_B}$, with u_0 the strength of the excluded volume and ϕ_B the bulk polymer density.

The situation studied in this chapter is more complex due to the confinement of the polymer inside a spherical capsid in the presence of electrostatics. Quite interestingly, Fig. 2.4(a) and (b) show there is a point around $r = 10$ where all the curves cross. According to the figure, the location of the crossing point does not depend on the salt concentration and capsid charge density. Since the capsid is a closed shell, we cannot define the bulk density in this problem. However, ϕ_B is related to the number of monomers in the capsid. Figures 2.5(a) and (b) illustrate the genome profiles for the same parameters as in Figs. 2.4(a) and (b) respectively but using a shorter genome length. The genome length is $N = 100$ and $N = 1000$ in Figs. 2.5 and 2.4, respectively. As illustrated in Figs. 2.5 all the plots again meet at a particular point but the position of the crossing point is moved compared to Fig. 2.4. It is interesting that despite different capsid charge density and salt concentration, all curves again meet at a unique single distance from the wall.

We also checked the position of the crossing point as a function of the excluded volume interaction expressed through the Edward's correlation length $\xi \sim 1/\sqrt{3u_0\phi_B}$. Our numerical results did not show any dependence of the crossing point on the strength of the excluded volume interaction. This is probably due to the fact that ϕ_B in this problem is not really the bulk density and depends on the excluded volume interaction and might cancel the impact of the excluded volume interaction. Although we cannot provide a closed form formula for the Edward's correlation length, it is interesting that all points meet at one single point and this point is independent of the capsid charge density, salt concentration

and the polymer excluded volume interaction but depends on the length of genome.

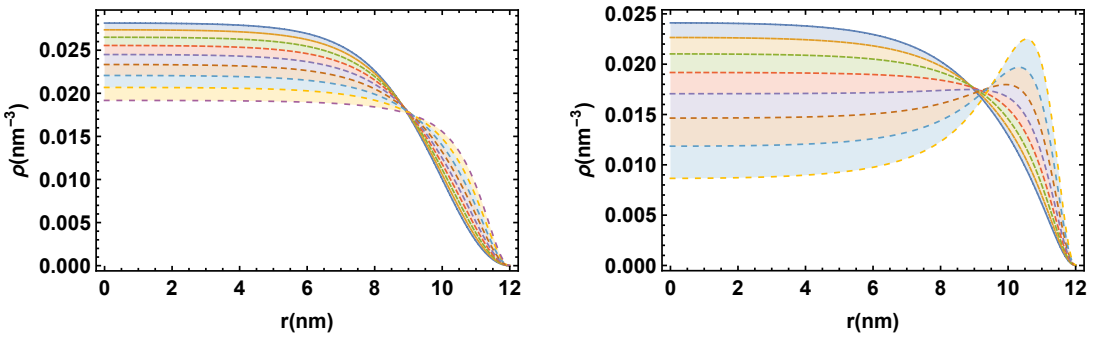

(a) (b)

Figure 2.5: Genome density profile for $N = 100$ and (a) various surface charge density (0-0.4 $e\,\mathrm{nm}^{-2}$) with salt concentration λ=400mM; (b) various salt concentration(250-500 mM) with fixed surface charge $\sigma = 0.4e\,\mathrm{nm}^{-2}$. Other parameters correspond to a=1nm, u_0=0.05nm^3, R=12nm.

.

In summary, in this chapter we investigated the validity of GSDA for studying the profile of genomes in viral shells because of the extensive usage of GSDA in the literature in describing the process of virus assembly and stability. We found that for small RNA segments employed in recent experiments or for *in vitro* assembly studies with mutated capsid proteins carrying lower charge density [30, 57, 70, 71], the GSDA deviates from the accurate results obtained through SCFT methods. Otherwise, native RNA viruses are long enough compared to the radius of the capsid and as such GSDA is good enough to explain different experimental observations and there is no need to solve tedious self-consistent equations. Our results showed that the narrower the region RNA is sitting and the stronger is genome-capsid interaction, the larger the energy gap, and hence the better GSDA works.

Chapter 3

Impact of a non-uniform charge distribution on virus assembly

3.1 Introduction

The simplest viruses consist of two components: the genome, either an RNA or DNA polynucleotide that carries the genetic code, and the capsid, a protein shell that encloses the genome. The capsid consists of many identical (or nearly identical) copies of the coat protein subunit. Even though the coat proteins are highly irregular in shape, the protein shells of most spherical viruses are highly structured and obey icosahedral symmetry [72–75]. One of the consequences of icosahedral symmetry is that it puts restrictions on the number of proteins that can make up a spherical virus shell. It limits this number to 60 times the structural index T that almost always assumes certain "magic" integer values $T = 1, 3, 4, 7, \ldots$ [44, 76, 77].

Many small single-stranded RNA or ssRNA viruses have been shown to spontaneously self-assemble *in vitro*, that is, outside living cells in solutions containing virus coat protein subunits and genome. In fact, virus coat proteins are able to co-assemble with a variety of cargos, including RNAs of other and sometimes unrelated viruses, synthetic polyanions, and negatively charged nanoparticles [21–23]. The spontaneous assembly of properly structured viral capsids of many icosahedral RNA viruses with this variety of cargos, is due to the presence of a disordered RNA binding domain on the N- or C-terminal end of the protein subunits. These are rich in basic amino acids that potentially extend quite deep into the capsid interior. These basic amino acids are positively charged under most solution conditions, and typically bear a few to tens of positive charges depending on the species of virus. It is now widely accepted that electrostatic interactions between the positive charges on the coat protein tails and negative charges on the genome is the main driving force for the spontaneous assembly of simple viruses in solution [24–31, 78].

Naïvely, one might expect that the total charge on the genome and the capsid would balance out, if not perfectly, then certainly approximately. However, in many ssRNA viruses the number of negative charges on the genome significantly exceeds the number of positive charges on capsid proteins. For example, the number of positive charges on capsids of Cowpea Chlorotic Mottle Virus (CCMV) and Brome Mosaic virus (BMV), both with $T = 3$ structures, is about 1800, yet their genome measures about 3000 nucleotides (*nt*) [32]. As each nucleotide bears a single charge, this suggests an *overcharging* of over 60 per cent. Furthermore, in a recent set of *in vitro* experiments, where shorter segments of BMV RNAs in the range of $500 - 2500$ *nt*s were mixed with CCMV capsid proteins, the

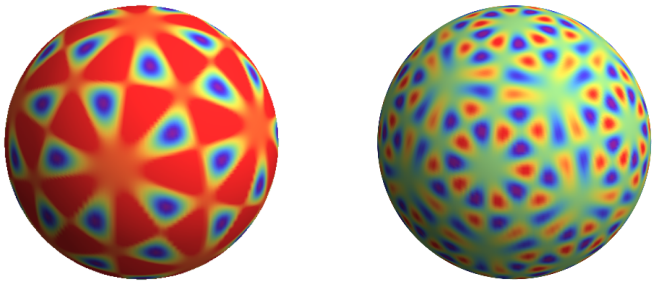

(a) (b)

Figure 3.1: (a) a $T = 1$ structure presented as $ISBF_{15,0}$ (b) a $T = 3$ structure presented as $ISBF_{27,0}$

resulting virus-like particles (VLPs) had a mixed population of pseudo $T = 2$ and $T = 3$ shells that were all overcharged [32]. RNA molecules shorter than 2000 *nt*s were packaged in multiple copies, *e.g.*, four in the case of 500 *nt* RNAs or two for 1000 *nt* RNAs in pseudo $T = 2$ capsids and two 1500 *nt* RNAs in $T = 3$ capsids.

While the *in vitro* self-assembly studies show that RNA-based virus-like particles are overcharged, experiments with linear negatively charged polymers, rather than virus RNAs, are less conclusive. In fact, studies with linear polyanions, such as poly(styrene sulfonate) (PSS), have often focused attention more strongly on how the capsid size distribution is impacted upon by either the polymer length or the stoichiometry ratio of the capsid proteins and polymers [24, 45]. What is known, is that polymers, ranging in degree of polymerisation from $1900 - 16500$ monomers, could all be encapsidated by a $T = 3$ structure, resulting in anything from a weakly to a highly overcharged structure [45]. *In vitro* self-assembly studies on mixtures of CCMV coat proteins and PSS chains as short as 180 monomers show a bimodal distribution of particle sizes corresponding to $T = 1$ and pseudo $T = 2$ structures [79]. According to these experiments there are on average two polymers in

each $T = 1$ capsid (600 positive charges) and three in each T=2 (1200 positive charges) [79]. Hence, the VLPs are in this case undercharged: the ratio of negative to positive charges is 0.6 for the $T = 1$ and 0.45 for $T = 2$ capsids. From all these findings it is not easy to extract a sound conclusion about the optimal length of the encapsulated polymer.

Several theoretical studies have shed light on the puzzling phenomenon of overcharging. Simulations on encapsulation of polymers with a fixed (quenched) level of branching as a model for RNA, have shown that the level of overcharging is a sensitive function of the secondary and tertiary structures of the RNA [16, 37]. Field-theoretic calculations presuming the branching to be annealed, not quenched, have also shown that the length of encapsidated polymer, and hence the level of overcharging, increases as the number of branch points increases [17, 36]. While these theoretical studies confirm that the topology of RNA is important to the phenomenon of overcharging, they also predict that the optimal number of charges on a linear polyelectrolyte must be *less* than the total number of charges on the inner capsid wall: these complexes must be under- rather than overcharged. This contrasts with the molecular dynamics simulations of Perlmutter *et al.*, which show that even linear polyanion encapsulation can lead to overcharging [16].

In virtually all theoretical studies focusing on the assembly of viral shells, the capsid has been assumed to be smooth and to have a uniform charge distribution in a region near the surface of the capsid [52, 53, 73, 80–82]. However, as already alluded to, in most simple RNA viruses the positive charges reside on the RNA binding domains of the coat proteins, which are arranged according to the underlying icosahedral symmetry of the shell. This implies that the charge distribution must somehow reflect this icosahedral symmetry,

certainly near the surface of the capsid, and perhaps less so away from it. Theoretically, the effects of localization of charge near the inner surface of the capsid on the encapsulation of genome remain largely unexplored.

To remedy this, we study the impact of a non-uniform charge density on the optimal length of genome encapsulated by small icosahedral viruses. Since $T = 1$ and $T = 3$ capsids have 60 and 180 RNA binding domains, respectively, we model capsids with 60 and 180 positively charged regions, as shown in Fig. C.1. We show how a non-uniform charge distribution, associated with the underlying icosahedral arrangement of the proteins part of a virus shell, results in a longer optimal genome length compared to a uniform charge distribution. This can give rise to the phenomenon of overcharging even for linear polyanions. The effects of a non-uniform charge distribution and the highly branched secondary structure of RNA, in particular for viral RNAs, conspire to greatly enhance overcharging. This allows for a larger amount of RNA to be packed in the same restricted interior of the virus shell, which arguably would be an evolutionary advantage to the virus.

Furthermore, we find that the optimal length of the genome, and as a result that of the number of encapsulated charges, depends on the detailed structure of RNA binding domains, *i.e.*, the thickness, height and charge density. This is consistent with the experimental findings of Ni *et al.* on Brome Mosaic virus (BMV), in which mutations in the RNA binding domains that keep the number of charges constant but change their length and charge density, impact upon the packaged RNA length [26]. These and many other experiments reveal the existence of intriguing results arising from the N-terminal domain topology [26, 30, 83, 84]. A satisfactory theoretical approach needs to treat the

coat protein topology (N-terminal domains), RNA folding, electrostatic interactions and polymer confinement simultaneously. Our theoretical calculations allow us to single out the impact of length and charge density of the RNA binding domains, without considering other effects such as the impact of translational entropy and kinetic trapping that make the interpretation of experiments and simulations difficult.

3.2 Model

Our model consist of the genome density field that includes the entropic and steric constributions of the polyelectrolyte and the electrostatic interactions between the polyelectrolyte and the capsid. We initially model the genome as a flexible linear polyelectrolyte that interacts attractively with the positive charges residing on the binding domains and postpone the discussion of the impact of RNA secondary structure, to Section II.A.

The free energy of a confined polyelectrolyte confined in a salt solution interacting with an external charge distribution can, within the ground state dominance approximation, be written as

$$\beta F = \int \mathrm{d}^3\mathbf{r} \Big[\frac{1}{6} a^2 |\nabla \Psi(\mathbf{r})|^2 + \frac{1}{2} \upsilon \Psi^4(\mathbf{r}) - \frac{1}{8\pi\lambda_B} |\nabla \beta e \Phi(\mathbf{r})|^2 - 2\mu \cosh\left[\beta e \Phi(\mathbf{r})\right] + \beta\tau \Psi^2(\mathbf{r}) \Phi(\mathbf{r}) + \beta \rho_0(\mathbf{r}) \Phi(\mathbf{r}) \Big], \quad (3.1)$$

with β the reciprocal temperature in units of energy, a the statistical step or Kuhn length of the polymer, υ is effective excluded volume per monomer, $\lambda_B = e^2\beta/4\pi\epsilon$ the Bjerrum length, ϵ the dielectric permittivity, e the elementary charge, μ density of monovalent salt ions, and τ the linear charge density of chain. As usual, the dielectric permittivity of the

medium is persumed constant [85].

The fields $\Psi(\mathbf{r})$ and $\Phi(\mathbf{r})$ are the monomer density field and electrostatic potential of mean force respectively. The positive charge density $\rho_0(\mathbf{r})$ is placed in an icosohedrally symetric distribution either on the capsid surface as shown in Figs. C.1(a) and C.1(b) or extending into the interior of the capsid along the N-terminal tails as in Fig. 3.2(b). Extremizing the free energy with respect to the $\Psi(\mathbf{r})$ and $\Phi(\mathbf{r})$ fields subject to the constraint that the total number of monomers inside the capsid is constant [63], $N = \int \mathrm{d}^3\mathbf{r}\ \Psi^2(\mathbf{r})$, results in two self-consistent non-linear field equations,

$$\frac{a^2}{6}\nabla^2\Psi = -\mathcal{E}\Psi(\mathbf{r}) + \beta\tau\Phi(\mathbf{r})\Psi(\mathbf{r}) + \upsilon\Psi^3 \tag{3.2a}$$

$$\tfrac{\beta e^2}{4\pi\lambda_B}\nabla^2\Phi(\mathbf{r}) = +2\mu e \sinh\beta e\Phi(\mathbf{r}) - \tau\Psi^2(\mathbf{r}) - \rho(\mathbf{r}), \tag{3.2b}$$

with $\mathcal{E}$ the Lagrange multiplier enforcing the fixed number of monomers. Note $\rho(\mathbf{r})$ here is the volume charge density that will be set to zero if there are no charges extended to the interior of capsid. The boundary conditions for the electrostatic potential inside and outside of the capsid that we model as a sphere of radius R are,

$$\hat{n}\cdot\nabla\Phi_{in}\mid_{r=R} - \hat{n}\cdot\nabla\Phi_{out}\mid_{r=R} = 4\pi\lambda_B\sigma(\theta,\phi)/\beta e^2 \tag{3.3a}$$

$$\Phi_{in}(r)\mid_{r=R} = \Phi_{out}(r)\mid_{r=R} \tag{3.3b}$$

$$\Phi_{out}(r)\mid_{r=\infty} = 0. \tag{3.3c}$$

with $\sigma(\theta,\phi)$ the surface charge density. In case of a space charge distribution $\rho \neq 0$, but then we assume $\sigma = 0$. If the charges are localized to the surface, then $\sigma \neq 0$ but the volume charge density $\rho = 0$. Thus, if the charges associated with the capsid are lying completely on the capsid wall, the volume charge density $\rho(\mathbf{r}) = 0$ in Eq. (4.6c), and the

charge from the capsid is modeled as the surface charge $\sigma(\theta, \phi)$ in Eq. (4.7a). We discuss the exact forms of $\sigma(\theta, \phi)$ and $\rho(\mathbf{r})$ in Section II.B.

We use Dirichlet $\Psi(r) \mid_{r=R}= 0$ boundary conditions for the chain density at the capsid wall but our findings are robust and we found the same results for Neumann boundary condition $\partial_r \Psi(r) \mid_{r=R}= 0$. While Eq. (3.2a) applies to a linear chain, a similar formalism can be employed to obtain the free energy of RNA modeled as a branched polymer trapped in a viral shell [17], as explained in the next section.

3.2.1 Branched Polymer

To examine the combined effect of the secondary structure of RNA and non-uniform capsid charge distribution in this chapter, we model RNA as an annealed branched polymer and add to Eq. (4.1) the following terms

$$-\frac{1}{\sqrt{a^3}}(f_e \Psi + \frac{a^3}{6} f_b \Psi^3), \tag{3.4}$$

which describe the statistics of an annealed branched polymer [17, 36, 51, 86–89] with f_e and f_b the fugacities of the end and branch points respectively [17]. The field equations (Eq. (3.2a)) become

$$\frac{a^2}{6}\nabla^2\Psi = -\mathcal{E}\Psi(\mathbf{r}) + \beta\tau\Phi(\mathbf{r})\Psi(\mathbf{r}) + \upsilon\Psi^3 - \frac{f_e}{2\sqrt{a^3}} - \frac{\sqrt{a^3}}{4} f_b \Psi^2, \tag{3.5}$$

In this formalism, the stem-loops or hair-pins in RNA are considered as end points. The number of end and branch points N_e and N_b of the polymer depend on the fugacities $N_e = -\beta f_e \frac{\partial F}{\partial f_e}$ and $N_b = -\beta f_b \frac{\partial F}{\partial f_b}$. We consider only the case of a single encapsulated polymer with no closed loops, and thus we have the following constraint: $N_e = N_b + 2$. The fugacity of branch points f_b determines the degree of branching.

3.2.2 Icosahedral Symmetric Based Function (ISBF)

To explicitly model the charged N-terminal tails, we employ Icosahedral Symmetric Based Functions (ISBFs) for $T = 1$ and $T = 3$ structures with 60 and 180 positively charged regions, respectively. These functions are real-valued, complete, and orthogonal and can be written as a sum over spherical harmonics [90],

$$ISBF_{l,n}(\theta,\phi) = \sum_{m=-l}^{+l} b_{l,n,m} Y_{l,m}(\theta,\phi). \tag{3.6}$$

The ISBF functions are indexed by the integers l and n, where $l(l+1)$ is the azimuthal separation constant. $n \in \{0, 1, ..., N_l - 1\}$ indexes the different ISBFs and N_l denotes the number of linearly independent ISBFs that can be constructed for a given l. The weights $b_{l,n,m}$ can be computed for each l by comparing the expansion of icosahedrally symmetric set of delta functions in both spherical harmonics and ISBFs.

The coefficients, $b_{l,n,m}$ given in Eq. (3.6) become nonzero only when m is a multiple of five, corresponding to five-fold symmetry of icosahedral group. As a function of the associated Legendre function $P_m^l(x)$, ISBFs [90] can easily be written as

$$ISBF_{l,n}(\theta,\phi) = \begin{cases} \sum_{m=0}^{+l} \frac{2}{1+\delta_{m,0}} b_{l,n,m} N_{l,m} P_m^l(\cos\theta)\cos(m\phi), & l : even \\ \sum_{m=1}^{+l} 2 b_{l,n,m} N_{l,m} P_m^l(\cos\theta)\sin(m\phi), & l : odd \end{cases}$$

with $N_{l,m} = \sqrt{\frac{2l+1}{4\pi}\frac{(l-m)!}{(l+m)!}}$.

The charge distributions for structures with $T = 1$ and $T = 3$ icosahedral symmetry are modeled by the ISBF with $(l = 15, n = 0)$ and $(l = 27, n = 0)$ respectively, shown in Figs. C.1(a) and 1(b). The values of $b_{l,n,m}$ for T=1 and T=3 structures are given in Table I.

(a) (b)

Figure 3.2: The charge distributions from the capsids for (a) A T=1 thin capsid. The black spots show the regions with a uniform surface charge density. The charges are smeared on the surface representing the thin capsid model. (b) A T=3 thick capsid. The charges are extended into the interior of the capsid.

Assuming that there are no charges in the regions between N-terminal tails (see Fig. 3.2(a)), we set charge density equal to zero if the magnitude of the ISBFs is smaller than a certain cutoff value C. Thus, the distance between the charged regions depends on the cutoff, and, since we fix the total charge of the capsid, the charge density of the N-terminal domain changes as a function of the cutoff. We consider both the "thin capsid model" where the charges are smeared on the surface of the spherical capsid in 60 or 180 positions as shown in Fig. 3.2(a), and the "thick capsid model" where the charges extend into the capsid as shown in Fig. 3.2(b). For the thick capsid model, we assumed that there are 60 ($T = 1$) or 180 ($T = 3$) "bumpy" charged regions extended inside the capsid. To this end, we shifted and truncated $ISBF_{15,0}$ and $ISBF_{27,0}$ such that the capsid surface protrudes in 60 or 180 positions presenting peptide tails (Fig. 3.2(b)) with charges uniformly distributed in the volume of protruded regions.

3.3 Results

We solved the coupled equations given in Eqs. (4.6) for Ψ and Φ fields, subject to the boundary conditions given in Eqs. (4.7) through the finite element method(FEM). The polymer density profiles Ψ^2 as a function of the distance from the center of the shell, r, are shown in Figs. 4.2(a) and 4.2(b) in three and one dimension(s) respectively. As illustrated in the figure, the polymer density is higher at the N-terminal regions. Note that the density at the wall in the regions between N-terminal tails is lower than that in the N-terminal domains, but still higher compared to the capsid center even though the capsid wall is not charged between the tails.

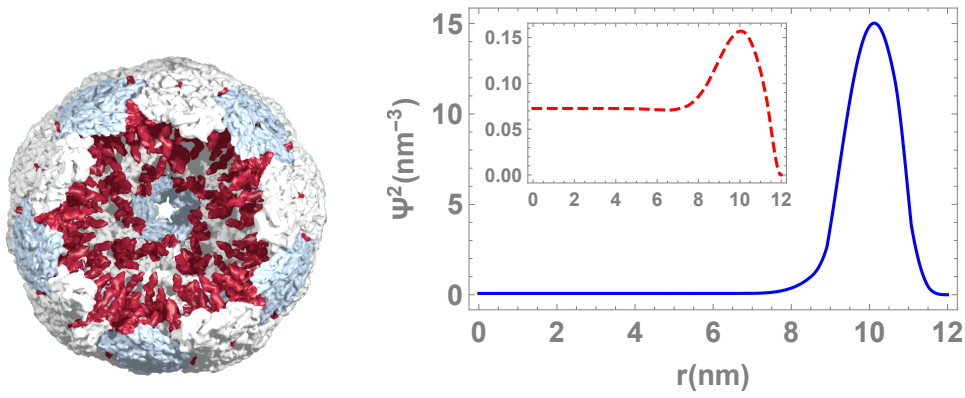

(a) (b)

Figure 3.3: Genome density profile of a T=3 capsid in (a) 3D view. The protruded regions represent RNA (red). The density of RNA between N-terminals is very small and not shown in the figure. (b) 1D view as the function of capsid radius with non-uniform charge distribution. The figure shows the profiles along two different directions. The solid line corresponds to the direction in which the N-terminal tail is located and the dashed line to the direction without N-terminal tail (inset graph). In the absence of surface charge density and N-terminal tail (dashed curve), the density is still maximum close to the wall. The polymer is branched with $f_b = 3$, total monomer number=2411, salt concentration $\mu = 100$mM, $R = 12$nm and $Qc = 1800$.

We find that the optimal genome length increases for a non-uniform charge distribution as compared to that where the charge distribution is uniform. In fact, the free

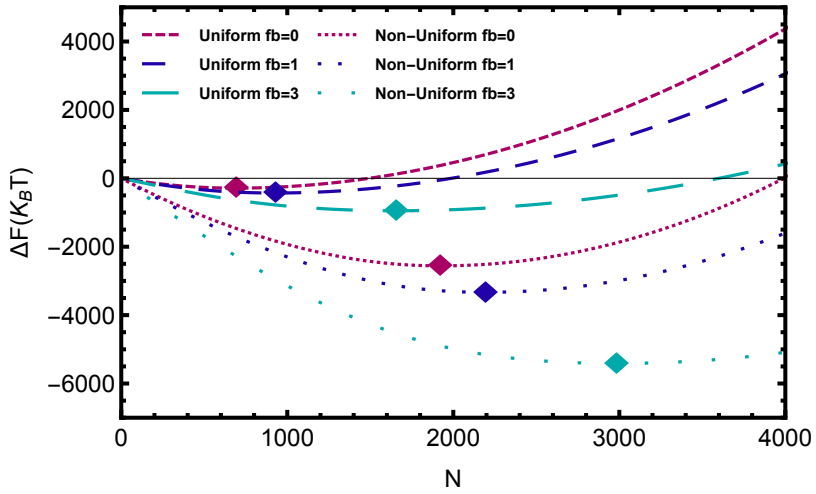

Figure 3.4: Encapsulation free energy for a linear and branched polyelectrolyte as a function of monomer number for a capsid with uniform (dashed lines) and non-uniform (dotted lines) charge density. For a linear chain the branching fugacity $f_b = 0$ and increases to $f_b = 1.0$ and $f_b = 3.0$ as the chain becomes more branched. The diamonds indicate the minimum of free energy. Other parameters used correspond to a $T = 3$ virus: total capsid charges on capsid $Q_c = 1800$, $a = 1.0\ nm$, $v = 0.01\ nm^3$, $\mu = 100\ mM$, $R = 12\ nm$, tail length $= 4\ nm$

energy in addition becomes deeper indicating a higher efficiency of genome encapsulation. Furthermore, we find that the optimal genome length increases if the cutoff C is increased, and that the distance between the charged regions correspondingly increases. That is, as the charges on the capsid are distributed *more* non-uniformly, the optimal genome length increases. Nevertheless, for the thin capsid model, we have not been able to observe the phenomenon of overcharging with linear chains, *i.e.*, the number of charges on genome is always lower than those on the capsids for all the parameters values that we tested. This is not the case for the thick capsid model as explained below.

Figure 3.4 illustrates the encapsulation free energy as a function of genome length for a $T = 3$ structure with the radius of capsid $R = 12\ nm$ at $\mu = 100\ mM$ salt concentrations for the thick capsid model (Fig. 3.2(b)). The total number of charges are assumed to be $Q_c = 1800$ for a $T = 3$ structure, 10 charges on each N-terminal tail. The dashed lines

in Fig. 3.4 correspond to a capsid with a uniform charge density and the dotted lines to a non-uniform charge density. The lines with the smallest distance between the dashed and dots correspond to that of a linear polymer. As illustrated in the figure, the minimum of the free energy moves towards longer chains if the charge distribution is non-uniform.

Figure 3.4 also shows the impact of RNA secondary structures on the optimal length of encapsulated genome. The graphs in Fig. 3.4 corresponds to $f_b = 0$ for a linear polymer and $f_b = 1.0$ and $f_b = 3.0$ for branched ones. The polymer becomes more strongly branched as f_b increases. Note that in the figure the distance between dots or dashed lines increases as the fugacity or the number of branch points increases. The figure reveals that as the degree of branching increases, the length of encapsulated genome increases for a capsid with a uniform charge density. This effect becomes stronger if we consider a non-uniform charge distribution. The diamonds in the figure indicate the optimal length of genome. The ratios of the optimal length or number of charges on RNA to the capsid total charge $Q_c = 1800$ from left to right in the figure are 0.39, 0.52, 0.92, 1.07, 1.22, 1.66, which clearly shows a transition from undercharging towards overcharging. We note that we find the same behavior when employing a $T = 1$ instead of a $T = 3$ capsid.

3.4 Discussion and Summary

The reason for overcharging associated with the non-uniform charge distributions is twofold. A non-uniform charge distribution on the capsids obviously promotes a non-uniform genome density distribution. However, in order to have a more uniform polymer distribution with lower entropy cost, longer chains are preferably encapsulated to make

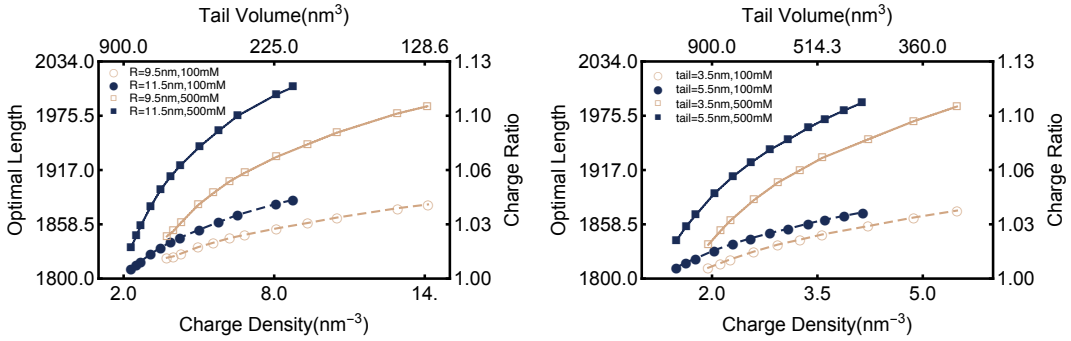

(a) (b)

Figure 3.5: Optimal genome length or Charge Ratio vs. N-terminal charge density or volume occupied for a $T = 3$. (a) Hollow symbols correspond to capsid radius of $R = 9.5\ nm$ and solid ones to $R = 11.5\ nm$ with the N-terminal tail length 3.5 nm; (b) Hollow symbols correspond to tail length of 3.5 nm and solid ones to 5.5 nm for $R = 12.5\ nm$. Other parameters are total charge $Qc = 1800$, and salt concentration $\mu = 100\ mM$ (dashed) and $\mu = 500\ mM$ (solid)

the genome distribution more uniform in the regions between the N-terminal tails. Figure 3.5(a) illustrates this effect for a $T = 3$ structure with 180 tails as a plot of the optimal length of genome *vs.* the capsid charge density. Note that since the total charge of capsid is fixed, as we increase the charge density, we lower the volume of the N-terminal regions, which is also shown in the axis on the top of the graph. The vertical axis on the right-hand side of the figure shows the degree of overcharging. The circles in the figure correspond to $\mu = 100\ mM$ salt concentration and squares to $\mu = 500\ mM$. For the hollow symbols the radius of capsid is $R = 9.5\ nm$ but for the solid symbols $R = 11.5\ nm$. As shown in the figure, if we increase the area between the N-terminals or the radius of capsid, the amount of overcharging increases at a given salt concentration.

However, the noted entropy effect cannot explain all the observations. At the physiological salt concentration of $\mu = 100\ mM$, the genome only interacts with the capsid if it is sitting in vicinity of the capsid coat protein charges. This is due to the rather short range

of electrostatic interactions at that salt concentration. The presence of N-terminals increases the region with which the genome interacts attractively through electrostatic interactions. Thus, the higher the salt concentration, the more important becomes the role of N-terminals. The figure shows that the overcharging is more pronounced at $\mu = 500\, mM$. Also, the higher salt concentration, the lower is the electrostatic self-repulsion between genome monomers, which helps to the encapsidation of longer chains.

We also examined the impact of the length of N-terminal domains in the thick capsid model, which corresponds to how far the charged regions extend into the interior of the capsid. As illustrated in Fig. 3.5(b) for $T = 3$ capsids, more genome is encapsidated for longer N-terminal tails, which is again due to larger interacting region for a fixed total numer of charges on the capsid. The effect becomes more pronounced for higher salt concentrations as illustrated in the figure.

In summary, we have studied the phenomena of overcharging observed in many viruses. Previous mean-field theories as well as the experimental studies of CCMV capsid proteins with short linear polymers have indicated the resulting VLPs are undercharged [17, 18, 18, 36, 54, 91, 92]. However, MD simulations revealed overcharging can happen even for linear polymers and the question is why [16]. In this chapter, we showed that the non-uniform charge distribution increases both the stability and the amount of genome that can be assembled by CPs as a result of what in essence is entropy. For a thin capsid model with the charges smeared flatly on the surface, longer chains are encapsulated, but we have not been able to observe overcharging with linear polymers. This indicates that overcharging for linear systems is primarily due to the charged N-terminal regions that protrude into the

interior of the capsid. The N-terminal regions increase the regions in which the genome can interact with the capsid proteins and thus resulting in the encapsidation of longer chains. This latter effect is stronger at higher salt concentrations. We find that the combined effect of RNA base-pairing, which gives rise to the genome branching, and non-uniform charge distribution can explain the pronounced charge inversion observed in viruses.

Chapter 4

The effect of RNA stiffness on the self-assembly of virus particles

4.1 Introduction

Ribonucleic acid (RNA) is one of the molecules of life, which plays a central role in the cell as information carriers, enzymes, gene regulators, et cetera. It is made out of four elementary building nucleotides, being A(denine), G(uanine), C(ytosine) and U(racil) [93]. As shown by Crick and Watson, purines (A,G) pair with complementary pyrimidines (C,U), leading primarily to the pairs CG and AU. There exist also so-called wobble pairs of GU. Single stranded RNA is quite flexible with a Kuhn length of, depending on the ionic strength of the solution, one or two nm [94], and can form double helical stems (A helices) with a Kuhn length of about 140 nm [62, 95]. So, double stranded RNA is stiffer than double stranded DNA, which has a Kuhn length of 100 nm, noting that the Kuhn length is twice

the persistence length of a so-valled wormlike chain.

The pairing of bases over long distances along the backbone gives rise to the secondary or folded structure of RNA. Pairing of bases can be represented by so-called arch diagrams. Nested arches represent helices, while crossings give rise to the so-called pseudoknots [96]. The nested pairings can be described quantitatively by recursion relations [6,97,98], which exactly sum all possible pairings without pseudoknots. From a geometrical point of view, the generated structures can be viewed as branched polymers. The size of an ideal, Gaussian linear polymer scales as the number of "segments" to the power $\nu = 1/2$, while ideal branched ones have a scaling exponent $\nu = 1/4$ [99]. Note that there is no excluded volume interaction between monomers of an ideal chain. For self-avoiding chains the scaling exponents are $\nu = 3/5$ and $\nu = 1/2$ for the linear and branched polymers, respectively [99,100]. However, because of its *tertiary* structures that include pseudoknots, RNAs are significantly more compact than branched polymers. Indeed, several numerical studies and surveys have found the exponent $\nu = 1/3$ to be small for RNA, reflecting this more compact structure [37,101].

Several recent self-assembly experimental studies reveal the importance of non-electrostatic interactions, associated with specific structures of the genome, for the selection of one RNA over another by the capsid proteins [102]. The self-assembly studies of Comas-Garcia *et al.* [32] reveal in particular the importance of RNA topology. They carried out a number of experiments in which a solution of the capsid proteins of cowpea chlorotic mottle virus(CCMV) were mixed with equal amount of RNA1 of Brome Mosaic virus (BMV) and RNA1 of Cowpea Chlorotic Mottle Virus (CCMV). In this head-to-head competition, the

amount of coat protein (CP) of CCMV was selected such that it could only encapsidate one of the genomes. Quite unexpectedly, the RNA1 of CCMV (the cognate RNA) lost to RNA1 of BMV, *i.e*, only RNA1 of BMV was encapsidated by CCMV CPs. These experiments emphasize the impact of RNA structure on the assembly of viral shells, as RNA1 of BMV has a more compact structure than that of CCMV [17].

Following these experiments a number of simulation studies, using quenched (fixed) branched polymers as a model for RNA, have shown that the optimal length of encapsidated RNA increases when accounting for its secondary structure [16,37]. Mean-field calculations using annealed (equilibrium) branched polymers as model RNAs have also shown that the length of encapsidated polymer increases as the propensity to form larger numbers of branched points increases [17, 36, 103]. More importantly, these calculations show that a higher level of branching considerably increases the depth of the free-energy gain associated with the encapsulation of RNA by a positively charged shell. This implies that the efficiency of genome packaging goes up with increasing the level of branching, so with increasing compact secondary structure of the genome.

In fact, it was shown in Refs. [49, 104] that while RNA molecules of the same nucleotide length and composition might have similar amounts of base pairing, non-viral RNAs have significantly less compact structures than viral ones. The compactness of viral RNAs has been associated with the presence of a larger fraction of higher-order junctions or branch points in their secondary structure [101,104,105]. Figure 4.1(a) and (b) illustrate the secondary structures of CCMV RNA and those of a randomly sequenced RNA with the same length. The structures are obtained through the Vienna RNA software package [6].

(a) (b)

Figure 4.1: (a) The secondary structure of the CCMV RNA1 and (b) a random RNA with the same number of nucleotides. The structures are obtained using the the Vienna RNA package [6].

As shown in the figure, CCMV RNA has considerably larger number of branched points than non-viral RNA of the same length.

Above-mentioned theoretical and experimental studies indicate that in a head-to-head competition between two different types of RNAs, the RNA with a larger number of branching junctions or branch points should have a competitive edge over others [17,36,103]. A naive physical explanation is that branching causes RNA molecules to become more compact than structureless linear polymers of similar chain length, which are then easier to accommodate in the limited space provided by the cavity of a capsid. According to these theories and simulations, a linear chain should definitely "loose" to a branched one of the same number of monomers when competing head-to-head for a limited number of capsid proteins.

To probe the effect of RNA structure and test the above theories on the self-

assembly of virions more systematically, Beren *et al.* [106] recently performed a set of *in vitro* packaging experiments with polyU, an RNA molecule that has no folded secondary structure. They examined whether RNA topology, i.e., the secondary structure or level of branching, allows the viral RNA to be exclusively packaged by its cognate capsid proteins. More specifically, they studied the competition between CCMV viral RNA with polyU of equal number of nucleotides for virus capsid proteins. They find that CCMV CPs are capable of packaging polyU RNAs and, quite interestingly, polyU outcompetes the native CCMV RNA in a head-to-head competition for the capsid proteins. These findings are in sharp contrast with the previous experimental, theoretical, simulation and scaling studies noted above, which suggest that the branching and compactness of RNA must lead to a more efficient capsid assembly. That being said, the scaling theory of Ref. [81] already hints at the subtle interplay between Kuhn length, solvent quality and linear charge density dictating the free energy gain of encapsulation.

To explain these intriguing experimental findings, we employ a field density functional theory and study the impact of RNA branching, while allowing for differences in Kuhn length. We further consider that double helical sequences have a larger linear charge density than non-hybridized sequences along the chain. In all previous theoretical and simulation studies related to the impact of RNA topology on virus assembly, the focus has been on the importance of the degree of branching, ignoring the impact of base-pairing on the RNA Kuhn length and linear charge density.

As noted above, the Kuhn length of single stranded RNA under physiological conditions of monovalent salt is between one and two nm depending on the ionic strength

[94], while that of a double stranded RNA is about 140 nm [62, 95]. The average duplex length of viral RNA is about six nucleotide pairs [101], which corresponds to about five nm. This value is much smaller than the persistence length of double stranded RNA [104], suggesting that viral RNA can be modeled as a flexible polymer with an average Kuhn length of about six paired nucleotides. There are of course also loop sequences that in our model act as end, hinge and branching points, but how this translates into an effective Kuhn length for the entire branched chain representation of the RNA is unclear. Plausibly, the effective Kuhn length of the internally hybridized chain should be larger than that of the equivalent unstructured non-hybridized chain. Furthermore, another major difference between the linear and branched (base-paired) ssRNA structures seems to be the linear charge density, which doubles for the latter on account of base pairing (hybredization).

In this chapter, we vary the degree of branching as well as the effective Kuhn length and linear charge density of a model RNA, and study their impact on the optimal length of encapsulated genome by capsid proteins. We find that as we increase the chain stiffness or Kuhn length the free energy of encapsulation of RNA becomes less negative than that of a linear chain, at least under certain conditions. Hence, a larger Kuhn length, associated with base-pairing, might decrease the efficiency of packaging of RNA compared to a linear polymer. In contrast, our results indicate that increasing the linear charge density improves the efficiency of packaging of both linear and branched polymers. Thus base-pairing has two competing effects: it makes the chain stiffer, which increases the work required to encapsidate the chain, but at the same time it increases the linear charge density that lowers the encapsidation free energy and augment the packaging efficiency. These results

are consistent with the experiments of Beren *et al.* [106], in which the linear RNA, PolyU, outcompetes the cognate RNA of CCMV when they are both in solution with a limited amount of capsid proteins of CCMV, that is, sufficient to encapsidate either PolyU or CCMV RNA but not both.

4.2 Model

The free energy associated with a genome trapped inside a spherical capsid has been studied in the previous chapters. In this chapter we focus on the case of annealed branched polymers as the degree of branching of RNAs [107], and write the free energy as [17, 30, 36, 51, 59, 82, 103, 108]

$$\begin{aligned}\beta F =& \int \mathrm{d}^3\mathbf{r}\Big[\tfrac{\ell^2}{6}|\nabla\Psi(\mathbf{r})|^2 + \frac{1}{2}\upsilon\Psi^4(\mathbf{r}) + W\big[\Psi(\mathbf{r})\big] \\ & - \tfrac{1}{8\pi\lambda_B}|\nabla\beta e\Phi(\mathbf{r})|^2 - 2\mu\cosh\big[\beta e\Phi(\mathbf{r})\big] + \beta\tau\Phi(\mathbf{r})\Psi^2(\mathbf{r})\Big] + \int \mathrm{d}^2 r\Big[\beta\sigma\,\Phi(\mathbf{r})\Big]. \quad (4.1)\end{aligned}$$

with β the inverse of temperature in units of energy, υ the effective excluded volume per monomer, $\lambda_B = e^2\beta/4\pi\epsilon$ the Bjerrum length, e the elementary charge, μ the number density of monovalent salt ions, and τ the charge of the statistical Kuhn segment of the chain. The dielectric permittivity of the medium ϵ is assumed to be constant [85]. The quantity ℓ, the Kuhn length of the polymer, is defined as an effective stiffness averaged over the entire sequence along the genome. Further, the fields $\Psi(r)$ and $\Phi(r)$ describe the square root of the monomer density field and the electrostatic potential, respectively, and the term $W[\Psi]$ corresponds to the free energy density of an annealed branched polymer as described in Eq. 4.2 below.

As discussed in the Introduction, the secondary structure of the RNA molecules contain considerable numbers of junctions of single-stranded loops from which three or more duplexes exit. This makes RNA act effectively as a flexible branched polymer in solution. While the Kuhn length for a single stranded, non self-hybridized ssRNA is a few nanometers and that for a double stranded RNA is about 140 nanometers, the Kuhn length of viral RNA is not well determined, as we discussed above. In the absence of exact measurements, we employ an average or effective value for ℓ, which presumably will be larger if the number of consecutive base pairs (duplexes) between single stranded segments or stem loops along the RNA is larger. Further, we consider the limit of long chains consisting of a very large number of segments $N \to \infty$ for our confined chains, where N denotes the number of segments. In this formal limit, we employ the ground-state dominance approximation implicit in Eq. (1), as it has proven to be accurate provided $N \gg 1$, i.e., for very long chains [56]. We specify below the connection between the number of segments and the number of nucleotides that make up the RNA, differentiating between self-hybridized and non self-hybridized RNAs.

The first term in Eq. (4.1) is the entropic cost of deviation from a uniform chain density and the second term describes the influence of excluded volume interactions. The last two lines of Eq. (4.1) are associated with the electrostatic interactions between the chain segments, the capsid and the salt ions at the level of Poisson-Boltzmann theory [18,59,109]. The term $W[\Psi]$ represents the free energy density associated with the annealed branching of the polymer [86–89],

$$W[\Psi] = -\frac{1}{\sqrt{\ell^3}}(f_e\Psi + \frac{\ell^3}{6}f_b\Psi^3), \tag{4.2}$$

where f_e and f_b are the fugacities of the end and branched points of the annealed polymer,

respectively [51]. Note that the stem-loop or hair-pin configurations of RNA are counted as end points. The quantity $\frac{1}{\sqrt{\ell^3}} f_e \Psi$ indicates the density of end points and $\frac{\sqrt{\ell^3}}{6} f_b \Psi^3$ the density of branch points. The number of end N_e and branched points N_b are related to the fugacities f_e and f_b, respectively, and can be written as

$$N_e = -\beta f_e \frac{\partial F}{\partial f_e} \qquad \text{and} \qquad N_b = -\beta f_b \frac{\partial F}{\partial f_b}. \tag{4.3}$$

There are two additional constraints in the problem. Note first that the total number of monomers (Kuhn lengths) inside the capsid is fixed [63, 110],

$$N = \int \mathrm{d}^3\mathbf{r}\ \Psi^2(\mathbf{r}). \tag{4.4}$$

We impose this constraint through a Lagrange multiplier, $\mathcal{E}$, introduced below. Second, there is a relation between the number of the end and branched points,

$$N_e = N_b + 2, \tag{4.5}$$

as there is only a single polymer in the cavity that by construction has no closed loops as it has to mimic the secondary structure of an RNA. The polymer is linear if $f_b = 0$, and the number of branched points increases with increasing value of f_b. For our calculations, we vary f_b and find f_e through Eqs. (4.3) and (4.5). Thus, f_e is not a free parameter.

Varying the free energy functional with respect to the monomer density field $\Psi(r)$ and the electrostatic potential $\Phi(r)$, subject to the constraint that the total number of monomers inside the capsid is constant [63], we obtain two self-consistent non-linear differential equations, which couple the monomer density with the electrostatic potential in the

interior of the capsid. The resulting equations are

$$\frac{\ell^2}{6}\nabla^2\Psi = -\mathcal{E}\Psi(\mathbf{r}) + \beta\tau\Phi(\mathbf{r})\Psi(\mathbf{r}) + \upsilon\Psi^3 + \frac{1}{2}\frac{\partial W}{\partial\Psi} \tag{4.6a}$$

$$\frac{\beta e^2}{4\pi\lambda_B}\nabla^2\Phi_{in}(\mathbf{r}) = 2\mu e \sinh\beta e\Phi_{in}(\mathbf{r}) - \tau\Psi^2(\mathbf{r}) \tag{4.6b}$$

$$\frac{\beta e^2}{4\pi\lambda_B}\nabla^2\Phi_{out}(\mathbf{r}) = 2\mu e \sinh\beta e\Phi_{out}(\mathbf{r}) \tag{4.6c}$$

with $\mathcal{E}$ the earlier mentioned Lagrange multiplier enforcing the fixed number of monomers in the cavity. The boundary conditions for the electrostatic potential inside and outside of the spherical shell of radius R are,

$$\hat{n}\cdot\nabla\Phi_{in} \mid_{r=R} - \hat{n}\cdot\nabla\Phi_{out} \mid_{r=R} = 4\pi\lambda_B\sigma/\beta e^2 \tag{4.7a}$$

$$\Phi_{in}(\mathbf{r}) \mid_{r=R} = \Phi_{out}(\mathbf{r}) \mid_{r=R} \tag{4.7b}$$

$$\Phi_{out}(\mathbf{r}) \mid_{\mathbf{r}=\infty} = 0. \tag{4.7c}$$

The boundary condition (BC) for the electrostatic potential is obtained by minimizing the free energy assuming the surface charge density σ is fixed. The concentration of the polymer outside of the capsid is assumed to be zero. The BC for the inside monomer density field Ψ is of Neumann type ($\hat{n}\cdot\nabla\Psi|_s = 0$) that can be obtained from the energy minimization [63] but our findings are robust and our conclusion do not change if we impose the Dirichlet boundary condition $\Psi(r) \mid_{r=R}= 0$. The former represent a neutral surface, whilst the latter a repelling surface. [56]

4.3 Results

We solved the coupled equations given in Eqs. (4.6) for the Ψ and Φ fields, subject to the boundary conditions in Eqs. (4.7) through a finite element method (FEM). The

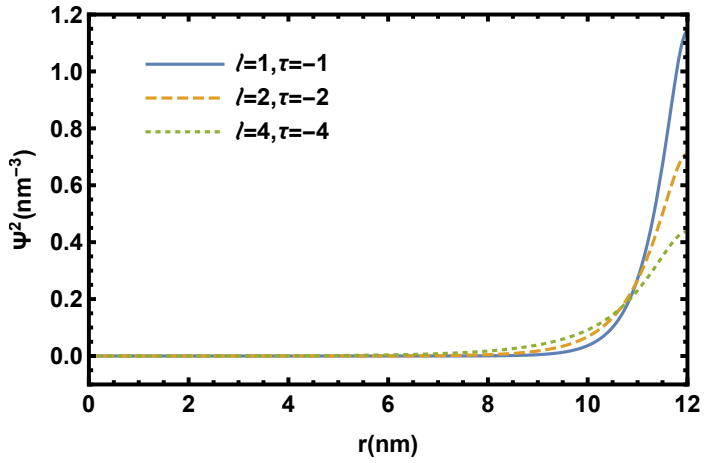

Figure 4.2: Genome density profile as a function of distance from the capsid center for a linear polymer with $l = 1nm$ (solid line), $l = 2nm$(dashed line) and $l = 4nm$(dotted line). Other parameters used correspond to a $T = 3$ virus: the total capsid charges on capsid $Q_c = 1800e$, the strength of excluded volume interaction $\upsilon = 0.05nm^3$, the fugacity $f_b = 0$, the quantity μ corresponds to a salt concentration of $100mM$, the capsid radius $R = 12nm$, the temperature $T = 300K$ and total number of nucleotides for all three cases equals 1000.

polymer density profiles Ψ^2 as a function of the distance from the center of the shell, r, are shown in Fig. 4.2 for different values of the RNA stiffness ℓ and a fixed number of nucleotides, presuming the RNA not to have any secondary structure. Note that for simplicity we assume that a linear chain with $\ell = 1\ nm$ contains one nucleotide and carries one negative charge, so $\tau = -e$, $\ell = 2\ nm$ has two nucleotides with two negative charges and so on. Thus in our figures the numerical value of ℓ also indicates the number of nucleotides in one Kuhn length for linear chains. For the three plots in Fig. 4.2, the total number of nucleotides is calculated using Eq. 4.4 and is equal to 1000. It is worth mentioning that Eq. 4.4 gives us the total number of Kuhn lengths N and we multiply it by ℓ the number of nucleotides along one Kuhn length to obtain the total number of nucleotides.

As illustrated in the figure, the polymer density becomes larger at the wall as the Kuhn length decreases, even though the linear charge density is fixed. In all plots for

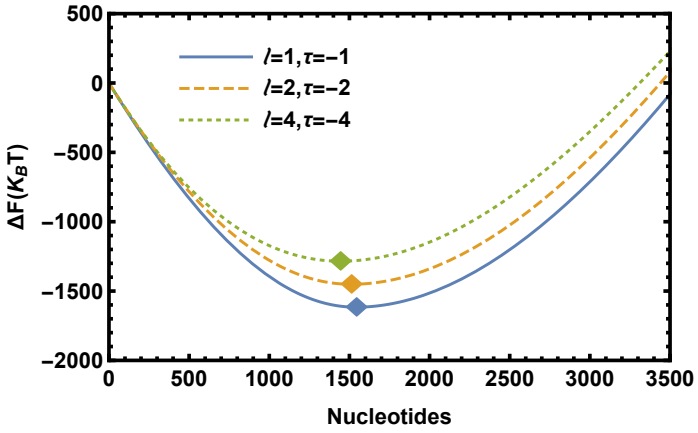

Figure 4.3: Encapsidation free energy of a linear polymer as a function of number of nucleotides for $\ell = 1nm$ (solid line), $\ell = 2nm$ (dashed line) and $\ell = 4nm$ (dotted line). As the stiffness ℓ increases, the optimal number of nucleotides moves towards shorter chains. The quantity τ indicates the number of negative charges in one Kuhn segment. Other parameters used are the total number of charges on the capsid $Q_c = 1800$, the excluded volume parameter $\upsilon = 0.05nm^3$, the quantity μ corresponds to a salt concentration of $100mM$, the radius of the cavity of the capsid $R = 12nm$ and the absolute temperature $T = 300K$.

Fig. 4.2 we assumed that the excluded volume is kept constant. Arguably, the excluded volume parameter υ depends on ℓ, and usually it is assumed that $\upsilon \propto \ell^3$ [56]. As we will discuss in Sect. 4.4, our conclusions about the role of stiffness in the encapsidation free energy are robust and should not sensitively depend on the strength of the excluded volume interaction.

To investigate the packaging efficiency of a linear chain as a function of its stiffness, we obtained the free energy of the encapsidation of the linear polymer model as a function of number of nucleotides for different values of ℓ, as illustrated in Fig. 4.3. The figure shows that the optimal number of nucleotides trapped in the shell increases as ℓ decreases. We emphasize again that since we assumed that the size of a single nucleotide is about one nm, the numerical value of ℓ represents the number of nucleotides within one Kuhn length. This implies that the number of nucleotides and hence the number of charges per Kuhn

segment should increase as the Kuhn length increases. For example, in our parametrization $\ell = 4nm$ represents four nucleotides (resulting in $\tau = -4e$). We observe the same behavior for the free energy of branched polymers, that is, increasing ℓ causes the optimal length of genome to move towards shorter chains. Obviously the stiffness value ℓ is larger for the RNAs whose average number of base pairs in the duplex segments is larger.

The concept of the number of nucleotides per Kuhn length is trickier to implement for the branched polymers taken as model for self-hybridized ssRNA. For example, a branched polymer with the Kuhn length $\ell = 1nm$ represents in our model description two nucleotides and a charge of $\tau = -2e$. When the average number of base pairs is about 8 in duplex segments of an ssRNA, we consider the Kuhn length is about eight nm, but the number of nucleotides and number of charges per Kuhn length τ will be 16. Thus, in our prescription of the self-hybridized ssRNA the number of nucleotides is twice the value of ℓ within a Kuhn length as a result of base pairing.

We also examined the impact of the fugacity on the optimal number of nucleotides. There is a direct relation between the fugacity and the number of branched points: As the fugacity increases the number of branched points of RNA increases too, see [17, 36, 103]. Figure 4.4 illustrates that the optimal number of nucleotides increases and the encapsidation free energy becomes more negative, indicating a more stable complex, as the fugacity of branching and hence the number of branch points increases. The solid line in the figure shows the free energy of a linear polymer. For the case shown in the figure, the Kuhn length of the linear chain is $\ell = 1nm$ but that for the branched polymers $\ell = 4nm$, corresponding to four base-paired nucleotides. The number of charges within one Kuhn length then is

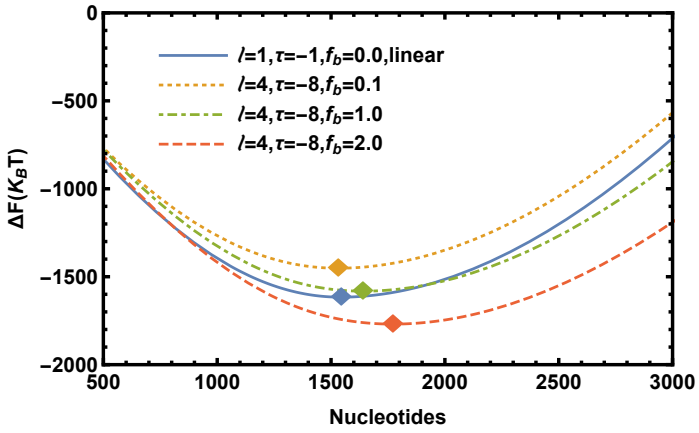

Figure 4.4: Encapsidation free energy as a function of number of nucleotides for a linear (solid line) and branched chains with different degree of branching: $f_b = 0.1$ (dotted line), $f_b = 1$ (dot-dashed line) and $f_b = 2$ (dashed line). As the fugacity f_b (and hence the number of branched points) increases, the optimal number of nucleotides moves towards longer chains. Other parameters are $Q_c = 1800e$, $\upsilon = 0.05nm^3$, the quantity μ corresponds to a salt concentration of $100mM$, $R = 12nm$ and $T = 300K$.

$\tau = -8e$.

Figure 4.4 reveals that the free energy of the linear chain is lower than that of the branched one in certain regions of parameter space. For example, for a branched polymer with fugacity $f_b = 0.1$, $\ell = 4nm$ and $\tau = -8e$ (dotted line), the encapsidation free energy of a linear chain with $\ell = 1nm$ and $\tau = -e$ is always lower than that of the branched polymer, and thus, in a head-to-head competition with a limited number of proteins, the linear chain will be the one that is preferentially encapsidated by capsid proteins. This shows that the work of compaction of linear chains could be lower than that of a branched polymer, depending on the stiffness and the degree of branching of the polymers involved. Note that for a fixed ℓ while the number of branch points (f_b) increases, at some point, the branched polymers outcompetes the linear polymer for binding to capsid proteins, as is illustrated in the figure.

We next studied the free energy of a branched polymer with a fixed fugacity for

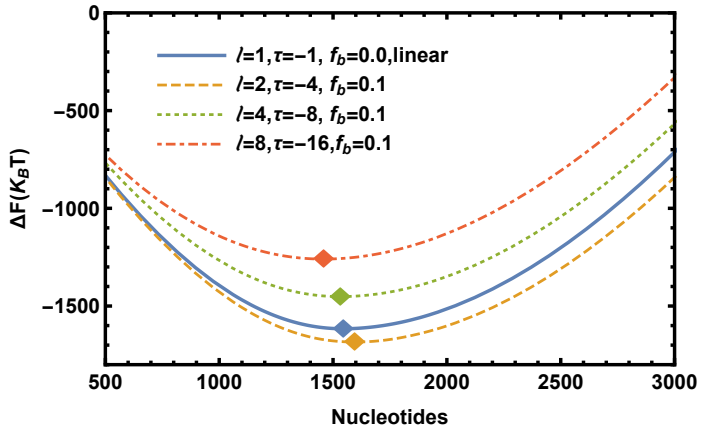

Figure 4.5: Encapsidation free energy as a function of number of nucleotides for a linear (solid line) and a branched chain at $\ell = 2nm$ (dashed line), $\ell = 4nm$ (dotted line) and $\ell = 8nm$ (dot-dashed line). Other parameters used are $Q_c = 1800e$, $\upsilon = 0.05nm^3$, the quantity μ corresponds to a salt concentration of $100mM$, $R = 12nm$ and $T = 300K$.

different values of the stiffness ℓ. As illustrated in Fig. 4.5 for a fugacity $f_b = 0.1$, the linear chain (solid) "looses" to a branched one when four nucleotides have formed two base pairs with $\ell = 2nm$ and $\tau = -4e$ (dashed line). However, the figure shows that as ℓ increases, for $\ell = 4nm$ and $8nm$ (dotted and dotted-dashed lines), their encapsidation free energies become larger than that of the linear chain, indicating that in a head-to-head competition the linear polymer will be encapsidated. Thus, if the average number of nucleotides in duplex segments increases, it becomes energetically more costly to confine RNA inside the capsid.

4.4 Discussion

Recent experiments emphasized on the crucial role of the RNA topology in the efficiency of virus assembly. As noted in the introduction, Comas-Garcia *et al.* [32] have shown that CCMV capsid proteins exclusively encapsidate BMV RNA in the presence of the

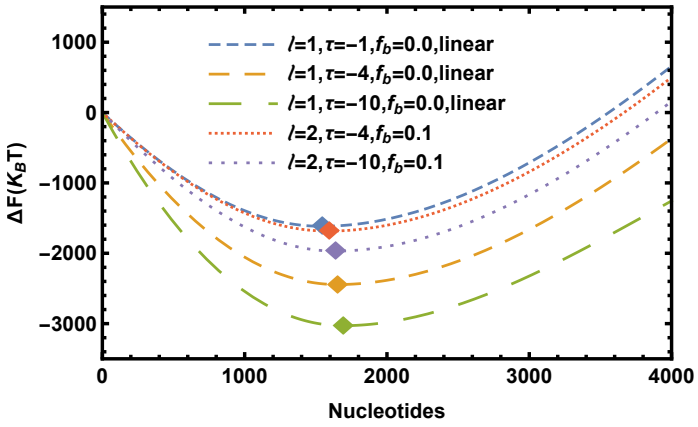

Figure 4.6: Encapsidation free energy as a function of the number of nucleotides for linear (dashed lines) and branched chains(dotted lines), with various number of charges within one Kuhn length τ. Other parameters are $Q_c = 1800e$, $\upsilon = 0.05nm^3$, the quantity μ corresponds to a salt concentration of $100mM$, $R = 12nm$ and $T = 300K$.

cognate CCMV RNA under conditions where there is a limited number of capsid proteins in solution. The simulations and analytical studies performed in Refs. [16, 17, 36, 55, 103] are consistent with these results: the viral RNA with a larger degree of branching has a competitive edge over the other viral RNAs or non-viral randomly branched RNAs, keeping all other chain quantities equal.

Indeed, all field theories, numerical calculations and simulations up to now have indicated that the encapsidation free energy of both annealed and quenched branched polymers is significantly lower than that of linear polymers. This suggests that if there are equal amounts of linear and branched polymers in a solution, but there are sufficient capsid proteins to encapsulate exclusively half of the genomes in solutions, only the branched polymer is encapsidated by capsid proteins. Nevertheless, according to a series of more recent experiments by Beren *et al.* [106] in a head-to head competition between a linear (polyU) chain and CCMV RNA of equal length, surprisingly, and in contrast to theoretical predictions, the linear chain outcompetes the cognate RNA.

While previous theoretical studies have focused on the scaling behavior of linear and branched flexible polymers [17, 18, 36, 53–55, 103], in this chapter we study the impact of the stiffness or Kuhn length on the encapsidation of RNA by capsid proteins. In general the duplexed segments of viral RNA contain on average about five to six base-pairs [101]. Note that some studies show that viral RNAs must have between 60 and 70 per cent of their nucleotides in duplexes, so the linear charge density is almost a factor of two larger and the effective chain length about twice shorter [111]. We argue that while the base pairing on the one hand makes the RNA more compact, on the other hand it increases the effective Kuhn length or the statistical length of the polymer unit. This leads to an increase in the work of compaction of the flexible chain by capsid proteins, which is directly related to the encapsidation free energy of the polymer as plotted in Fig. 4.5. We emphasize again that the findings of this chapter is not in contradiction with the previous studies: The more strongly branched a polymer is, the more competitive it becomes to be encapsidated by capsid proteins. However, in this work we show that because of base-pairing, the RNA also becomes stiffer and under appropriate conditions can no longer outcompete the linear polymer for binding to capsid proteins.

Since branching due to base-pairing causes both the stiffness and the linear charge density of an otherwise linear polymer to increase, one might wonder which effect, higher charge density or larger stiffness, makes the viral RNA less competitive than a linear polymer. Figure 4.6 distinguishes the effect of stiffness and charge density. The dashed lines in the figure correspond to linear polymers with $\ell = 1nm$ but different numbers of charges per Kuhn segment $\tau = -e, -4e, -10e$. In the plots, the longer the dashes are, the higher the

charge density is. As illustrated in the figure, the encapsidation free energy becomes lower as the charge density increases. The charge density has the same impact on the encapsidation free energy of branched polymers. Figure 4.6 shows that as the charge density of branched polymer increases (dotted lines), their free energy decreases. The more distance between the dots, the higher the charge density of the branched polymer. Quite interestingly, the figure shows that the effect of stiffness overshadows the impact of charge density. A branched polymer with the stiffness of $\ell = 2nm$ and charge density of $\tau = -4e$ or $-10e$ has a higher free energy than a linear polymer with the stiffness of $\ell = 1nm$ but the charge density of $\tau = -4e$. These examples do not correspond to "real" RNA as it is not possible to increase the number of charges to more than $2e$ per base pair, but they clarify that base-pairing has three competing effects. First, it makes RNA stiffer, which increases the work of encapsidation but, second, in parallel gives rise to the branching effect and, third, a higher charge density, which both lowers the encapsidation free energy and enhances the packaging efficiency of RNA by capsid proteins.

Another important point to consider, is the change in the excluded volume interaction that must somehow be connected with the variation in the Kuhn length. We repeated the calculations done for Fig. 4.5, but considered the excluded volume effect, which approximately goes as ℓ^3 [56]. We found that our conclusion is robust and that the excluded volume interaction only slightly modifies the boundary in the parameter space where the linear polymers are able to outcompete the branched ones. The results of this study can explain the intriguing findings of the experiments of Beren *et al.* [106] in which the unstructured polyU RNA is preferentially packaged and outcompetes native RNA CCMV, despite

the fact that viral RNAs have more branch points and as such have a more compact structure. Last but not least we note that the interaction of RNA with capsid proteins could modify the preferred curvature of proteins and result into the capsid of different sizes and T numbers as demonstrated in [106]. However, since very little is known about this effect, in this chapter we exclusively focused on the impact of RNA stiffness resulting from its base pairing in the RNA encapsidation free energy.

4.5 Conclusions

Results of our field theory calculations have shown that competition between different forms of RNA for encapsulation by virus coat proteins is a complex function of the degree of branching, effective stiffness of the polymer, linear charge density and excluded volume interactions. The conclusion of previous works that the more branched an RNA is on account of its secondary, base-paired structure, the larger the competitive edge it has to be encapsulated in the presence of coat proteins needs to be refined. Under appropriate conditions of linear charge density and effective chain stiffness, we find that a linear chain may in fact outcompete even the native RNA of a virus, as was recently also shown experimentally. Of course, our conclusions are based on coarse-grained model in which the RNA binding domains of the coat proteins are represented by a smooth, uniformly charged wall. In future work we intend to more realistically model these polycationic tails that form a complex with the polynucleotide. Of particular interest here is the impact of excluded volume interactions between these tails and the polynucleotide.

Part III

Elasticity Theory for Viral Capsid

Chapter 5

Elasticity in curved topographies: Exact theories and linear approximations

5.1 Introduction

There are many examples of 2D crystals on curved spaces, including colloids absorbed on a spherical surface [43, 112], negative curvature [113] at oil-water interface, virus shells [44, 114, 115] and colloids mixtures [116], just to name a few. The uniqueness of these problems arises from the subtle but profound relation between geometry and topology.

The equilibrium structure of two-dimensional ordered structures on the surfaces of non-zero Gaussian curvature is dictated by the presence and arrangement of defects such as dislocations and disclinations. The energetically forbidden defects in flat surfaces be-

come ubiquitous on curved substrates; nevertheless, their presence gives rise to equilibrium structures that include finite stresses. The standard theory of elasticity [117] is unwieldy to investigate the interplay of the defects and geometry and, often, is not the most suitable starting point for these problems. In fact, in order to satisfy topological constraints, somewhat uncontrolled approximations need to be considered.

In this chapter we develop a geometric theory for elasticity that incorporates topological constraints exactly, thus allowing to calculate the stress and strain in a curved surface and analyze different approximations employed in the literature. Examples that will be discussed include five-fold disclinations in a triangular lattice in the regions of constant positive Gaussian curvature, see Fig.5.1.

The organization of the chapter is as follows: In the following section, we first present different approximations employed in literature to solve elasticity equations and provide a conceptual discussion of our approach, which is developed in Sect. 5.3. As an example, the case of a spherical cap, with or without a central disclination and the derivation of all their relevant analytical formulas are presented in Sect. 5.4. Explicit comparisons between the different approximations and the exact results are presented in Sect. 5.5. Some general conclusions are presented in Sect. 5.6. More technical/mathematical developments are deferred to the appendices, where we have made a special effort in providing all the detail necessary so that all calculations are fully reproducible.

5.2 Formalism: Conceptual Aspects

The basic quantities in elasticity theory are the displacements $\mathbf{u}(\bar{\mathbf{x}})$ from a reference state $\bar{\mathbf{x}}$

$$\mathbf{x} \equiv \bar{\mathbf{x}} + \mathbf{u}(\bar{\mathbf{x}}) \ , \tag{5.1}$$

and the associated strain ($u_{\alpha\beta}$) and stress ($\sigma^{\alpha\beta}$) tensors, which are conjugated variables in the thermodynamic sense [117]. A definition of the strain tensor is given by comparing how a small vector in the *reference* state $d\bar{\mathbf{x}}$ transforms after a mechanical deformation, represented by $d\mathbf{x}$:

$$d\mathbf{x}^2 \quad = \quad d\bar{\mathbf{x}}^2 + 2u_{\alpha\beta} d\bar{\mathbf{x}}^\alpha d\bar{\mathbf{x}}^\beta \ . \tag{5.2}$$

The physical interpretation of this equation is that two particles initially apart by $d\bar{\mathbf{x}}$, after deformation become separated by $d\mathbf{x}$. This equation can be written as a function of two metrics, denoted as reference and target hereon, as follows,

$$g_{\alpha\beta} = \bar{g}_{\alpha\beta} + 2u_{\alpha\beta}. \tag{5.3}$$

While the distances in the reference space are measured according to the metric $\bar{g}_{\alpha\beta}$, after deformation, which defines the *target* space, distances and angles among physical particles change and are determined by the metric $g_{\alpha\beta}$, as illustrated in Fig. 5.1. The strain tensor is the difference between target and reference metrics.

The reference state is defined as a strain and stress free configuration, which is typically taken as $\mathbf{x} = (x, y, z)$ in 3D or $\mathbf{x} = (x, y, z = 0)$ in 2D, which implies an euclidean

reference metric

$$d\bar{\mathbf{x}}^2 = dx^2 + dy^2 + dz^2 \text{ (3D)} \tag{5.4}$$

$$d\bar{\mathbf{x}}^2 = dx^2 + dy^2 \text{ (2D) .} \tag{5.5}$$

Physically, the reference state maybe associated with a lattice where all nearest neighbors are at the same distance and form the same angle. In 2D we associate it with the triangular lattice, see Fig. 5.1. Further below, we will show that the reference state is not unique, as a triangular lattice with topological defects such as disclinations and dislocations is also allowed. We mention, on passing, that in 3D a lattice where all nearest neighbors are at the same distance and form the same angle would consist of a tiling with regular tetrahedra, which is not possible [118] and leads to several consequences that have been discussed elsewhere [119, 120]. Our goal in this chapter is to develop a formalism to obtain the stress and strain in a curved surface. In particular, we focus on how an initially flat monolayer, whose reference state is given by $\bar{\mathbf{x}}$, consisting of a plane with additonal defects, deforms into a given topography $\vec{r}(\bar{\mathbf{x}})$ embedded in 3D space, as illustrated in Fig. 5.1. Note that both the reference metric $d\bar{\mathbf{x}}^2$ and target metric $d\vec{r}^2$ (which, in order to alleviate the notation will be denoted as $d\mathbf{x}^2$ in what it is, certainly, a blatant abuse of language) are known beforehand. We aim at finding the following transformation

$$\mathbf{x} = \mathcal{F}(\bar{\mathbf{x}}) \ , \tag{5.6}$$

which will be obtained by solving the equations of elasticity theory. How this transformation is related to the more familiar quantities in elasticity theory: the stress tensor $\sigma^{\alpha\beta}$, the Airy function (χ) [121] etc.. will be discussed extensively later in the chapter.

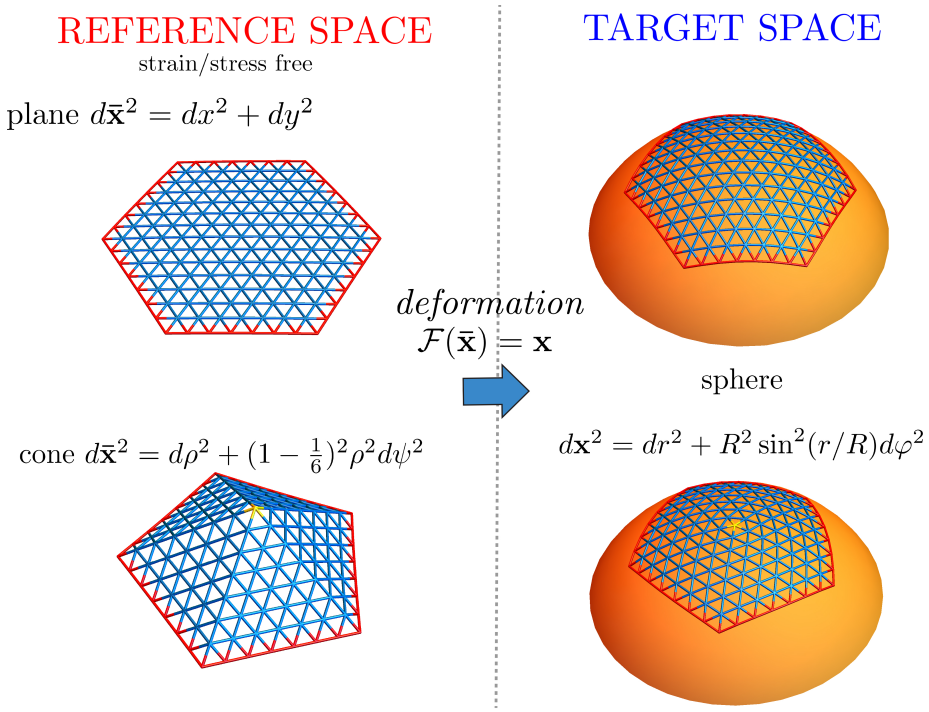

Figure 5.1: Example of reference/target metric and space for a target space consisting of a spherical cap. This problem is solved in Section 5.4.

The problem of finding the transformation given in Eq. 5.6 is quite subtle because of the interplay of curvature, topology and defects such as disclinations or dislocations [121, 122]. For example, in a boundary free crystal, the sum of all disclination charges is related to the Euler characteristic χ_E through the Gauss Bonnet theorem [123]

$$\sum_{i=1}^{M} s_i = \int d^2\mathbf{x}\sqrt{g}K(\mathbf{x}) = 2\pi\chi_E \ , \tag{5.7}$$

where $K(\mathbf{x})$ is the Gaussian curvature, g is the determinant of the surface metric and for a triangular lattice $s_i = \frac{\pi}{3}q_i$ ($q_i = \pm 1$). In case of a spherical surface, $\chi_E = 2$ leading to the well known result that a spherical crystal has an excess of twelve $q_i = 1$ disclinations (pentamers) in the absence of heptamers ($q_i = -1$).

Solutions to the theory of elasticity are obtained mostly within the Foppl Von

Karman theory of elastic plates, which amounts to small displacements from equilibrium positions, an approach we denote as the Euler Framework (EF). A useful quantity to calculate the free energy and stress of a curved object is the Airy stress function. For a crystal consisting of M disclinations at positions $\mathbf{x}_i$ and with charge s_i, the equation for the Airy function is

$$\frac{1}{Y}\Delta^2\chi(\mathbf{x}) = \sum_{i=1}^{M} s_i\delta(\mathbf{x}_i - \mathbf{x}) - K(\mathbf{x}) \ , \tag{5.8}$$

where Δ is the 2D Laplacian on a plane and Y is the Young modulus [117, 124]. Note that the Gaussian curvature of the surface acts as an external field. Relevant solutions to Eq. 5.8 are available for a buckled disclination or dislocation [124], a spherical cap with and without a central disclination [125, 126] and also, for a spherical cap with an off-center disclination [127–129]. We emphasize again that the EF is exact in the limit of small curvature only. More precisely, if r_m is the dimension of the crystal and R some "average" curvature of the surface, the small curvature limit is defined by

$$\alpha \equiv \frac{r_m}{R} = \theta_m << 1 \ . \tag{5.9}$$

In a spherical cap (with constant curvature radius R), a major problem arises as $\alpha \to \pi$, that is, as the spherical cap becomes a full sphere. Because within EF the solution of Eq. 5.8 is defined on a plane for a disk of area $A = \pi r_m^2$, the constraint Eq. 5.7

$$\int d^2\mathbf{x}K(\mathbf{x}) = \int \frac{d^2\mathbf{x}}{R^2} = \frac{A}{R^2} = \pi\alpha^2 \neq 4\pi \ , \tag{5.10}$$

breaks down.

For a full sphere [130], the topological constraint Eq. 5.10 cannot be satisfied within EF. The failure to exactly satisfy a topological constraint is a serious conceptual

problem that typically results in very significant computational errors. In Ref. [131–133] a generalization of Eq. 5.8, which we denote as the Laplace Formalism (LF), was proposed

$$\frac{1}{Y}\Delta_g^2\chi(\mathbf{x}) = \frac{1}{\sqrt{g(\mathbf{x})}}\sum_{i=1}^{M} s_i\delta(\mathbf{x}_i - \mathbf{x}) - K(\mathbf{x}) \ , \tag{5.11}$$

where the Laplacian Δ_g is computed with the target metric, *i.e.*, on the curved surface. Now, for a full sphere, the topological constraint Eq. 5.7 is satisfied identically. Although very successful and highly accurate in many applications [134], the LF appears as an uncontrolled approximation: It is not obvious how to compute next orders so that eventually the exact solution will be recovered. Furthermore, for crystal with boundaries, like a crystal spanning a spherical cap, it is not immediately apparent what additional boundary conditions must be supplemented to Eq. 5.11.

For the reasons exposed, neither the EF nor the LF are entirely satisfactory, despite their many successes. There is a clear need for a more rigorous formalism able to develop the LF as a systematic expansion and from which the EF appears as a low curvature expansion. A first insight on how to develop this formalism is provided by the fact that physical quantities (energies, stresses, strains, etc..) should be independent of surface parameterizations, that is, expressed in terms of geometric invariants, an approach pioneered by Koiter as early as 1966 [135]. An elegant formulation with numerous new insights has been provided in Ref. [136] and extended further in Ref. [137]. In previous papers, see Ref. [138, 139] we have anticipated some aspects of the formalism fully elaborated here.

Before dwelling into the actual formalism, it is worth describing the main ideas and concepts, which are very intuitive despite the significant amount of differential geometry [123] necessary for its rigorous development. As already discussed, both the target

metric $g_{\mu\nu}(\mathbf{x})$ and the reference $\bar{g}_{\mu\nu}(\bar{\mathbf{x}})$ are known, what is therefore needed is the transformation Eq. 5.6 that enables to express the two metrics either as $g_{\mu\nu}(\bar{\mathbf{x}})$ or $\bar{g}_{\mu\nu}(\mathbf{x})$.

A simple counting of the number of variables helps understand the problem better. A general metric has three degrees of freedom g_{11}, g_{22}, g_{12}, so in order to exactly map $\bar{g}_{\mu\nu}$ into $g_{\mu\nu}$ three functions are necessary. The solution of elasticity theory Eq. 5.6 provides only two of them as $\mathcal{F}$ is a 2D mapping. The third function is associated with the Gaussian curvature. If the curvature of the reference and target metrics are not the same, a situation that is called *geometric frustration* or *metric incompatibility*, then it is not possible to make the two metrics $\bar{g}_{\mu\nu}$ and $g_{\mu\nu}$ coincide by Eq. 5.6. Since the Gaussian curvature is a scalar invariant under reparameterizations, metric incompatibility, immediately leads to non-zero strains (and stresses), as obvious from Eq. 5.2.

A few more clarifications are pertinent. First of all, as discussed above, the reference metric represents a strain and stress free configuration. We have already pointed out that a triangular lattice provides a concrete example. However, there are others: a cone with the appropriate aperture angle and $q = 1, 2, 3$ disclination charge at its tip and $q = 0$ (hexamers) everywhere else is also a stress and strain free configuration. In the same way, one can consider a reference metric that contains an arbitrary number of defects, and hence, the associated curvature will be given by the disclination density $s(\bar{\mathbf{x}})$

$$\begin{aligned} \bar{K}(\bar{\mathbf{x}}) &= s(\bar{\mathbf{x}}) = \frac{1}{\sqrt{\bar{g}}} \sum_{j=1}^{M} s_j \delta(\bar{\mathbf{x}} - \bar{\mathbf{x}}^j) \\ &= \frac{1}{\sqrt{\bar{g}}} \left(\sum_{j=1}^{N_D} s_j \delta(\bar{\mathbf{x}} - \bar{\mathbf{x}}^j) + \sum_{i=1}^{N_d} \epsilon^{\alpha\beta} b^i_\alpha \partial_\mu (e_\beta{}^\mu \delta(\bar{\mathbf{x}} - \bar{\mathbf{x}}^i)) \right) \end{aligned} \tag{5.12}$$

where use has been made of vielbeins $e_\beta{}^\mu$, see Appendix B.2. The second equality follows

by separating the M disclinations as N_D isolated disclinations and N_d dislocations, that is, considering tightly bound disclinations as dipoles characterized by a Burgers vector $\vec{b}$. Only for a few cases, such as $N_D = 0, N_d = 0$ (plane), $N_D = 1, N_d = 0$ (cone) or $N_D = k, N_d = 0$ (with $12 \geq k \geq 2$, icosahedral sections), see also the limiting case $N_D = 0, N_d = 1$ [140], it is possible to embed explicit solutions in target space such that $K = \bar{K}$ and therefore, they are strain and stress free. In this form, elasticity solutions amount to expressing a given metric $g_{\alpha\beta}$ as its optimal approximate in terms of "quanta" of disclinations of charge $\frac{\pi}{3}q$ and dislocations of Burgers vector $\mathbf{b}$. In fact, the geometric content of this "quanta" becomes even more explicit by noting that isolated disclinations are "quanta" of Gaussian curvature while dislocations are of geometrical torsion [138, 141].

In this chapter, we will not further discuss the role of dislocations, however, it is worth noting that it is possible to approximate any metric by Eq. 5.12 if $N_d \to \infty$, as demonstrated in Ref. [138]. This corresponds to the limit where Burgers vector $\mathbf{b}$ are infinitesimally small, *i.e.* mean field solutions, also discussed in Ref. [142,143]. In this limit, the *Perfect Curvature Condition* (PCC)

$$K(\mathbf{x}) = s(\mathbf{x}) \tag{5.13}$$

is satisfied. As pointed out in Ref. [113], it has the electrostatic analogy of a continuum of charge $K(\mathbf{x})$ being represented by N_D isolated charges and a continuum of polarization, i.e. $N_d \to \infty$ dipoles. More generally, the quantity

$$\eta(\mathbf{x}) = K(\mathbf{x}) - s(\mathbf{x}) \tag{5.14}$$

is a measure of the geometric frustration or metric incompatibility. The PCC $\eta(\mathbf{x}) = 0$ is

the necessary and sufficient condition for a stress-strain free state to exist in target space. We next develop these ideas in precise mathematical form.

5.3 Formalism: Development

5.3.1 Exact Formulas

As introduced previously, we will consider two metrics, $g_{\mu\nu}(\mathbf{x})$ (target metric) and $\bar{g}_{\mu\nu}(\mathbf{x})$ (reference metric). Both metrics are defined over the same domain $\mathcal{B}_t$, which we denote as the *target* domain. The reference domain $\mathcal{B}_r$ represents the rest frame where the elastic energy is zero. Consistent with our discussion in Sect. 5.2, we will denote as $\mathbf{x}$ the target coordinates and as $\bar{\mathbf{x}}$ the reference coordinates. The solution of the problem is then to determine $\mathcal{F}$ in Eq. 5.6 ($\mathbf{x} = \mathcal{F}(\bar{\mathbf{x}})$).

The most general elastic free energy has the form

$$F = \frac{1}{2} \int_{\mathcal{B}} W\left(g(\mathbf{x}), \bar{g}(\mathbf{x})\right) d\mathrm{V}ol_g \ . \tag{5.15}$$

We now show that an appropriate choice of W leads to the familiar expression for the elastic energy [117], see also Ref. [137]. If Y is the Young modulus and ν_P is the Poisson ratio, the following quantities are defined

$$\begin{aligned} A^{\alpha\beta\gamma\delta} &= \frac{Y}{1-\nu_P^2}\left(\nu_P g^{\alpha\beta} g^{\gamma\delta} + (1-\nu_P) g^{\alpha\gamma} g^{\beta\delta}\right) \\ A_{\alpha\beta\gamma\delta} &= \frac{1}{Y}\left((1+\nu_P) g_{\alpha\gamma} g_{\beta\delta} - \nu_P g_{\alpha\beta} g_{\gamma\delta}\right) \end{aligned} \tag{5.16}$$

in such a way that $A^{\alpha\beta\gamma\delta} A_{\gamma\delta\alpha'\beta'} = g^{\alpha}_{\alpha'} g^{\beta}_{\beta'}$. Then the functional $W\left(g(\mathbf{x}), \bar{g}(\mathbf{x})\right)$ is defined so that it reduces to the standard elastic energy for an isotropic medium, that is

$$W\left(g(\mathbf{x}), \bar{g}(\mathbf{x})\right) = A^{\alpha\beta\gamma\delta} u_{\alpha\beta} u_{\gamma\delta} \ , \tag{5.17}$$

where the strain tensor, see Eq. 5.2, is

$$2u_{\alpha\beta}(\mathbf{x}) = g_{\alpha\beta}(\mathbf{x}) - \bar{g}_{\alpha\beta}(\mathbf{x}) \ . \tag{5.18}$$

Note that the free energy Eq. 5.15 is invariant under general reparameterizations. Working in the target frame, the metric $g_{\alpha\beta}(\mathbf{x})$ is known, so we will derive the equilibrium equations in order to determine the reference metric $\bar{g}_{\mu\nu}(\mathbf{x})$, which, expressed in the target coordinates is not known. The stress tensor is given by

$$\sigma^{\alpha\beta} = \frac{1}{\sqrt{g}}\frac{\delta F}{\delta u_{\alpha\beta}} = A^{\alpha\beta\gamma\delta}u_{\gamma\delta} \ . \tag{5.19}$$

Variations of Eq. 5.15 under reparameterizations (ξ_β) of the reference metric $\delta\bar{g}_{\alpha\beta} = -\bar{\nabla}_\alpha\xi_\beta - \bar{\nabla}_\beta\xi_\alpha$, leaving the target metric invariant gives

$$\begin{aligned} \delta F &= -\frac{1}{2}\int_{\mathcal{B}} d^2\mathbf{x}\sqrt{g}\sigma^{\alpha\beta}\delta\bar{g}_{\alpha\beta} = \int_{\mathcal{B}} d^2\mathbf{x}\sqrt{g}\sigma^{\alpha\beta}\bar{\nabla}_\alpha\xi_\beta \\ &= \int_{\mathcal{B}} d^2\mathbf{x}\left[\frac{\partial}{\partial x_\alpha}\left(\sqrt{g}\sigma^{\alpha\beta}\xi_\beta\right) - \sqrt{\bar{g}}\bar{\nabla}_\alpha\left(\left(\frac{g}{\bar{g}}\right)^{1/2}\sigma^{\alpha\beta}\right)\xi_\beta\right] \end{aligned} \tag{5.20}$$

The first term is a total derivative, and it can be converted to an integral along the boundary

$$\int_{\mathcal{B}} d^2\mathbf{x}\frac{\partial}{\partial x_\alpha}\left(\sqrt{g}\sigma^{\alpha\beta}\xi_\beta\right) = \int_{\partial\mathcal{B}} dx^\rho\sqrt{g}\epsilon_{\rho\gamma}\sigma^{\gamma\beta}\xi_\beta \ . \tag{5.21}$$

Should the boundary contain a line tension term

$$F_l = \gamma\int_{\partial\mathcal{B}} ds \ , \tag{5.22}$$

then

$$\delta F_l = -\gamma\int_{\partial\mathcal{B}} dx^\mu\nabla_\mu t^\nu\xi_\nu \ , \tag{5.23}$$

where t^μ is the unit tangent to the boundary. Taking into account the geometric formula

$$t^\mu \nabla_\mu t^\nu = \frac{1}{r_{\mathcal{B}}} e_\alpha{}^\nu n^\alpha \ , \tag{5.24}$$

with $r_{\mathcal{B}}$ the radius of curvature, n^α the normal and $e_\alpha{}^\nu$ are the vielbeins, see the Appendix B.2. The correct boundary condition is:

$$n_\gamma \hat{\sigma}^{\gamma\nu} = -\frac{\gamma}{r_{\mathcal{B}}} n^\nu, \tag{5.25}$$

where $\hat{\sigma}^{\alpha\beta} = e^\alpha{}_\mu e^\beta{}_\nu \sigma^{\mu\nu}$, see Appendix for the different expressions of the stress tensor and some additional details on the derivation of these formulas. This boundary condition reduces to the one derived for the EF in Ref. [126].

From the definition of the covariant derivative, it is

$$\nabla_\alpha \sigma^{\alpha\beta} = \frac{\partial \sigma^{\alpha\beta}}{\partial x_\alpha} + \Gamma^\alpha_{\alpha\gamma} \sigma^{\gamma\beta} + \Gamma^\beta_{\alpha\gamma} \sigma^{\alpha\gamma} \ . \tag{5.26}$$

Therefore, the equations determining equilibrium are

$$\bar{\nabla}_\alpha \left(\left(\frac{g}{\bar{g}} \right)^{1/2} \sigma^{\alpha\beta} \right) = \bar{\nabla}_\alpha \sigma^{\alpha\beta} + \left(\Gamma^\alpha_{\alpha\gamma} - \bar{\Gamma}^\alpha_{\alpha\gamma} \right) \sigma^{\gamma\beta} = 0 \ , \tag{5.27}$$

which can also be written as

$$\nabla_\alpha \sigma^{\alpha\beta} + \left(\bar{\Gamma}^\beta_{\alpha\gamma} - \Gamma^\beta_{\alpha\gamma} \right) \sigma^{\alpha\gamma} = 0 \ , \tag{5.28}$$

and the appropriate boundary conditions as defined by Eq. 5.25. Here, we have used the Christoffel symbols that are symmetric $\Gamma^\beta_{\alpha\gamma} = \Gamma^\beta_{\gamma\alpha}$.

A general solution to Eq. 5.27 is given by the following ansatz [137]

$$\sigma^{\alpha\beta} = \frac{1}{\sqrt{g}} \frac{1}{\sqrt{\bar{g}}} \epsilon^{\alpha\rho} \epsilon^{\beta\gamma} \bar{\nabla}_\rho \bar{\nabla}_\gamma \chi \ , \tag{5.29}$$

where $\epsilon^{12} = -\epsilon^{21} = 1$ and zero otherwise, and χ is the Airy function. Using the following identity,

$$\frac{1}{g}\epsilon^{\alpha\rho}\epsilon^{\mu\nu} = g^{\alpha\mu}g^{\rho\nu} - g^{\alpha\nu}g^{\rho\mu}, \tag{5.30}$$

Eq. 5.29 can be written as

$$\sigma^{\alpha\beta} = \left(\frac{\bar{g}}{g}\right)^{1/2}\left(\bar{g}^{\alpha\beta}\bar{g}^{\rho\gamma} - \bar{g}^{\alpha\gamma}\bar{g}^{\beta\rho}\right)\bar{\nabla}_\rho\bar{\nabla}_\gamma\chi. \tag{5.31}$$

Using the formula $g^{\rho\gamma}\Gamma^\nu_{\rho\gamma} = -\frac{1}{\sqrt{g}}\partial_\gamma(\sqrt{g}g^{\gamma\nu})$ and the fact that the covariant derivative of the metric is zero, *i.e.*, $\bar{\nabla}_\alpha\bar{g}_{\mu\nu} = 0$, we find

$$\bar{\nabla}_\alpha\sigma^{\alpha\beta} + \left(\Gamma^\alpha_{\alpha\gamma} - \bar{\Gamma}^\alpha_{\alpha\gamma}\right)\sigma^{\gamma\beta} = \frac{1}{\sqrt{g\bar{g}}}\epsilon^{\alpha\rho}\epsilon^{\beta\gamma}\bar{\nabla}_\alpha\bar{\nabla}_\rho\bar{\nabla}_\gamma\chi\ . \tag{5.32}$$

The right hand side of the above equation can be expressed in terms of the Riemann tensor, see Eq. B.39, as follows

$$\begin{aligned}\epsilon^{\alpha\rho}\epsilon^{\beta\gamma}\bar{\nabla}_\alpha\bar{\nabla}_\rho\bar{\nabla}_\gamma\chi &= \frac{1}{2}\epsilon^{\alpha\rho}\epsilon^{\beta\gamma}[\bar{\nabla}_\alpha,\bar{\nabla}_\rho]\bar{\nabla}_\gamma\chi \\ &= \frac{1}{2}\epsilon^{\alpha\rho}\epsilon^{\beta\gamma}\bar{R}^\mu{}_{\gamma\alpha\rho}\bar{\nabla}_\mu\chi = 0\ ,\end{aligned} \tag{5.33}$$

where the last identity follows since the Riemann tensor of the reference metric is zero outside the defect cores, that is, almost everywhere, see Eq. 5.12. Thus, Eq. 5.29 provides a general solution of Eq. 5.27 in terms of the Airy function.

Substituting the solution of Eq. 5.29 into the definition of the strain Eq. 5.18 gives,

$$\frac{1}{\sqrt{g}}\frac{1}{\sqrt{\bar{g}}}\epsilon^{\alpha\rho}\epsilon^{\beta\gamma}\bar{\nabla}_\rho\bar{\nabla}_\gamma\chi = \frac{1}{2}A^{\alpha\beta\gamma\delta}\left(g_{\gamma\delta} - \bar{g}_{\gamma\delta}\right) \tag{5.34}$$

or

$$\begin{aligned}
\bar{g}_{\alpha\beta} &= g_{\alpha\beta} - \frac{2}{\sqrt{g\bar{g}}} A_{\mu\lambda\alpha\beta}\epsilon^{\mu\rho}\epsilon^{\lambda\gamma}\bar{\nabla}_\rho\bar{\nabla}_\gamma\chi \\
\bar{g}_{\alpha\beta} &= g_{\alpha\beta} - \frac{2}{Y}\left(\frac{g}{\bar{g}}\right)^{1/2}\left[g_{\alpha\beta}g^{\rho\gamma} - (1+\nu_P)g^\gamma_\alpha g^\rho_\beta\right]\bar{\nabla}_\rho\bar{\nabla}_\gamma\chi
\end{aligned} \tag{5.35}$$

Thus $\bar{g}_{\mu\nu}(\chi(\mathbf{x}))$ can be obtained from above equation. Note however, that among all possible functions χ, there is only one that has the right curvature $\bar{K}$, so the equation above needs to be supplemented with the additional constraint

$$2\bar{K} = \bar{R} = \bar{g}^{\mu\nu}\bar{R}_{\mu\nu} = \bar{g}^{\mu\nu}\bar{R}^\rho{}_{\mu\rho\nu} = 0 \ , \tag{5.36}$$

which uniquely determines χ. Here $\bar{K} = s(\mathbf{x})$ is the Gaussian curvature, $\bar{R}$ the scalar curvature, $\bar{R}_{\mu\nu}$ the Ricci tensor and $\bar{R}^\rho{}_{\mu\gamma\nu}$ the Riemann tensor. That is, the solution consists among all possible functions of χ, to select the one that makes $\bar{g}_{\mu\nu}$ a flat metric. In general, such solution is complicated as $\bar{g}_{\mu\nu}$ appears on both sides of the equation, and the rhs includes its derivatives.

Using Eqs. 5.17-5.19 and 5.35, the expression for the elastic energy (Eq. 5.15) without any approximations is,

$$\begin{aligned}
F &= \frac{1}{2}\int_{\mathcal{B}} \sigma^{\alpha\beta}A_{\alpha\beta\rho\sigma}\sigma^{\rho\sigma}d\mathrm{Vol}_g \\
&= \frac{1}{2Y}\int_{\mathcal{B}} d\mathrm{Vol}_g \frac{g}{\bar{g}}\left((1+\nu_p)g^{\alpha\rho}g^{\beta\sigma} - \nu_p g^{\alpha\beta}g^{\rho\sigma}\right)\times\bar{\nabla}_\alpha\bar{\nabla}_\beta\chi\bar{\nabla}_\rho\bar{\nabla}_\sigma\chi
\end{aligned} \tag{5.37}$$

note that up to this point all formulas are exact. We now discuss some common approximations.

5.3.2 Incompatibility metric approximation

target frame

Since the actual metric $g_{\mu\nu}(\mathbf{x})$ is known, the goal is to compute the reference metric $\bar{g}_{\mu\nu}(\mathbf{x})$, and from there, one can obtain the transformation Eq. 5.6. If one assumes that η, see Eq. 5.14, is somehow small, the Airy function and the metric are:

$$\chi = \chi^{(1)} + \chi^{(2)} + \cdots \tag{5.38}$$

$$\bar{g} = g + g^{(1)} + g^{(2)} + \cdots , \tag{5.39}$$

where each term contains increasing powers of η. Obviously the Airy function is at least, linear with η, as for $\eta = 0$, $\chi = 0$ and $g = \bar{g}$. Plugging this expansion into the Airy equation 5.35 provides the explicit orders in the expansion. The first order is

$$g^{(1)}_{\alpha\beta} = -\frac{2}{Y}\left(g_{\alpha\beta}\Delta\chi^{(1)} - (1+\nu_P)\nabla_\alpha\nabla_\beta\chi^{(1)}\right) , \tag{5.40}$$

where $\Delta = g^{\alpha\beta}\nabla_\alpha\nabla_\beta = \frac{1}{\sqrt{g}}\partial_\alpha(g^{\alpha\beta}\sqrt{g}\partial_\beta)$ is the Laplace-Beltrami operator. Higher orders are discussed in the Appendix B.3. The goal is now to derive an explicit equation for $\chi^{(i)}$, as discussed below.

First order expressions for energy and stress: target frame

With the metric expressed linearly in terms of the Airy function, the next step is to enforce the constraint Eq. 5.36. For this purpose, it is necessary to compute the scalar curvature. This calculation is relegated to Appendix B.3, and gives

$$\bar{K} = K + \frac{1}{Y}\left(\Delta^2\chi^{(1)} + 2K\Delta\chi^{(1)} + (1+\nu_p)g^{\mu\lambda}\nabla_\mu K\nabla_\lambda\chi^{(1)}\right) . \tag{5.41}$$

In addition to the square of Laplacian in the above equation there are additional terms that will be explored further below. The stress tensor within this order is

$$\sigma^{\alpha\beta} = g^{\alpha\beta}\Delta\chi^{(1)} - g^{\alpha\mu}g^{\beta\nu}\nabla_\mu\nabla_\nu\chi^{(1)} \ , \tag{5.42}$$

and the energy

$$F = \frac{1}{2Y}\int d^2u\sqrt{g}\left[(\Delta\chi^{(1)})^2 + \frac{(1+\nu_P)}{g}\epsilon^{\alpha\sigma}\epsilon^{\rho\beta}\nabla_\alpha\nabla_\beta\chi^{(1)}\nabla_\rho\nabla_\sigma\chi^{(1)}\right]. \tag{5.43}$$

As elaborated in Appendix B.4, may be expressed as

$$\begin{aligned} F &= \frac{1}{2Y}\int d^2u\sqrt{g}(\Delta\chi^{(1)})^2 - \\ &- \frac{1+\nu_p}{2Y}\int d^2u\sqrt{g}Kg^{\alpha\beta}\nabla_\alpha\chi^{(1)}\nabla_\beta\chi^{(1)} - \frac{1+\nu_p}{2Y}\oint dx^\rho\sqrt{g}\epsilon_{\rho\alpha}\sigma^{\alpha\beta}\nabla_\beta\chi^{(1)}. \end{aligned} \tag{5.44}$$

A variation on the previous expansion consists in dropping the cross terms involving $K\chi$ in Eq. 5.41. The resulting equations are

$$\bar{K} = K + \frac{1}{Y}\Delta^2\chi^{(1)} \ , \tag{5.45}$$

with corresponding energy

$$F = \frac{1}{2Y}\int d^2u\sqrt{g}(\Delta\chi^{(1)})^2 - \frac{1+\nu_p}{2Y}\oint dx^\rho\sqrt{g}\epsilon_{\rho\alpha}\sigma^{\alpha\beta}\nabla_\beta\chi^{(1)} \ , \tag{5.46}$$

which we recognize as the LF discussed in Sect. 5.2. Note that in the absence of line tension or external stress, the boundary conditions determine that the second term vanishes identically. Hereon, we will refer the approximation Eq. 5.41 as the Incompatibility Framework (IF) in order to differentiate it from the LF.

reference frame

The expansion for the metric and the Airy function is

$$\chi = \chi^{(I)} + \chi^{(II)} + \cdots \tag{5.47}$$

$$g = \bar{g} + \bar{g}^{(I)} + \bar{g}^{(II)} + \cdots \tag{5.48}$$

Similarly as in the target approximation Eq. 5.40, the first order is

$$\bar{g}^{(I)}_{\alpha\beta} = \frac{2}{Y}\left(\bar{g}_{\alpha\beta}\bar{\Delta}\chi^{(I)} - (1+\nu_P)\bar{\nabla}_\alpha\bar{\nabla}_\beta\chi^{(I)}\right) , \tag{5.49}$$

with $\bar{\Delta}$ being the Laplace-Beltrami operator of the reference metric. Higher orders are discussed in the appendix B.3.

First order expressions for energy and stress: reference frame

The formulas derived in the previous case automatically translate into the reference frame by replacing $g_{\alpha\beta} \leftrightarrow \bar{g}_{\alpha\beta}$ and $\chi^{(1)} \rightarrow -\chi^{(I)}$, leading to

$$K = \bar{K} - \frac{1}{Y}\left(\bar{\Delta}^2\chi^{(I)} + 2\bar{K}\bar{\Delta}\chi^{(I)} + (1+\nu_p)\bar{g}^{\mu\lambda}\bar{\nabla}_\mu\bar{K}\bar{\nabla}_\lambda\chi^{(I)}\right) \tag{5.50}$$

The stress tensor within this order is

$$\sigma^{\alpha\beta} = \bar{g}^{\alpha\beta}\bar{\Delta}\chi^{(I)} - \bar{g}^{\alpha\mu}\bar{g}^{\beta\nu}\bar{\nabla}_\mu\bar{\nabla}_\nu\chi^{(I)} , \tag{5.51}$$

and the energy

$$F = \frac{1}{2Y}\int d^2u\sqrt{\bar{g}}\left[(\bar{\Delta}\chi^{(I)})^2 + \frac{(1+\nu_P)}{\bar{g}}\epsilon^{\alpha\sigma}\epsilon^{\rho\beta}\bar{\nabla}_\alpha\bar{\nabla}_\beta\chi^{(I)}\bar{\nabla}_\rho\bar{\nabla}_\sigma\chi^{(I)}\right] . \tag{5.52}$$

Given the assumptions about the reference metric, see Eq. 5.12, the above equations simplify to

$$\frac{1}{Y}\bar{\Delta}^2\chi^{(I)} = \bar{K} - K \tag{5.53}$$

and energy

$$F = \frac{1}{2Y}\int d^2u\sqrt{\bar{g}}(\bar{\Delta}\chi^{(I)})^2 \tag{5.54}$$

where $\bar{\Delta}$ is the Laplacian on the plane. Thus, the reference frame expansion coincides with the EF discussed in Sect. 5.2. The singular terms in Eq. 5.12 can be dropped from the second term in Eq. 5.52 as they only contribute within the defect cores. These contributions are accounted by an empirical core energy term E_{core} as linear elasticity breaks down.

5.4 Results

As a concrete example, we will solve the case of a crystal on a sphere of radius R, as illustrated in Fig. 5.1. The extent of the crystal is parameterized by its aperture angle θ_M. This problem has been described previously within the EF by Morozov and Bruinsma [126] as well as Grason [128]. In the current notation, the Gaussian curvature is $K = \frac{1}{R^2}$ and $\bar{K}$ the disclination density $\bar{K} = s(\mathbf{r})$. The reference frame metric is Euclidean and is defined over a disk of radius ρ_0 by

$$ds^2 = d\rho^2 + \rho^2\left(1 - \frac{s}{2\pi}\right)^2 d\psi^2 \equiv \bar{g}_{\mu\nu}d\bar{x}^\mu d\bar{x}^\nu \ . \tag{5.55}$$

The case $s = \frac{\pi}{3}q_i$ corresponds to a disclination of positive charge placed at the center of the disk. The target metric is

$$ds^2 = dr^2 + R^2\sin^2(r/R)d\varphi^2 \equiv g_{\mu\nu}dx^\mu dx^\nu \ . \tag{5.56}$$

The problem then consists in finding the function $\mathcal{F}$ such that

$$x^\mu = \mathcal{F}(\bar{x}^\mu) \ , \tag{5.57}$$

where $x^\mu = (r, \varphi)$ and $\bar{x}^\mu = (\rho, \psi)$. We will investigate symmetric solutions where $\psi = \varphi$

$$r \equiv r(\rho) = F(\rho) \ , \tag{5.58}$$

so that the problem becomes one dimensional.

5.4.1 Exact Solution

We will discuss symmetric solutions defined by Eq. 5.58 and we will calculate $\rho(r)$. The reference metric is

$$ds^2 = d\rho^2 + \rho^2 d\psi^2 \equiv (\rho'(r))^2 dr^2 + w^2 \rho^2(r) d\varphi^2 \tag{5.59}$$

where $\rho' = d\rho/dr$, $w \equiv 1 - \frac{s}{2\pi}$ and the reference metric is expressed in target coordinates. The non-zero Christoffel symbols are:

symbol	Γ^r_{rr}	$\Gamma^r_{\varphi\varphi}$	$\Gamma^\varphi_{\varphi r}$
reference	$\frac{\rho''(r)}{\rho'(r)}$	$-w^2 \frac{\rho(r)}{\rho'(r)}$	$\frac{\rho'(r)}{\rho(r)}$
target	0	$-R\sin(r/R)\cos(r/R)$	$\frac{\cot(r/R)}{R}$

(5.60)

The components of the stress tensor Eq. 5.19 is the difference between the target and reference metric, that is

$$\begin{aligned}
\sigma^{rr} &= \frac{Y}{2(1-\nu_p^2)} \left[1 - \rho'(r)^2 + \nu_p \left(1 - \left(\frac{w\rho(r)}{R\sin(r/R)} \right)^2 \right) \right] \\
\sigma^{r\varphi} &= 0 \\
\sigma^{\varphi\varphi} &= \frac{Y}{2(1-\nu_p^2) R^2 \sin^2(r/R)} \times \left[1 - \left(\frac{w\rho(r)}{R\sin(r/R)} \right)^2 + \nu_p (1 - \rho'(r)^2) \right] \ .
\end{aligned} \tag{5.61}$$

Inserting Eq. 5.60 into Eq. 5.27 we obtain

$$\frac{d\sigma^{rr}}{dr} + \Gamma^{\varphi}_{\varphi r}\sigma^{rr} + \bar{\Gamma}^{r}_{rr}\sigma^{rr} + \bar{\Gamma}^{r}_{\varphi\varphi}\sigma^{\varphi\varphi} = 0, \tag{5.62}$$

which becomes

$$\frac{d\sigma^{rr}}{dr} + \left(\frac{\cot\left(\frac{r}{R}\right)}{R} + \frac{\rho''(r)}{\rho'(r)}\right)\sigma^{rr} - \frac{w^2\rho(r)}{\rho'(r)}\sigma^{\varphi\varphi} = 0. \tag{5.63}$$

Introducing Eq. 5.61 into Eq. 5.63 yields a nonlinear ordinary differential equation for $\rho(r)$

$$\begin{aligned}
&\frac{2vw^2}{R^2\sin(\frac{r}{R})^2}\rho(r)^2\left(\frac{\cot(\frac{r}{R})}{R} - \frac{\rho'(r)}{\rho(r)}\right) - 2\rho'(r)\rho''(r) \\
&+ \left(\frac{\cot(\frac{r}{R})}{R} + \frac{\rho''(r)}{\rho'(r)}\right) \times \left[1 - \rho'(r)^2 + v\left(1 - \frac{w^2\rho(r)^2}{R^2\sin(\frac{r}{R})^2}\right)\right] \\
&- w^2\frac{\rho(r)}{\rho'(r)}\frac{1}{R^2\sin(\frac{r}{R})^2} \times \left[1 - \frac{w^2\rho(r)^2}{R^2\sin(\frac{r}{R})^2} + v - v\rho'(r)^2\right] = 0
\end{aligned} \tag{5.64}$$

with boundary conditions $\rho(0) = 0$ and $\sigma^{rr}(\theta_m R) = \frac{Y}{1-\nu_p^2}\left[1 - \rho'(\theta_m R)^2 + v\left(1 - \frac{w^2\rho(\theta_m R)^2}{R^2\sin(\theta_m)^2}\right)\right] = 0$. Although within this formalism the Airy function is not necessary to calculate the stress, its actual form is valuable as a comparison with its approximations. It is given as:

$$\begin{aligned}
\sigma^{rr} &= \frac{1}{R\sin(r/R)w\rho(r)\rho'(r)}\bar{\nabla}^2_{\varphi}\chi = \frac{w}{R\sin(r/R)\rho'(r)^2}\frac{d\chi}{dr} \\
\sigma^{\varphi\varphi} &= \frac{1}{R\sin(r/R)w\rho'(r)\rho(r)}\left(\frac{d^2\chi}{dr^2} - \frac{\rho''(r)}{\rho'(r)}\frac{d\chi}{dr}\right)
\end{aligned} \tag{5.65}$$

where $\sigma^{r\varphi} = 0$ is satisfied identically. Note that only one of the equations needs to be satisfied, as the other becomes then an identity.

5.4.2 Incompatibility metric approximation solutions

Reference frame

The equations describing the Airy function for a disclination of charge s in the reference frame have been described above, namely

$$\bar{\Delta}^2\chi^{(I)} + Y(K - s(\mathbf{r})) = 0 \ . \tag{5.66}$$

The solution can be read directly from Ref. [126], and it is given by

$$\chi^{(I)}(\rho) = \frac{Y}{64R^2}\left(2\rho_0^2\rho^2 - \rho^4\right) + \frac{Ys}{8\pi}\rho^2\left(\log(\rho/\rho_0) - \frac{1}{2}\right) \ , \tag{5.67}$$

where $\rho_0 = R\theta_m$ is the radius of the crystal. This is a double expansion in the small parameters ρ_0^2/R^2 and $s/(2\pi)$.

Substitution of Eq. 5.67 into Eq. 5.49 gives

$$\begin{aligned}
\bar{g}_{rr}^{(I)} &= \frac{1}{8R^2}(\rho_0^2 - \rho^2 + \nu_p(3\rho^2 - \rho_0^2)) - \frac{s}{2\pi}\nu_p + \frac{s}{2\pi}(1-\nu_p)\log(\frac{\rho}{\rho_0}), \\
\bar{g}_{\phi\phi}^{(I)} &= w^2\rho^2\left(\frac{1}{8R^2}(\rho_0^2 - 3\rho^2 + \nu_p(\rho^2 - \rho_0^2)) + \frac{s}{2\pi} + \frac{s}{2\pi}(1-\nu_p)\log(\frac{\rho}{\rho_0})\right) \ .
\end{aligned} \tag{5.68}$$

The target frame metric becomes

$$\begin{aligned}
g_{rr} &= \bar{g} + \bar{g}_{rr}^{(I)} \\
&= 1 + \frac{1}{8R^2}(\rho_0^2 - \rho^2 + \nu_p(3\rho^2 - \rho_0^2)) - \frac{s}{2\pi}\nu_p + \frac{s}{2\pi}(1-\nu_p)\log(\frac{\rho}{\rho_0}) \\
&\equiv r'(\rho)^2, \\
g_{\phi\phi} &= \bar{g}_{\phi\phi} + \bar{g}_{\phi\phi}^{(I)} \\
&= w^2\rho^2 + w^2\rho^2\left(\frac{1}{8R^2}(\rho_0^2 - 3\rho^2 + \nu_p(\rho^2 - \rho_0^2)) + \frac{s}{2\pi} + \frac{s}{2\pi}(1-\nu_p)\log(\frac{\rho}{\rho_0})\right) \\
&\equiv \sin^2(r(\rho)) \ .
\end{aligned} \tag{5.69}$$

Using the transformation properties of $g(\bar{x})_{\mu\nu}$ in terms of $\mathcal{F}$ in Eq. 5.6, we obtain

$$r(\rho) = \rho\left(1+\frac{1}{16R^2}(\rho_0^2-\frac{\rho^2}{3}+\nu_p(\rho^2-\rho_0^2))-\frac{s}{4\pi}+\frac{s}{4\pi}(1-\nu_p)\log(\frac{\rho}{\rho_0})\right) , \quad (5.70)$$

which is inverted to give the complete solution,

$$\rho(r) = r\left(1-\frac{1}{16R^2}((\theta_m R)^2-\frac{r^2}{3}+\nu_p(r^2-(\theta_m R)^2))+\frac{s}{4\pi}-\frac{s}{4\pi}(1-\nu_p)\log(\frac{r}{\theta_m R})\right) . \quad (5.71)$$

The stresses are then found using Eq. 5.51

$$\begin{aligned} \sigma^{\rho\rho} &= \frac{Y}{16R^2}(\rho_0^2-\rho^2)+\frac{Ys}{4\pi}\log(\frac{\rho}{\rho_0}) \\ \rho^2\sigma^{\psi\psi} &= \frac{Y}{16R^2}(\rho_0^2-3\rho^2)+\frac{Ys}{4\pi}\left(1+\log(\frac{\rho}{\rho_0})\right) \end{aligned} \quad (5.72)$$

and the free energy from Eq. 5.54 becomes,

$$\begin{aligned} \frac{F}{\pi\rho_0^2 Y} &= \frac{\theta_m^4}{384}+\frac{1}{32}(\frac{s^2}{\pi^2}-\frac{s}{2\pi}\theta_m^2) \\ \frac{F}{\text{Area}\cdot Y} &= \frac{\theta_m^4}{1536}+\frac{1}{32}\left(\frac{s}{\pi}-\frac{\theta_m^2}{4}\right)^2 . \end{aligned} \quad (5.73)$$

The limit $\theta_m \to 0$ (flat limit) agrees with previous results [124].

Target frame

With the assumptions that $\psi = \varphi$, the target metric becomes

$$ds^2 = (\mathcal{F}'(\rho))^2 d\rho^2 + \sin^2(\mathcal{F}(\rho))d\psi^2 \quad (5.74)$$

The equations for the Airy function are either Eq. 5.41 (IF) or Eq. 5.45 (LF), namely

$$\begin{aligned} \Delta^2\chi_{IF}^{(1)}+\frac{2}{R^2}\Delta\chi_{IF}^{(1)} &= s(\mathbf{x})-\frac{1}{R^2} \text{ (IF)} \\ \Delta^2\chi_{LF}^{(1)} &= s(\mathbf{x})-\frac{1}{R^2} \text{ (LF)} \end{aligned} \quad (5.75)$$

where $s(\mathbf{x})$ is the disclination density.

The solutions to Eq. 5.75 is

$$\begin{aligned}\chi^{(1)}_{IF}(r)/(YR^2) &= \log(\cos(\frac{r}{2R})) - \log(\cos(\frac{\theta_m}{2})) - \frac{1}{2}\cos(\frac{r}{R})\csc(\theta_m)\tan(\frac{\theta_m}{2}) + \frac{1}{2}\cot(\theta_m)\tan(\frac{\theta_m}{2}) \\ &+ \frac{s}{2\pi}\left[\sin^2(\frac{r}{2R})\log(\frac{\tan(\frac{r}{2R})}{\tan(\frac{\theta_m}{2})}) - \frac{1}{2}\sin^2(\frac{r}{2R})\sec^2(\frac{\theta_m}{2}) + \frac{1}{2}\tan^2(\frac{\theta_m}{2})\right] \qquad (5.76)\end{aligned}$$

and also

$$\begin{aligned}\chi^{(1)}_{LF}(r)/(YR^2) &= \mathrm{Li}_2(\sin^2(\frac{r}{2R})) - \mathrm{Li}_2(\sin^2(\frac{\theta_m}{2})) - \cot^2(\frac{\theta_m}{2})\log(\frac{1+\tan^2(\frac{r}{2R})}{1+\tan^2(\frac{\theta_m}{2})})\log(1+\tan^2(\frac{\theta_m}{2})) \\ &+ \frac{s}{2\pi}\Big[\mathrm{Li}_2(-\tan^2(\frac{r}{2R})) - \mathrm{Li}_2(-\tan^2(\frac{\theta_m}{2})) \\ &+ \log(\tan(\frac{r}{2R}))\log(1+\tan^2(\frac{r}{2R})) - \log(\tan(\frac{\theta_m}{2}))\log(1+\tan^2(\frac{\theta_m}{2})) \\ &+ 2\log(\cos(\frac{r}{2R}))\left(\cot^2(\frac{\theta_m}{2})\log(\cos(\frac{\theta_m}{2})) + \log(\sin(\frac{\theta_m}{2}))\right) \\ &- 2\log(\cos(\frac{\theta_m}{2}))\left(\cot^2(\frac{\theta_m}{2})\log(\cos(\frac{\theta_m}{2})) + \log(\sin(\frac{\theta_m}{2}))\right)\Big] \ , \qquad (5.77)\end{aligned}$$

with Li_2 the dilogarithmic function. It is relevant at this point to compare the Airy function in target space with the one in reference space; the difference between both gives an idea of the errors involved in the coresponding approximations. Using Eq. 5.67 by expanding Eq. 5.77 to the next orders gives

$$\begin{aligned}\chi^{(1)}_{IF}(x)/(YR^2) &= -\frac{1}{64}(x^2-\theta_m^2)^2 + \frac{s}{16\pi}(\theta_m^2 - x^2 + 2x^2\log(\frac{x}{\theta_m})) \\ &- \frac{1}{384}(\theta_m^6 - 2x^2\theta_m^4 + x^4\theta_m^2) + \frac{s}{192\pi}(3x^4 + 2\theta_m^4 - 5x^2\theta_m^2 - 2x^4\log(\frac{x}{\theta_m})) \\ \chi^{(1)}_{LF}(x)/(YR^2) &= -\frac{1}{64}(x^2-\theta_m^2)^2 + \frac{s}{16\pi}(\theta_m^2 - x^2 + 2x^2\log(\frac{x}{\theta_m})) \\ &- \frac{1}{2304}(\theta_m^6 + 2x^6 - 3x^4\theta_m^2) + \frac{s}{384\pi}(\theta_m^4 - x^2\theta_m^2 + 2x^4\log(\frac{x}{\theta_m})), \qquad (5.78)\end{aligned}$$

with $x = r/R$. It is important to note that there are only linear terms in disclination charge s, but higher orders in x and θ_M. This is basically due to the fact that defects in both IF and LF appear linearly, but, the displacements do not need to be small. The explicit form

of the stresses can be found using Eq. 5.42

$$\sigma^{rr}_{IF}(r)/Y = \frac{1}{4}\cos(\frac{r}{R})\left[-\sec^2(\frac{r}{2R}) + \sec^2(\frac{\theta_m}{2}) + \frac{s}{2\pi}\left(2\log(\frac{\tan(\frac{r}{2R})}{\tan(\frac{\theta_m}{2})}) + \sec^2(\frac{r}{2R}) - \sec^2(\frac{\theta_m}{2})\right)\right],$$

$$R^2\sin^2(\frac{r}{R})\sigma^{\phi\phi}_{IF}(r)/Y = \frac{s}{2\pi} - \frac{1}{2} + \frac{1}{4}\cos(\frac{r}{R})\left[\sec^2(\frac{r}{2R}) + \sec^2(\frac{\theta_m}{2})\frac{s}{2\pi}\left(2\log(\frac{\tan(\frac{r}{2R})}{\tan(\frac{\theta_m}{2})}) - \sec^2(\frac{r}{2R}) - \sec^2(\frac{\theta_m}{2})\right)\right] \tag{5.79}$$

and

$$\sigma^{rr}_{LF}(r)/Y = \frac{1}{2}\sec^2(\frac{r}{2R})\cos(\frac{r}{R}) \times \left[-\cot^2(\frac{r}{2R})\log(\cos^2(\frac{r}{2R})) + \cot^2(\frac{\theta_m}{2})\log(\cos^2(\frac{\theta_m}{2})) + \frac{s}{2\pi}\left(\log(\frac{\tan(\frac{r}{2R})}{\tan(\frac{\theta_m}{2})}) + \csc^2(\frac{r}{2R})\log(\cos(\frac{r}{2R})) - \csc^2(\frac{\theta_m}{2})\log(\cos(\frac{\theta_m}{2}))\right)\right],$$

$$R^2\sin^2(\frac{r}{R})\sigma^{\phi\phi}_{LF}(r)/Y = 1 + \frac{1}{2}\sec^2(\frac{r}{2R}) \times \left[\cot^2(\frac{r}{2R})\log(\cos^2(\frac{r}{2R})) + \cot^2(\frac{\theta_m}{2})\log(\cos^2(\frac{\theta_m}{2})) + \frac{s}{2\pi}\left(\log(\frac{\tan(\frac{r}{2R})}{\tan(\frac{\theta_m}{2})}) - \cos(\frac{r}{R})\csc^2(\frac{r}{2R})\log(\cos(\frac{r}{2R})) - \csc^2(\frac{\theta_m}{2})\log(\cos(\frac{\theta_m}{2}))\right)\right], \tag{5.80}$$

which we thoroughly analyze in the next section.

5.5 Discussion

We now present approximate solutions and compare them to those of the exact equations, and analyze each quantity in turn.

5.5.1 The function $\mathcal{F}$

This function defines how distances between particles in reference frame are transformed in target space. We have not been able to find an analytical expression for the exact

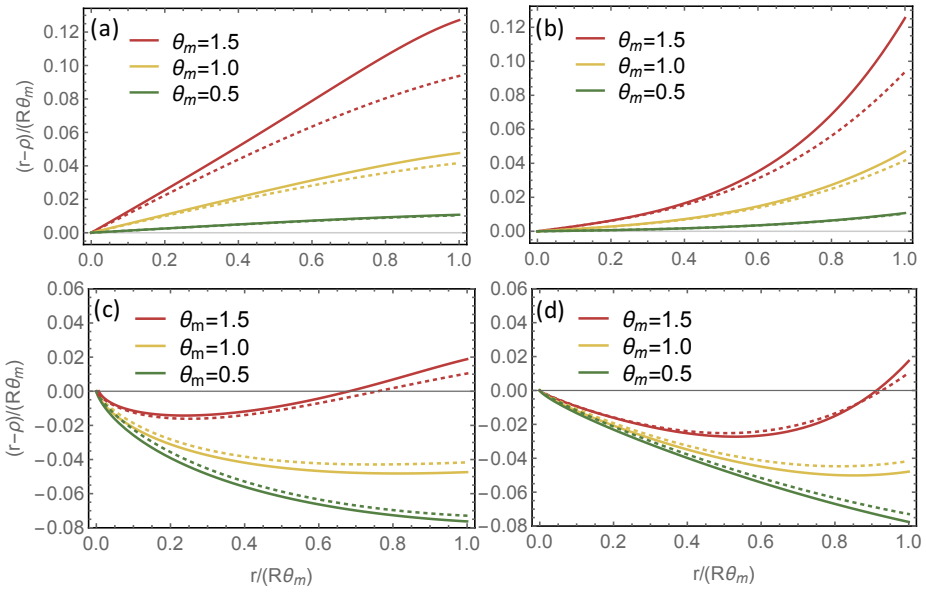

Figure 5.2: The difference between target and reference coordinate $(r - \rho(r))$ as a function of the target coordinate (r) for different values of disclination charge s and Poisson ratio ν_p (a) $[s = 0,\ \nu_p = 0.2]$, (b) $[s = 0,\ \nu_p = 0.8]$, (c) $[s = \frac{\pi}{3},\ \nu_p = 0.2]$ and (d) $[s = \frac{\pi}{3},\ \nu_p = 0.8]$. The solid lines correspond to the exact result Eq. 5.64 while the dotted lines denote the EF solution Eq. 5.71.

Eq. 5.64, which we could nevertheless solve numerically. In Fig. 5.2 we compare it to the EF solution defined by Eq. 5.71. In order to visualize the difference, the figures are shown as a function of $r - \rho(r)$. Quite interestingly, the EF mapping shows very small errors, certainly for $\theta_m < 0.1$, which corresponds to an aperture angle of 60 degrees. Even for $\theta_m \sim 1.5$ (half the sphere), the linear approximation does extremely well when a disclination is present, which is expected as the disclination charge screens the Gaussian curvature, so that the geometric frustration parameter η, see Eq. 5.14, is small and subsequent corrections to the linear contribution become very small.

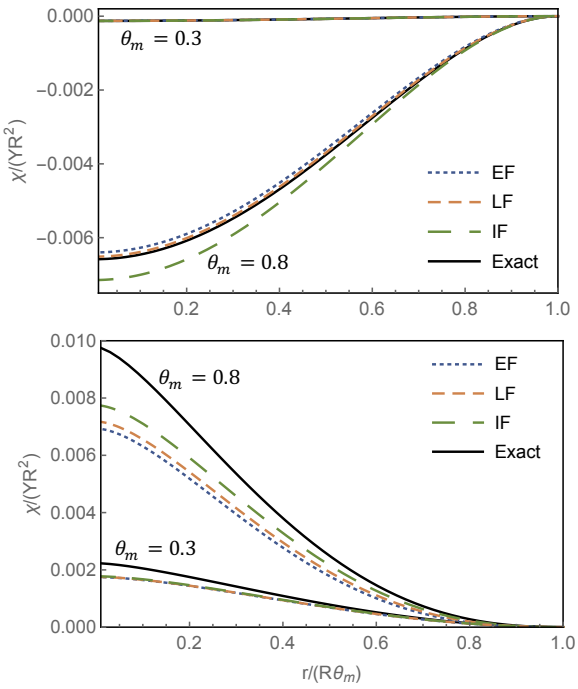

Figure 5.3: χ as function of r (target frame) or ρ (reference frame) corresponding to cap sizes $\theta_m = 0.8$ and $\theta_m = 0.3$. The upper figure denotes to $s = 0$ and lower one with $s = \pi/3$.

5.5.2 Airy function and stresses

The Airy function, computed with the different approximations, namely EF (Eq. 5.67), IF (Eq. 5.76) and LF (Eq. 5.77) is shown in Fig. 5.3 for two different values of the aperture angle (cap size). Small but significant differences are observed for larger caps.

The stresses show similar trends as observed for the Airy function illustrated in Fig. 5.4. As expected, for large values of the apeture angle the exact result is in much better agreement with the case of a disclination at the center (note the different scales in the plot).

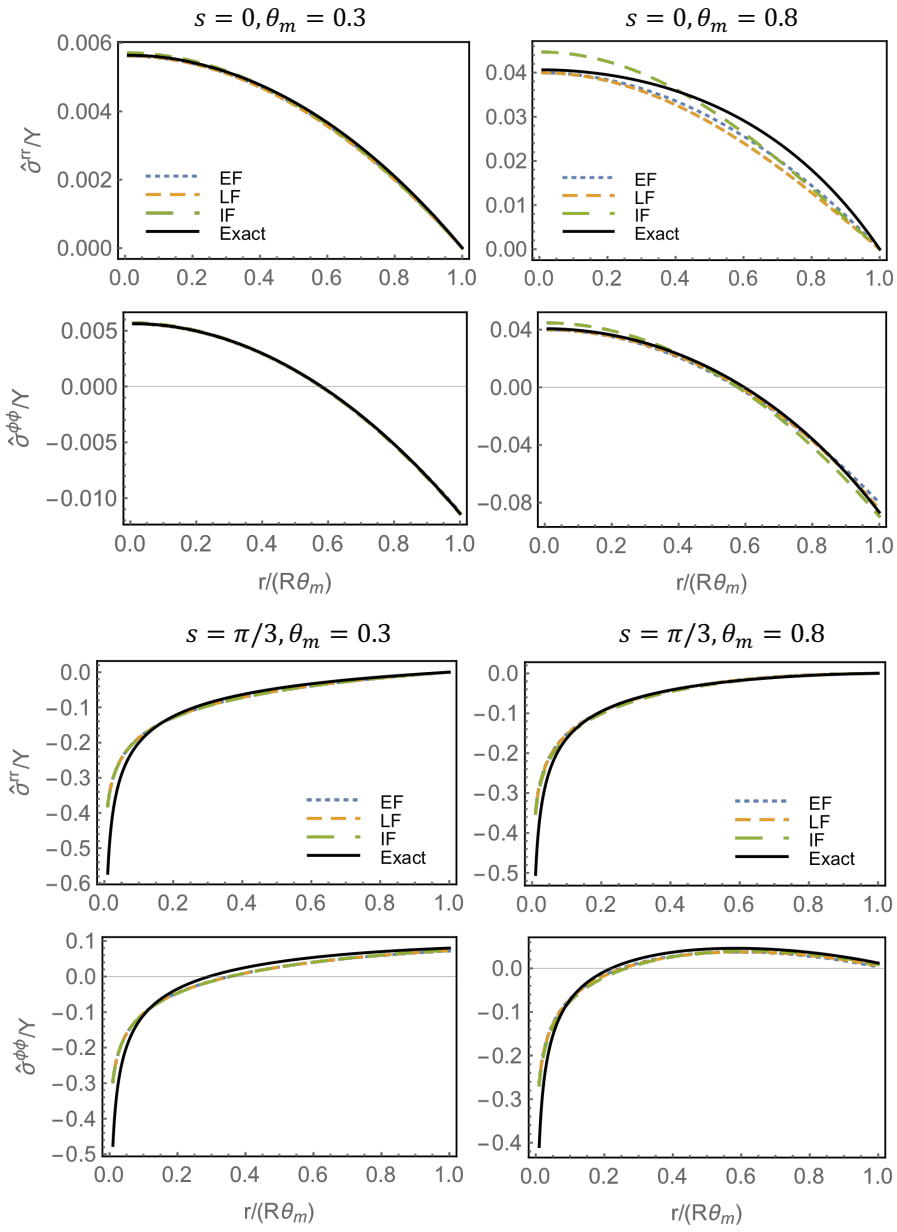

Figure 5.4: Stress σ^{rr} and $\sigma^{\phi\phi}$ with small cap size ($\theta = 0.3$, left column) and large cap size ($\theta = 1.0$, right column). The top four plots of stress correspond to zero disclination and four bottom plots to a single disclination at the center.

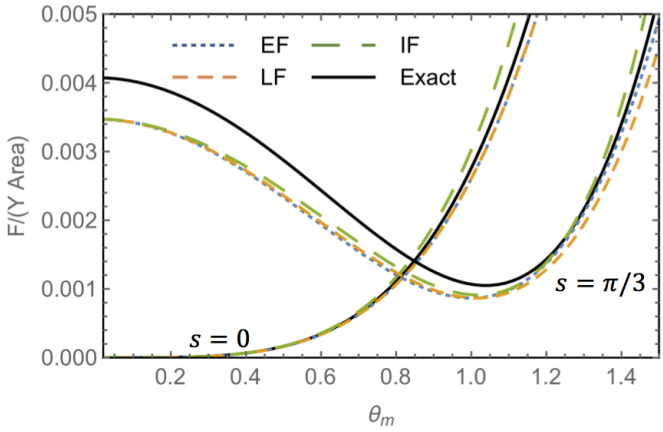

Figure 5.5: Free energy per unit area for $s = 0$ and $s = \frac{\pi}{3}$ for different model presented in the chapter.

5.5.3 Energy

The values for the total free energy are shown in Fig. 5.5 as a function of the aperture angle θ_m . As expected, in the flat limit $\theta_m \to 0$, the EF, LF and IF all converge to a value that is different from the exact result, which is also slightly different from another exact result obtained by Seung and Nelson [124] (see the discussion in conclusions and Appendix), namely

$$\begin{aligned} \frac{F}{Y\,\text{Area}} = \frac{1}{288} &= 0.0035 \text{ (EF, LF, IF)} \\ &= 0.0041 \text{ (Exact)} \\ &= 0.0040 \text{ (Exact SN) .} \end{aligned} \tag{5.81}$$

The (small) disagreement between EF, LF and IF with the exact result is a consequence of large displacements near the core of a disclination on a flat topography [144]. The small disagreement with SN results also reflects the intrinsic ambiguity of what is meant by an "exact" elastic theory, as terms with higher powers of the strain tensor, for example, maybe

included in the definition of the elastic energy Eq. 5.15, a point which we will elaborate in the conclusions.

For the case of a central disclination, at finite and increasing values of the aperture angle θ_m, the different linear approximations gradually converge to the exact result. Note that the free energy goes through a minimum at around $\theta_m \approx 1.05$, which maybe interpreted as the point where the disclination optimally screens the Gaussian curvature. It seems reasonable that this point maybe calculated when the PCC Eq. 5.13 is satisfied on average, namely

$$\int d^2\mathbf{x} s(\mathbf{x}) = \int d^2\mathbf{x} K(\mathbf{x}) \to \frac{\pi}{3} = 2\pi(1 - \cos(\theta_c)) \ , \tag{5.82}$$

that is, at $\theta_M = \theta_c = \arccos(5/6) = 0.59$, which is significantly lower and reflects the role of the boundary conditions. It is also important to note that when $\theta_M > \theta_c$, the approximation to the energy for the disclination free monolayer starts to deviate from the exact result.

5.6 Conclusions

In this chapter we have presented a general fully covariant elastic theory, as defined by the energy Eqs. 5.15 and 5.17, anticipated in Refs. [136,137]. We discussed three different linear approximations (EF, LF, IF) from which all analytical results quoted in the literature have been derived. Quite unexpectedly, the differences are quantitatively very small, but the ones in target space (LF, IF) have the advantage that satisfy topological relations, see Eq. 5.7, exactly. It is possible to compute orders beyond linear and, in this way, obtain the exact result, although for general problems, this is rather cumbersome.

The actual meaning of the "exact solution", however, appears as an ambiguous

concept. While our exact result of a single disclination on a flat monolayer as $\theta_m \to 0$ is almost the same as the value (see Eq. 5.81) obtained by Seung and Nelson [124], it is not obvious that the energies obtained by the two methods match for all values of θ_m. The Seung and Nelson's energy is given as

$$F_D = \frac{\epsilon}{2} \sum_{\langle i,j \rangle} \left(d_{ij} - \bar{d}_{ij} \right)^2 = \frac{\epsilon}{2} \sum_{\langle i,j \rangle} \left(|\vec{r}_i - \vec{r}_j| - a \right)^2 \tag{5.83}$$

where $\langle i, j \rangle$ are the nearest neighbors defined by a triangulation $\mathcal{T}$. This energy is conceptually the same as the one defined by Eqs. 5.15 and 5.17, since $\bar{d}_{ij} = a$ is the distance in reference and d_{ij} in target space, and, expanding in small displacements, both energies coincide for the choices of elastic constants $Y = 2\epsilon/\sqrt{3}$ and $\nu_p = 1/3$ [124]. However, these two approaches differ beyond linear order. It is possible to make them agree at higher orders by adding higher powers of $|d_{ij} - \bar{d}_{ij}|$ in Eq. 5.83 ,

$$F = F_D + \sum_{l=2}^{M} \frac{\epsilon_l}{2} \left(d_{ij} - \bar{d}_{ij} \right)^{2l} \tag{5.84}$$

so that, for appropriately chosen values ϵ_l, higher orders of the displacement beyond linear will agree with the energy Eq. 5.17. Additional powers of $u_{\alpha\beta}$ can also be added to Eq. 5.17, to make it agree with Eq. 5.83. Either case, it serves to make the point that Eqs. 5.17 and 5.83 represent two different non-linear elastic theories, and therefore, it is expected that the exact results for a single disclination will differ. It should be noted, however, that both exact results are close, thus highlighting that non-linear corrections are small. The natural question becomes then, which one is the "correct" model. A satisfactory answer can be given if the underlying microscopic potential among particles is known. Then it is possible to impose that the higher orders of elasticity theory (see Eq. 5.84) match the same orders

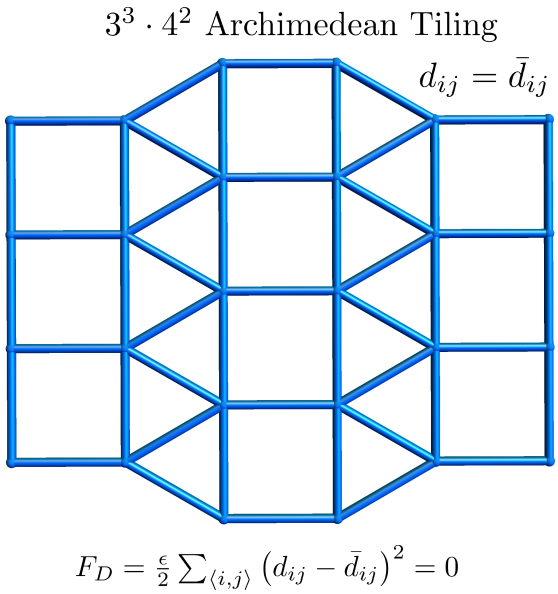

Figure 5.6: Example of the $(3^3.4^2)$ Archimedean tiling with zero elastic energy. Such configuration, however, has zero energy modes and require additional constraints to be stable.

of the energy of the crystal in powers of the displacement, as discussed in Ref. [133], where exceedingly accurate predictions for energies were obtained for any geometry.

Another fundamental aspect of the geometric theory of elasticity discussed in this chapter is the choice of the reference metric, which corresponds to a configuration where all nearest neighbors distances and angles are the same. In some cases, such as for a defect free disk or a cone with a single disclination, it is possible to optimize the geometry resulting into strain and stress free configurations in target space. For other, more complex defect distributions, such target space configurations do not exist. A conspicuous property of the model in Eq. 5.83, however, is that it involves nearest neighbor distances only, and the condition that the angles are the same does not need to be satisfied. Thus, general Archimedean tilings configurations, such as the one shown in Fig. 5.6, are strain/stress free for a target space consisting of a plane. It is interesting to note that it is possible to build

dodecagonal quasicrystals out of $(3^3.4^2)$ Archimedean tiling, which have been observed in nanocrystal systems [145]. Within elasticity theory, those Archimedean tilings require a Poisson ratio $\nu_p = 1/3$, as clear from the discussion following Eq. 5.83, see also Ref. [144].

We have shown that the "exact" equations of elasticity theory amount to minimizing the difference between the target and the reference metric

$$g(\text{Target metric}) - \bar{g}(\text{Reference metric}) \quad = \quad 2u_{\alpha\beta}$$

where the target metric is fixed by the topography (the surface), see Fig. 5.1, and the reference metric is such that its curvature $\bar{K}$ is a sum of disclinations and dislocations

$$\begin{aligned} \bar{K} &= \text{Disclinations} + \text{Dislocations} \\ &= \text{"Quanta" of Curvature} + \text{"Quanta" of Torsion} , \end{aligned}$$

where the disclinations are quantized in units of $\frac{\pi}{3}$ and the dislocations in units of the Burgers vector $\vec{b}$. These equations summarize the geometric content of the equations in elasticity theory as applied to arbitrary topographies. For boundary free crystals, they also satisfy topological constraints, for example, Eq. 5.7.

There are a number of issues that we have not discussed. For example, the free energy Eq. 5.17 is invariant under general parameterizations, which in turns, through the Noether theorem, gives rise to conservation laws that relate to the stress tensor. Also, the IF includes a term, see Eq. 5.41, that has derivative of the Gaussian curvature. In those cases where the Gaussian curvature is not constant and varies rapidly, this term may become important or even dominant.

In summary, we presented a covariant formulation of elasticity that unifies geometric and topological concepts with the theory of defects. All available results in the literature

maybe recovered from this formulation as suitable approximations, thus providing a rigorous justification on their validity, and providing the necessary framework for our recent studies of icosahedral order in virus shells [139]. Throughout this chapter, the geometry has been fixed. There are obviously many fascinating problems when the geometry is allowed to fluctuate, see, for example Ref. [146], but those problems will be discussed elsewhere.

Chapter 6

Elasticity in large icosahedral viruses: The interplay of Gaussian curvature and disclination interactions.

6.1 Introduction

More than fifty years ago, Caspar and Klug [147] made the striking observation that the capsids of most spherical viruses display icosahedral order(IO), defined by twelve five coordinated units (disclinations or pentamers) occupying the vertices of an icosahedron surrounded by hexameric units, see Fig. 6.1. While many studies have shown that this universal IO is favored under mechanical equilibrium [73–75], the mechanism by which these

shells grow, circumventing many possible activation barriers, and leading to the perfect IO remains mainly unknown.

Under many circumstances, small icosahedral capsids assemble spontaneously around their genetic material, often a single-stranded viral RNA [16, 21, 24, 32, 47]. Yet, larger double-stranded (ds) RNA or DNA viruses require what we generically denote as the template: scaffolding proteins (SPs) or an inner core [38–40, 42, 148, 149]. The focus of this paper is on these large viruses that require a template for successful assembly.

The major difficulty in understanding the pathway towards IO is apparent from the results of the generalized Thomson problem, consisting of finding the minimum configuration for interacting M-point particles constrained to be on the surface of a sphere. Simulation studies show that the number of metastable states increase exponentially with M [150], and only with the help of sophisticated optimization algorithms at relatively small values of M [15, 16, 23, 151], it is possible to obtain IO ground states. These situations, typical of spherical crystals, become even more difficult when considering the assembly of large capsids, in which once protein subunits are attached and a few bonds are made, it becomes energetically impossible for them to re-arrange: Should a single pentamer appear in an incorrect location, IO assembly would fail.

The combined effect of irreversibility and the inherent exponentially large number of metastable states typical of curved crystals puts many drastic constraints on IO growth. The complexity of the problem may be visualized by the various viral shells illustrated in Fig. 6.1, characterized by a structural index, the T number [76, 147, 152] $T = h^2 + k^2 + hk$, with h and k arbitrary integers, such that the crystal includes $60T$ monomers or $10(T-1)$

hexamers and 12 pentamers (disclinations).

A possible mechanism to successfully self-assemble a desirable structure might consist of protein subunits with chemical specificity, very much like in DNA origami [153] where structures with complex symmetries are routinely assembled. In viruses, however, capsids are built either from one or a few different types of proteins, so specificity cannot be the driving mechanism leading to IO [15, 47, 76, 154, 155]. In this paper, we show that a "generic" template provides a robust path to self- assembly of large shells with IO. This is consistent with many experimental data in that regardless of amino acid sequences and folding structures of virus coat and/or scaffolding proteins, due to the "universal" topological and geometrical constraints, large spherical viruses need scaffolding proteins to adopt IO, see Fig. 6.1. Although the focus of the paper is on virus assembly, the implication of our study goes far beyond and extend to many other problems where curved crystals are involved, a point that we we further elaborate in the conclusion [115, 156].

The distinct feature of spherical crystals is that their global structure is constrained by topology. More concretely, if $s(\mathbf{x})$ is the disclination density, then

$$\int d^2\mathbf{x}\ s(\mathbf{x}) = 2\pi\chi\ , \tag{6.1}$$

where χ is the Euler characteristic ($\chi = 2$ for a sphere). However a capsid closes only at the end of the assembly, and thus, Eq. 6.1 does not really restrict the number of disclinations during the growth process, as pentamers or other disclinations may be created or destroyed at the boundaries. For a complete shell, the easiest way to fulfill Eq. 6.1 is with twelve $q = +\frac{\pi}{3}$ disclinations, and this is the case we will follow hereon.

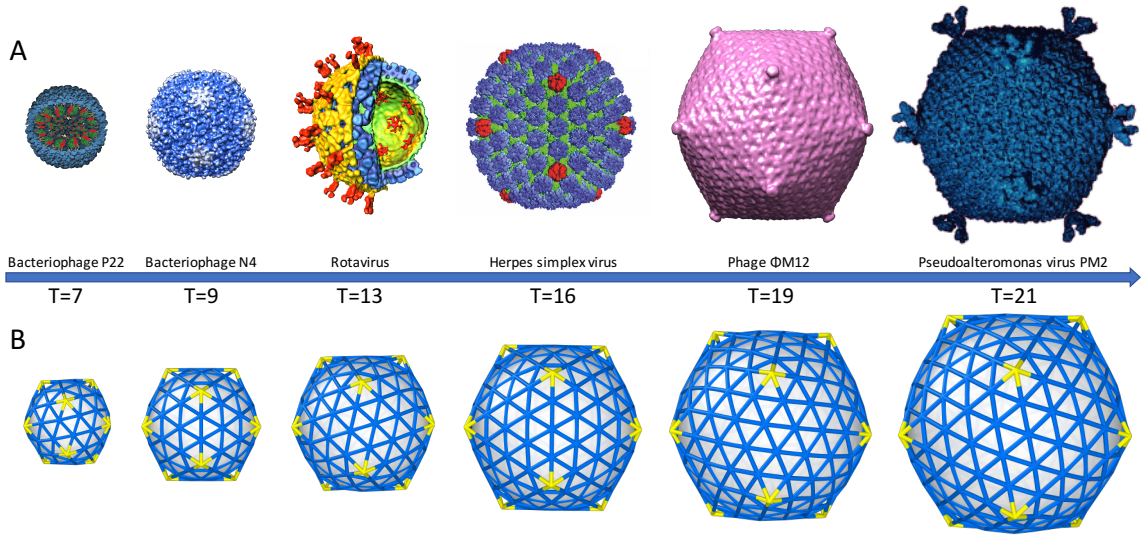

Figure 6.1: Figure 1a. From left to right: Bacteriophage P22 [7], Bacteriophage N4 [8], Rotavirus [9], Herpes simplex virus [10], Phage ΦM12 [11] and Pseudoalteromonas virus [12]. The triangulation number of each virus is shown below it. The scaffolding proteins and hydrogenases inside the capsid of Bacteriophage P22 and the inner shell of Rotavirus are illustrated in the figure. To form structures with IO, all viruses in the figure need scaffolding proteins as illustrated for Bacteriophage P22. Only Rotavirus requires a preformed scaffolding layer. Rotavirus belong to Reoviridae virus family, they all form $T = 13$ and have multi-shell structures. Figure 1b. Capsids obtained in the simulations from left to right: $T = 7$, $T = 9$, $T = 13$, $T = 16$, $T = 19$ and $T = 21$.

A minimal model for spherical crystals consists of a free energy

$$\begin{aligned} F_c &= \int d^2\mathbf{x}\left[\mu u_{\alpha\beta}^2 + \frac{\lambda}{2}(u_{\alpha\alpha})^2\right] + \frac{\kappa}{2}\int d^2\mathbf{x}(H(\mathbf{x}) - H_0)^2 \\ &\equiv F_c^l + F_c^b \end{aligned} \tag{6.2}$$

where $u_{\alpha\beta}$ is the strain tensor. The coefficients μ, λ are the Lame coefficients, which depend on the microscopic underlying interactions. Here $H(\mathbf{x})$ is the extrinsic curvature of the template, H_0 the spontaneous curvature and κ the bending rigidity. By integrating the phonon degrees of freedom, we can recast the term F_c^l in Eq. 6.2 as a non-local theory of interacting disclinations, with free energy [131]

$$F_c^l = \frac{K_0}{2}\int d^2\mathbf{x}d^2\mathbf{y}\left[(K(\mathbf{x}) - s(\mathbf{x}))G(\mathbf{x},\mathbf{y})(K(\mathbf{y}) - s(\mathbf{y}))\right] , \tag{6.3}$$

where $K(\mathbf{x})$ is the Gaussian curvature and K_0 is the Young modulus. The disclination density $s(\mathbf{x}) = \sum_{i=1}^{12} q_i\delta(\mathbf{x} - \mathbf{x}_i)$ has as variables the positions of 12 disclinations, each of charge $q_i = \frac{\pi}{3}$. The function $G(\mathbf{x},\mathbf{y})$ is the inverse of the Laplacian square [131]. All previous studies for the model in Eq. 6.3 have been done for curved crystals without a boundary. In this paper, we provide, for the first time, the necessary formalism to include the presence of a boundary.

A discrete version of Eq. 6.2 is given by [115, 124, 131, 156]

$$F_d = E_s + E_b = \sum_i \frac{1}{2}k_s(b_i - b_0)^2 + \sum_{i,j} k_b[1 - \cos(\theta_{ij} - \theta_0)] \tag{6.4}$$

with θ_0 a preferred angle, related to the spontaneous curvature H_0. The stretching energy sums over all bonds i with b_0 the equilibrium bond length and the bending energy is between all neighboring trimers indexed with ij. We further assume that there is an attractive force between the trimers and the preformed scaffolding layer (inner core) (see Fig.6.4), which,

consistent with our minimal model, involves a simple LJ-potential $E_{LJ} = \sum_i 4\epsilon[(\frac{\sigma}{r_i})^{12} - 2(\frac{\sigma}{r_i})^6]$ with ϵ the depth of the potential and σ the position of minimum energy corresponding to optimal distance between the center of the core and subunits. In the next section, we associate a dynamics to these models, which corresponds to following a local minimum energy pathway.

6.2 Methods

6.2.1 Discrete model

The growth of the shells is based on the following assumptions [23, 32, 47, 154]: At each step of growth, a new trimer is added to the location in the boundary which makes the maximum number of bonds with the neighboring subunits. This is consistent with the fact that protein-protein attractive interaction is weak and a subunit can associate and dissociate till it sits in a position that forms a few bounds with neighboring proteins. These interactions eventually become strong for the subunits to dissociate and trimer attachment becomes irreversible [16]. The attractive interactions between subunits, whose strength depends on electrostatic and hydrophobic forces, are implicit in the model. Note that pH and salt can modify the strength of protein-protein and protein-template interactions and thus the growth pathway. The impact of pH and salt on the shell assembly will be pursed elsewhere.

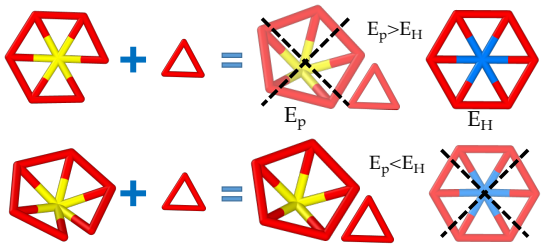

Figure 6.2: Dynamics of formation of a hexamer vs. a pentamer: five trimers are attached at a vertex with an opening angle close to $\pi/3$ at the top and much smaller than $\pi/3$ at the bottom. If the energy per subunit of formation of a pentamer E_p is higher than a hexamer E_H, then a hexamer forms (top); otherwise, a pentamer assembles (bottom).

A crucial step in the assembly process is the formation of pentamers, which occurs only if the local energy is lowered, as illustrated in Fig. 6.2. After the addition of each subunit or the formation of a pentamer, using HOOMD package [157, 158], we allow the triangular lattice to relax and to find its minimum energy configuration [44].

The proposed mechanism follows a sequential pathway where trimers (T) attach to the growing capsid ($C \to C'$) according to the reaction

$$\begin{aligned} T + C &\leftrightarrows TC \\ TC &\to C' \end{aligned} \tag{6.5}$$

with characteristic rates k_D, k'_D and k_r. The rate $k_D = 2\pi D_T R_T$ is diffusion limited, with R_T the trimer radius and D_T its diffusion coefficient, so that the reaction speed is linear in trimer concentration $v_{TC} = k_D[T]$, k'_D is the detachment rate as the trimer searches for the local minimum, and k_r is the irreversible rate of attachment of the trimer to the capsid. The combined reaction rate is therefore $k_T = \frac{k_r k_D}{k'_D + k_r}$. Once the second reaction in Eq. 6.5 takes place, there is no possibility for correcting mistakes: if a pentamer forms in the incorrect location, IO is frustrated. With some additional assumptions about the dependence of k_r

on the coordination of the growing capsid, it is possible to derive overall rates for capsid formation, a problem that will be pursued elsewhere.

Two important parameters arises in discussing spherical crystals with the model Eq. 6.4. One is the Foppl von-Karman (FvK) number [115]

$$\gamma = \frac{b_0^2 k_s}{k_b} \ , \tag{6.6}$$

which measures the ratio of stretching to bending moduli. When the FvK number is large, the protein subunits optimize stretching and bend away from their preferred radius of curvature showing some degree of faceting, which is the case of large viruses, see Figure 6.1. For the case of template driven self-assembly, we introduce a new parameter

$$\eta = \frac{k_b}{\epsilon}, \tag{6.7}$$

which measures the relative strength of the bending rigidity to the attraction of the trimers to the template. For small η, the proteins follow the core curvature during growth at all the time, regardless of proteins spontaneous curvature. For large η, the shell detaches from the core and follow its preferred curvature. In this paper we will be mostly interested in the regime $\eta \approx \mathcal{O}(1)$ and $\gamma \gg 1$, where the template, rather than the spontaneous curvature dictates the size of the capsid.

6.2.2 Continuum model

We now consider the model given in Eq. 6.3 on a spherical cap with an aperture angle θ_m, so that its geodesic radius is $R_m = \theta_m R$, see Fig. 6.4b. The Lame term (F_c^l) in

Eq. 6.3 can then be written as

$$F_c^l = \frac{1}{2K_0}\int d^2\mathbf{x}\sqrt{g}\,(\Delta\chi)^2 \ , \tag{6.8}$$

where $g_{\mu\nu}$ is the metric defining the surface and the Laplacian is $\Delta = \frac{1}{\sqrt{g}}\partial_\mu(g^{\mu\nu}\partial_\nu)$, with χ the Airy Stress function that satisfies

$$\frac{1}{K_0}\Delta^2\chi(\mathbf{x}) \quad = \quad s(\mathbf{x}) - K(\mathbf{x}). \tag{6.9}$$

In SI Appendix, we provide the detailed calculations. We note that approximate solutions of Eq. C.2 are available under the assumption that the Laplacian is computed with a flat metric, see Ref [128], which immediately leads to $\int d^2\mathbf{x}K(\mathbf{x}) = \int \frac{d^2\mathbf{x}}{R^2} = \frac{A}{R^2} = \pi \neq 2\chi\pi = 4\pi$, directly violating the topological constraint Eq. 6.1. Therefore previous results [130] are limited to small curvatures or aperture angles ($\theta_m \ll \pi$). The generalization of Eq. 6.3 to include boundaries proceeds by defining the stress tensor by the expression $\sigma^{\alpha\beta} = g^{\alpha\beta}\Delta\chi(\mathbf{x}) - g^{\alpha\mu}g^{\beta\nu}\nabla_\mu\nabla_\nu\chi(\mathbf{x})$. We now include a stress free condition $\sigma_{\alpha\beta}n^\beta = 0$ at the boundary, where n^α is the normal to the boundary. For a spherical cap, see Fig. 6.4b, we use the metric $ds^2 = g_{\mu\nu}dx^\mu dx^\nu = dr^2 + R^2\sin^2(r/R)d\phi^2$. Note that following the simulation outcomes, we ignore boundary fluctuations. This is mainly because of the strength of protein-protein interactions and line tension implicit in the growth model and is consistent with the simulation results.

With the above definitions, the topological constraint Eq. 6.1 is satisfied exactly for a sphere. The free energy Eq. 6.3 then becomes

$$F_c^l(\theta_m, \mathbf{x}_i) \quad = \quad E_0(\theta_m) + \sum_{i=1}^{N} E_{0d}(\mathbf{x}_i, \theta_m) + \sum_{i=1}^{N}\sum_{j=1}^{N} \hat{E}_{dd}(\mathbf{x}_i, \mathbf{x}_j, \theta_m) \tag{6.10}$$

with E_0 is the free energy of the hexamers, E_{0d} the interplay between Gaussian curvature and pentamers and $\hat{E}_{dd}$ describes disclination(pentamer) interactions. It is convenient to separate this last term as

$$F_c^{dd} = \sum_{i=1}^{N}\sum_{j=1}^{N}\hat{E}_{dd}(\mathbf{x}_i,\mathbf{x}_j,\theta_m) = \sum_{i=1}^{N}E_{self}(\mathbf{x}_i) + \sum_{i=1}^{N}\sum_{j>i}^{N}E_{dd}(\mathbf{x}_i,\mathbf{x}_j), \qquad (6.11)$$

where $E_{self}(\mathbf{x}_i)$ is the disclination self-energy, which depends on the location of a pentamer relative to the boundary.

6.3 Results

Consistent with the assumptions describing the dynamics of growth noted in previous section, we consider the spherical cap in Fig. 6.4b with an aperture angle, which monotonically varies from $\theta_m = 0$ to $\theta_m = \pi$ (sequential growth) as a function of time $\theta_m(t)$. Then, for each value of θ_m we calculate the free energy Eq. 6.10 and compare it to the one with an additional new defect (local condition). Once the latter one is favorable, the new defect is added.

For small values of θ_m, the cap grows defect free. In Fig. 6.3 we plot the energy of a spherical cap for $\theta_m = 0.7$. The dotted line in the figure shows the disclination self-energy E_{self}, the dashed line the Gaussian curvature-disclination interactions E_{0d} and the solid line is the sum of both energies as a function of the location of disclination in the cap. The diamond in the figure corresponds to the minimum of energy and indicates the location of the first (and only) disclination appearing in the cap, around $r \sim 0.66R$. This value is very close to the geodesic distance following from the local "screening" of the Gaussian

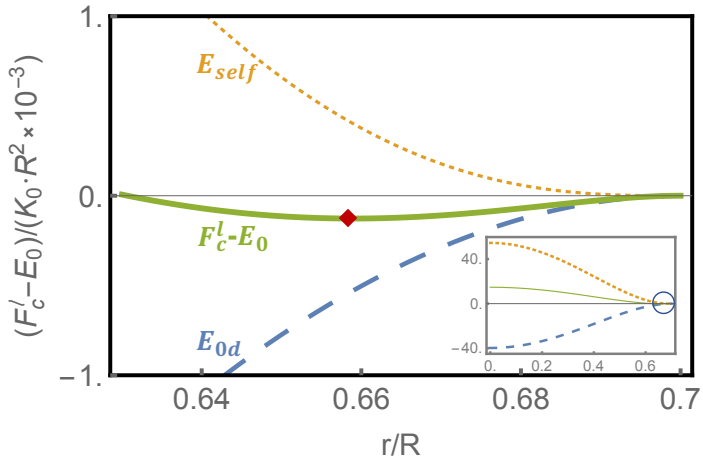

Figure 6.3: The 1D energy plot for the first disclination: The dotted line corresponds to disclination self-energy E_{self} (Eq. 6.11), the dashed line to the Gaussian curvature-disclination interactions E_{0d} and the solid line is the result of the addition of both energies $F_c^l - E_0$ (Eq. 6.10) as a function of the location of disclination in the shell for $\theta_m = 0.7$. The energy goes through a minimum for $r = 0.66R$. The inset graph shows the zoom-out energy plot where the circle region corresponds to the main graph.

curvature $\int d^2s(\mathbf{x}) = \int d^2K(\mathbf{x}) \rightarrow \frac{\pi}{3} = 2\pi(1 - \cos(\theta_m))$ such that $r = \arccos(5/6)R = 0.59R$. Somewhat counter intuitively, the first disclination does not appear at the center of the cap, which is the result of the competition between the disclination self-energy whose minimum is at the boundary and the Gaussian curvature-disclination interaction E_{0d} with its minimum energy occurring at the cap center, see Fig. S2 in SI Appendix where the contourplots of the different elastic free energies as a function of the location of the first disclination, r are shown. As the shell grows, the appearance of a new disclination becomes energetically favorable, *i.e.* a new energy valley for the formation of a new disclination emerges, as illustrated in Fig. 6.4b, where we show the contour plots of total elastic energies for spherical caps with $\theta_m = 0.8$ through $\theta_m = \pi$. The bigger ball in each plot indicates the position of the latest energy well, which is where the addition of the next disclination takes place. Remarkably, both in the continuum model and simulations, during the growth process, the disclinations always appear in the positions that eventually become the vertices

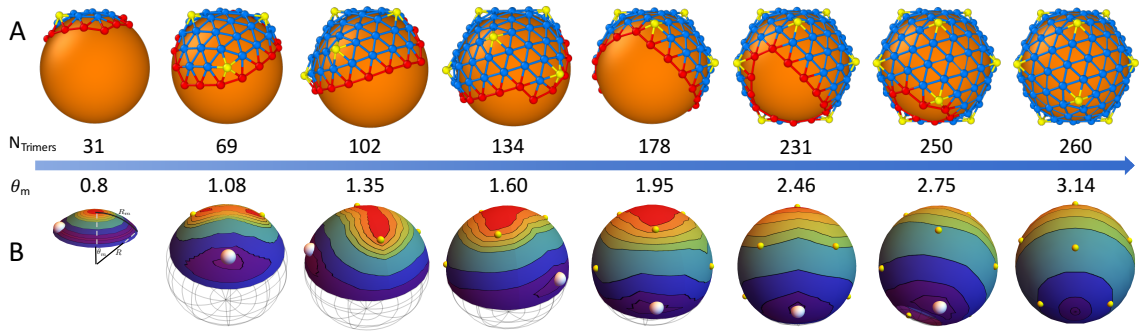

Figure 6.4: The snapshots of a T=13 growth in discrete simulation (first row) and continuum theory (second row). The upper caps correspond to the simulation growth with triangles representing the trimers. The yellow vertices belong to pentamers, blue ones to hexamers and red ones to the cap edge. The gold core mimics the preformed scaffolding layer or inner core. The lower caps denote the energy contourplots for the newest disclinations that appear in the purple energy well, with geodesic shell size $R_m = R\theta_m$. The red region has the highest energy and purple the lowest one. There is a yellow ball in the position of each disclination. The largest ball corresponds to a newly formed disclination.

of an icosahedron.

Results with the discrete model Eq. 6.4 are shown in Fig. 6.4a. Here again, the disclinations universally appear at the vertices of an icosahedron, in complete agreement with the analytical calculation. The simulations were performed for all values between $T = 7$ and $T = 21$ and in all cases the IO was achieved without a single error. The size of the core in Fig. 6.4a is commensurate with $T = 13$ structures. We note that for these simulations the proteins spontaneous radius $1/H_0$ is much smaller than the core radius, R_c ($R_c H_0 \gg 1$), a point that is discussed in more detail further below. In SI Appendix we provide a movie illustrating the growth of a $T = 21$ structure, which includes 420 triangles.

6.3.1 The role of stretching and bending rigidity

Figure C.3 shows the stretching energy vs N (number of subunits assembled) as a $T = 13$ shell grows for six different values of FvK $\gamma > 1$. We note that for large spontaneous

radius of curvature and small γ when bending rigidity is dominant, no large icosahedral shell assembles successfully. Rather interestingly, there are conspicuous differences in the dynamics as a function of the FvK parameter γ.

For small values of $\gamma = 2$ (thick black line in Fig. C.3) the shell elastic energy grows almost linearly as a function of N but does not show IO. This takes place for higher γ-values. The arrows in Fig. C.3 indicate a drop in the elastic energy associated with the appearance of pentamers, see SI Appendix for more details. At the beginning of the growth, the shells with different values of γ might follow different pathways and thus, the number of hexamers vary before the first few pentamers form. However, as the shell grows, the pentamers appear precisely at the same place, independently of γ. Note that the bending energy of the shells always grows linearly as a function of number of subunits for any γ (see SI Appendix).

6.4 Discussion

Our results show that for large shells ($T > 4$) successful assembly into IO requires a non-specific attractive interaction between protein subunits and a template. This interaction is implicit in the continuum model and is included as a generic attractive Lennard-Jones potential in the simulations. Furthermore, we find that the location of pentamers are completely controlled by the stretching energy as it is the case in the continuum elasticity theory.

In the absence of the template, small spherical crystals ($T = 1$ and $T = 3$) assemble spontaneously, for almost any FvK parameter γ. However, as we increase the spontaneous

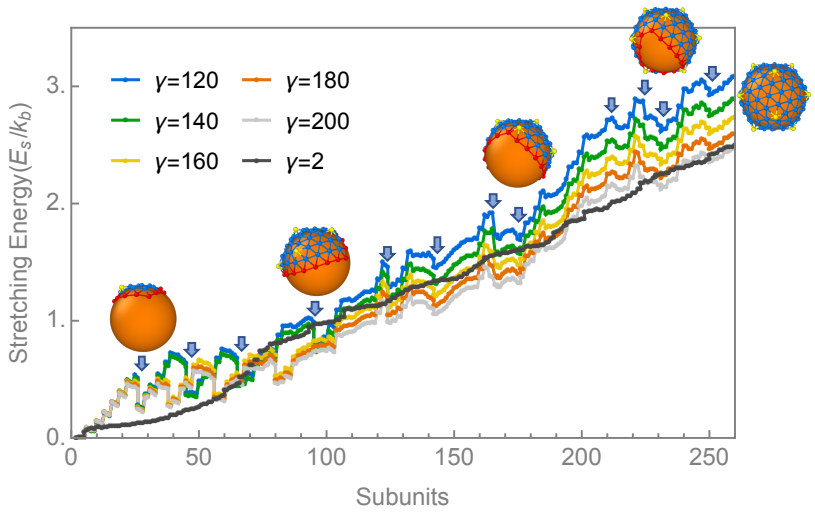

Figure 6.5: The stretching energy of a T=13 shell as a function of number of trimeric subunits. For small FvK numbers ($\gamma = 2$, black line), there is no significant drop in energy as a pentamer forms. However, for large FvK numbers ($\gamma \gg 1$), the formation of pentamers drastically lowers the energy of the elastic shell.

radius of curvature, the final structure depends on the value of γ. For small γ, large spherical shells without any specific symmetry form, and at large $\gamma > 5$ curved hexagonal sheets, which eventually assemble into tubular or conical structures are obtained. Thus our results predict that large shells with IO cannot grow without template.

A template can have a significant impact on the structure and symmetry of the shell. While a weak subunit-core attractive interaction has a minimal role in the shell shape, a very strong subunit-core interaction will override the mechanical properties of proteins. The subunits sit tightly on the template to form a sphere with no specific symmetry. We were able to observe large shells with IO only for $\eta \sim 1$ but at high γ. In this regime, in order for pentamers to overcome the core attraction and form in the "correct" position, they must assume a symmetric shape and buckle up (see Fig. 6.1b). Indeed a strong bending energy is needed to overcome the shell adsorption. We find that without decreasing γ (increasing k_b) but with increasing spontaneous curvature, the bending energy associated with the

deviation from the preferred curvature of subunits adsorbed to the core becomes strong enough to make the pentamers buckle and assume a smooth shape. Quite interestingly, we find that this is the strategy that the nature has taken to form large shells with IO.

The role of the inner core or the preformed scaffold layer presented above is very similar to the role of SPs, which assemble at the same time as the capsid proteins (CPs), *i.e.*, the template grows simultaneously with the capsid (see Fig. 6.6). In fact one can think of the inner core as a permanent "inner scaffold" [42]. For example, Bacteriophage P22 has a T=7 structure, but in the absence of scaffolding (Fig. 6.1, P22) often a smaller $T = 4$ forms. Similarly, Herpesvirus makes a $T = 16$ structure but without the SPs, a $T = 7$ assembles. More relevant to the present study is the case of Infectious Bursal Disease Virus (IBDV) a dsRNA virus that in the presence of SPs forms a $T = 13$ capsid but in the absence the subunits assemble to form a $T = 1$ capsid. This is exactly the condition for formation of the $T = 13$ structure in Fig. 6.4 where the preferred curvature between subunits is such that in the absence of scaffold they form a $T = 1$ structure. Reoviridae virus family also form $T = 13$ but they have multi-shell structures, which act as inner cores. For instance, in this family Bluetongue virus is a double capsid particle, outer (necessary for infection) and inner capsid (encloses RNA genome). The inner capsid, termed as "core" has two protein layers. The surface layer (or shell) is a $T = 13$ capsid that assembles around the inner shell, a $T = 2$ structure (an inner core). Interestingly, it has been suggested that there is an evolutionary connection between SPs of IBDV and inner capsid of Bluetongue virus [42].

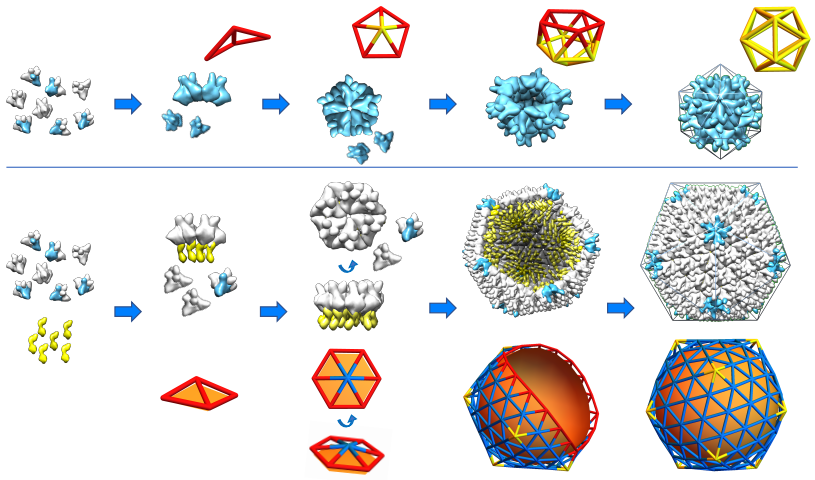

Figure 6.6: The role of scaffolding proteins (SPs) in the formation of $T = 13$ capsid of IBDV. Without SPs, the CPs (blue and white subunits) of IBDV form $T = 1$ structure (upper figure). In the presence of SPs (yellow subunits), they form $T = 13$ structure (lower figure). The results of our simulations are also illustrated next to each intermediate step. Note that SPs (yellow subunits) do not assemble without the CPs but probably experience some conformational changes during the assembly. However, our focus here is solely on the impact of scaffolding on the CPs resulting in a change in the capsid T number. For preformed SPs, like in the case of bluetongue virus, the core is spherical and there is no indication of any changes on the size of spherical template during the assembly.

6.5 Conclusions

Our model establishes that successful self-assembly of components into a spherical capsid with IO requires a template that determines the radius of the final structure. This template is very non-specific, and in its absence, protein subunits assemble into either smaller capsids or structures without IO.

Even though the focus of the above study was on the impact of the preformed scaffolding layer, based on the experimental observations we conclude that the SPs, which assemble simultaneously with CPs (Fig. 6.6), play basically the same role as the inner core in the assembly of large icosahedral shells. Figure 6.6 shows that in the absence of SPs, CPs of IBDV form a $T = 1$ structure but when the same IBDV proteins co-assemble with SPs

(yellow units) a $T = 13$ forms. The figure also shows the pathway of formation of $T = 1$ and $T = 13$ structures obtained in our simulations. We emphasize that the mechanical properties of subunits are the same for both shells, the difference in structures arises from the substrate or SPs.

The contribution of the SPs is twofold. The CPs of many viruses including bluetongue virus noted above do not assemble in the absence of SPs. On the one hand, it appears that SPs lower the energy barrier and help capsid subunits to aggregate. On the other hand, by forcing the CPs to assemble into a structure larger than their spontaneous radius of curvature, they contribute to preserving IO.

Examples of the role of templates on the formation of spherical crystals are not limited to viruses, but include crystallization of metals on nanoparticles [159], solid domains on vesicles [160, 161], filament bundles [128] and colloidal assemblies at water-oil interfaces [112]. Nevertheless, it has been shown [162] that sufficiently rigid crystals grow as almost flat sheets free of defects, unable to assemble with IO. This regime, however, seems not to be accessible to viral capsids, as the hydrophobic interaction between monomers force close-packing structures that are incompatible with grain boundaries.

This study shed light at fundamental scale on the role of mechanical properties of building blocks and scaffolding proteins. The proposed mechanism is consistent with available experiments on viruses involving either scaffolding proteins or inner capsids. Further experiments will be necessary to validate many predictions of our described mechanism.

Part IV

Conclusion

Chapter 7

Conclusion

Viruses self-assemble to form spherical capsids with icosahedral orders. The mechanisms are quite different depending on the size of viruses.

Two models are presented for small viruses: (1) nucleation and growth, or (2) en-mass assembly. Our studies show that the first model is appropriate for empty capsids, while the second mechanism can explain better the assembly in the presence of genome molecules. To find the assembly pathways, considerable efforts have been made in experimental work, molecular dynamics simulations as well as many theoretical works such as classical nucleation theory, line assembly model and thermodynamics. However, the significant number of parameters, such as pH, salt concentration, protein concentration, genome structure, packaging signal make the study of the assembly pathway extremely hard and the future research is still very much needed.

Compared to the small viruses, large viruses are even a bigger mystery. The en-mass pathway is ruled out because of the significant amount of protein subunits should

assemble and as such the disassembly becomes almost impossible. Quite remarkably, the thesis shows that a perfect shell with IO can be formed through nucleation and growth. We prove that a nonspecific template is required for an error-free pathway. As the spherical cap grows, the nonlinear geometry imposed by the template gives rise to a deep potential well, which attracts the new pentamer to be located at the vertex of an icosahedron.

The thesis has successfully investigated the virus assembly of different families through theoretical and simulation work. However, many exceptions still exist. For example, trimer subunits are limited to a certain group of viruses, the proposed mechanism in the thesis may not be suitable for viruses composed of only pentamers, such as simian vacuolating virus 40. In addition, presuming a perfect curvature seems a hard task for scaffolding proteins, and fluctuations are well expected to be a reasonable cause of non-icosahedral shells. Thus, many other auxiliary mechanisms incorporating the specific interaction of proteins and packaging signal of scaffolding proteins for instance, are to be pursued in the future. Nevertheless, the thesis sheds light on the mechanism of assembly of both small and large viruses, and provides many predictions for future experiments. Further applications will be expected in various areas of nanotechnology, gene delivery and medicine.

Bibliography

[1] Heinz Fraenkel-Conrat and Robley C Williams. Reconstitution of active tobacco mosaic virus from its inactive protein and nucleic acid components. *Proceedings of the National Academy of Sciences of the United States of America*, 41(10):690, 1955.

[2] JB Bancroft, GJ Hills, and Rou Markham. A study of the self-assembly process in a small spherical virus formation of organized structures from protein subunits in vitro. *Virology*, 31(2):354–379, 1967.

[3] Barbie K Ganser, Su Li, Victor Y Klishko, John T Finch, and Wesley I Sundquist. Assembly and analysis of conical models for the hiv-1 core. *Science*, 283(5398):80–83, 1999.

[4] Chunyan Wang, Jiagang Tu, Jun Liu, and Ian J Molineux. Structural dynamics of bacteriophage p22 infection initiation revealed by cryo-electron tomography. *Nature microbiology*, page 1, 2019.

[5] T. S. Baker, N. H. Olson, and S. D. Fuller. Adding the third dimension to virus life cycles: Three-dimensional reconstruction of icosahedral viruses from cryo-electron micrographs. *Microbiology and Molecular Biology Reviews*, 63(4):862–922, 1999.

[6] I. L. Hofacker, W. Fontana, P. F. Stadler, L. S. Bonhoeffer, M. Tacker, and P. Schuster. Fast Folding and Comparison of RNA Secondary Structures. *Monatsh. Chem.*, 125:167, 1994.

[7] Paul C Jordan, Dustin P Patterson, Kendall N Saboda, Ethan J Edwards, Heini M Miettinen, Gautam Basu, Megan C Thielges, and Trevor Douglas. Self-assembling biomolecular catalysts for hydrogen production. *Nature chemistry*, 8(2):179, 2016.

[8] Kyung H Choi, Jennifer McPartland, Irene Kaganman, Valorie D Bowman, Lucia B Rothman-Denes, and Michael G Rossmann. Insight into dna and protein transport in double-stranded dna viruses: the structure of bacteriophage n4. *Journal of molecular biology*, 378(3):726–736, 2008.

[9] Joseph B. Pesavento, Mary K. Estes, and B.V.Venkataram Prasad. Ii, 1. structural organization of the genome in rotavirus. In *Viral Gastroenteritis*, volume 9 of *Perspectives in Medical Virology*, pages 115–127. Elsevier, 2003.

[10] Z Hong Zhou, Matthew Dougherty, Joanita Jakana, Jing He, Frazer J Rixon, and Wah Chiu. Seeing the herpesvirus capsid at 8.5 å. *Science*, 288(5467):877–880, 2000.

[11] M Elizabeth Stroupe, Tess E Brewer, Duncan R Sousa, and Kathryn M Jones. The structure of sinorhizobium meliloti phage ϕm12, which has a novel t= 19l triangulation number and is the founder of a new group of t4-superfamily phages. *Virology*, 450:205–212, 2014.

[12] Hanna M Oksanen et al. Ictv virus taxonomy profile: Corticoviridae. *Journal of General Virology*, 98(5):888–889, 2017.

[13] Michael Francis Hagan, Robijn Bruinsma, Sanjay Dharmavaram, Selene Baochen She, and Guillermo Lázaro. Gaussian curvature and the budding kinetics of enveloped viruses. *BioRxiv*, page 457135, 2018.

[14] Cheng Zeng, Mercedes Hernando-Pérez, Bogdan Dragnea, Xiang Ma, Paul Van Der Schoot, and Roya Zandi. Contact mechanics of a small icosahedral virus. *Physical review letters*, 119(3):038102, 2017.

[15] Roya Zandi, David Reguera, Robijn F Bruinsma, William M Gelbart, and Joseph Rudnick. Origin of icosahedral symmetry in viruses. *Proceedings of the National Academy of Sciences*, 101(44):15556–15560, 2004.

[16] J. D. Perlmutter, C. Qiao, and M. F. Hagan. Viral genome structures are optimal for capsid assembly. *eLife*, 2:e00632, 2013.

[17] Gonca Erdemci-Tandogan, Jef Wagner, Paul van der Schoot, Rudolf Podgornik, and Roya Zandi. Rna topology remolds electrostatic stabilization of viruses. *Phys. Rev. E*, 89:032707, Mar 2014.

[18] A. Siber and R. Podgornik. Nonspecific interactions in spontaneous assembly of empty versus functional single-stranded RNA viruses. *Phys. Rev. E*, 78:051915, 2008.

[19] Antoni Luque, David Reguera, Alexander Morozov, Joseph Rudnick, and Robijn Bruinsma. Physics of shell assembly: Line tension, hole implosion, and closure catastrophe. *The Journal of chemical physics*, 136(18):184507, 2012.

[20] Adam Zlotnick. Distinguishing reversible from irreversible virus capsid assembly. *Journal of molecular biology*, 366(1):14–18, 2007.

[21] Jingchuan Sun, Chris DuFort, Marie-Christine Daniel, Ayaluru Murali, Chao Chen, Kodetham Gopinath, Barry Stein, Mrinmoy De, Vincent M. Rotello, Andreas Holzenburg, C. Cheng Kao, and Bogdan Dragnea. Core-controlled polymorphism in virus-like particles. *Proc. Nat. Acad. Sci. USA*, 104(4):1354–1359, 2007.

[22] R. Kusters, H.-K Lin, R. Zandi, I. Tsvetkova, B. Dragnea, and P. van der Schoot. Role of charge regulation and size polydispersity in nanoparticle encapsulation by viral coat proteins. *J. Phys. Chem. B*, 119:1869–1880, 2015.

[23] M. F. Hagan and R. Zandi. Recent advances in coarse-grained modeling of virus assembly. *Curr. Opin. Virol.*, 18:36–43, 2016.

[24] F. D. Sikkema, M. Comellas-Aragones, R. G. Fokkink, B. J. M. Verduin, J.J.L.M. Cornelissen, and R. J. M. Nolte. Monodisperse polymer-virus hybrid nanoparticles. *Org. Biomol. Chem.*, 5:54, 2007.

[25] Y. P. Ren, S. M. Wong, and L. Y. Lim. In vitro-reassembled plant virus-like particles for loading of polyacids. *J. Gen. Virol.*, 87:2749, 2006.

[26] P. Ni, Z. Wang, X. Ma, N. C. Das, P. Sokol, W. Chiu, B. Dragnea, M. Hagan, and C. C. Kao. An Examination of the Electrostatic Interactions between the N-Terminal Tail of the Brome Mosaic Virus Coat Protein and Encapsidated RNAs. *J. Mol. Biol.*, 419:284, 2012.

[27] A Losdorfer Bozic, A Siber, and R Podgornik. Electrostatic theory of viral self-assembly. *J. Biol. Phys.*, 39:215, 2013.

[28] A. Zlotnick, R. Aldrich, J. M. Johnson, P. Ceres, and M. J. Young. Mechanism of Capsid Assembly for an Icosahedral Plant Virus. *Virology*, 277:450, 2000.

[29] H.-K. Lin, P. van der Schoot, and R. Zandi. Impact of Charge Variation on the Encapsulation of Nanoparticles by Virus Coat Proteins. *Phys. Biol.*, 9:066004, 2012.

[30] Venkatesh Sivanandam, Deborah Mathews, Rees Garmann, Gonca Erdemci-Tandogan, Roya Zandi, and A L N Rao. Functional analysis of the N-terminal basic motif of a eukaryotic satellite RNA virus capsid protein in replication and packaging. *Scientific Reports*, 6:26328, may 2016.

[31] Huand Tao, Zhangand Rui, and B. I. Shklovskii. Electrostatic theory of viral self-assembly. *Physica A*, 387:3059, 2008.

[32] M. Comas-Garcia, R. D. Cadena-Nava, A. L. N. Rao, C. M. Knobler, and W. M. Gelbart. In Vitro Quantification of the Relative Packaging Efficiencies of Single-Stranded RNA Molecules by Viral Capsid Protein. *J. Virol.*, 86:12271, 2012.

[33] Rees F Garmann, Mauricio Comas-Garcia, Charles M Knobler, and William M Gelbart. Physical principles in the self-assembly of a simple spherical virus. *Accounts of chemical research*, 49(1):48–55, 2015.

[34] Maelenn Chevreuil, Didier Law-Hine, Jingzhi Chen, Stéphane Bressanelli, Sophie Combet, Doru Constantin, Jéril Degrouard, Johannes Möller, Mehdi Zeghal, and Guillaume Tresset. Nonequilibrium self-assembly dynamics of icosahedral viral capsids packaging genome or polyelectrolyte. *Nature communications*, 9(1):3071, 2018.

[35] Alexander Borodavka, Roman Tuma, and Peter G Stockley. Evidence that viral rnas have evolved for efficient, two-stage packaging. *Proceedings of the National Academy of Sciences*, 109(39):15769–15774, 2012.

[36] Gonca Erdemci-Tandogan, Jef Wagner, Paul van der Schoot, Rudolf Podgornik, and Roya Zandi. Effects of rna branching on the electrostatic stabilization of viruses. *Phys. Rev. E*, 94:022408, 2016.

[37] Surendra W. Singaram, Rees F. Garmann, Charles M. Knobler, William M. Gelbart, and Avinoam Ben-Shaul. Role of rna branchedness in the competition for viral capsid proteins. *The Journal of Physical Chemistry B*, 119:13991, 2015.

[38] William Earnshaw and Jonathan King. Structure of phage p22 coat protein aggregates formed in the absence of the scaffolding protein. *Journal of molecular biology*, 126(4):721–747, 1978.

[39] Pamela A Thuman-Commike, Barrie Greene, Justine A Malinski, Jonathan King, and Wah Chiu. Role of the scaffolding protein in p22 procapsid size determination suggested by t= 4 and t= 7 procapsid structures. *Biophysical journal*, 74(1):559–568, 1998.

[40] Irene Saugar, Nerea Irigoyen, Daniel Luque, José L Carrascosa, José F Rodríguez, and José R Castón. Electrostatic interactions between capsid and scaffolding proteins mediate the structural polymorphism of a double-stranded rna virus. *Journal of Biological Chemistry*, 285(6):3643–3650, 2010.

[41] Jonathan M Grimes, J Nicholas Burroughs, Patrice Gouet, Jonathan M Diprose, Robyn Malby, Stephan Ziéntara, Peter PC Mertens, and David I Stuart. The atomic structure of the bluetongue virus core. *Nature*, 395(6701):470, 1998.

[42] Fasséli Coulibaly, Christophe Chevalier, Irina Gutsche, Joan Pous, Jorge Navaza, Stéphane Bressanelli, Bernard Delmas, and Félix A Rey. The birnavirus crystal structure reveals structural relationships among icosahedral viruses. *Cell*, 120(6):761–772, 2005.

[43] Sanaz Panahandeh, Siyu Li, and Roya Zandi. The equilibrium structure of self-assembled protein nano-cages. *Nanoscale*, 10:22802–22809, 2018.

[44] Jef Wagner and Roya Zandi. The robust assembly of small symmetric nanoshells. *Biophysical journal*, 109(5):956–965, 2015.

[45] Y. F. Hu, R. Zandi, A. Anavitarte, C. M. Knobler, and W. M. Gelbart. Packaging of a polymer by a viral capsid: The interplay between polymer length and capsid size. *Biophys. J.*, 94:1428, 2008.

[46] Michael A Krol, Norman H Olson, John Tate, John E Johnson, Timothy S Baker, and Paul Ahlquist. Rna-controlled polymorphism in the in vivo assembly of 180-subunit and 120-subunit virions from a single capsid protein. *Proceedings of the National Academy of Sciences*, 96(24):13650–13655, 1999.

[47] Jiying Ning, Gonca Erdemci-Tandogan, Ernest L Yufenyuy, Jef Wagner, Benjamin A Himes, Gongpu Zhao, Christopher Aiken, Roya Zandi, and Peijun Zhang. In vitro protease cleavage and computer simulations reveal the hiv-1 capsid maturation pathway. *Nature Communications*, 7:13689, 2016.

[48] Antoni Luque, Roya Zandi, and David Reguera. Optimal architectures of elongated viruses. *PNAS*, 107(12):5323–5328, 2010.

[49] R. F. Bruinsma, M. Comas-Garcia, R. F. Garmann, and A. Y. Grosberg. Equilibrium self-assembly of small RNA viruses. *Physical Review E*, 93(3):1–14, 2016.

[50] Peter G. Stockley, Reidun Twarock, Saskia E. Bakker, Amy M. Barker, Alexander Borodavka, Eric Dykeman, Robert J. Ford, Arwen R. Pearson, Simon E. V. Phillips, Neil A. Ranson, and Roman Tuma. Packaging signals in single-stranded RNA viruses: natures alternative to a purely electrostatic assembly mechanism. *J. Biol. Phys.*, 39:277, 2013.

[51] J. Wagner, G. Erdemci-Tandogan, and Roya Zandi. Adsorption of annealed branched polymers on curved surfaces. *J. Phys.:Condens. Matter*, 27:495101, 2015.

[52] P. van der Schoot and R Bruinsma. Electrostatics and the assembly of an RNA virus. *Phys. Rev. E*, 71:061928, 2005.

[53] R. Zandi and P. van der Schoot. Size Regulation of ss-RNA Viruses. *Biophys. J.*, 96:9, 2009.

[54] A. Siber, R. Zandi, and R. Podgornik. Thermodynamics of nanospheres encapsulated in virus capsids. *Phys. Rev. E*, 81:051919, 2010.

[55] Gonca Erdemci-Tandogan, Henri Orland, and Roya Zandi. Rna base pairing determines the conformations of rna inside spherical viruses. *Phys. Rev. Lett.*, 119:188102, Oct 2017.

[56] P.-G. de Gennes. *Scaling concepts in polymer physics*. Cornell University Press, 1979.

[57] Vamseedhar Rayaprolu, Alan Moore, Joseph Che-Yen Wang, Boon Chong Goh, Juan R Perilla, Adam Zlotnick, and Suchetana Mukhopadhyay. Length of encapsidated cargo impacts stability and structure of in vitro assembled alphavirus core-like particles. *Journal of Physics: Condensed Matter*, 29(48):484003, 2017.

[58] S. F. Edwards. The statistical mechanics of polymers with excluded volume. *Proc. Phys. Soc.*, 85:613, 1965.

[59] I. Borukhov, D. Andelman, and H. Orland. Random polyelectrolytes and polyampholytes in solution. *Euro. Phys. J. B*, 5:869, 1998.

[60] Glenn Fredrickson. *The equilibrium theory of inhomogeneous polymers*, volume 134. Oxford University Press on Demand, 2006.

[61] M. Doi and S. F. Edwards. *The Theory of Polymer Dynamics*, volume 73 of *International Series of Monographs on Physics*. Oxford Science Publications, Oxford, 1986.

[62] J A Abels, F Moreno-Herrero, T van der Heijden, C Dekker, and N H Dekker. Single-Molecule Measurements of the Persistence Length of Double-Stranded RNA. *Biophysical Journal*, 88(4):2737–2744, dec 2005.

[63] H. Ji and D. Hone. Polymer adsorption on rough surfaces. 2. Good solvent conditions. *Macromolecules*, 21:2600, 1988.

[64] Xingkun Man, Shuang Yang, Dadong Yan, and An Chang Shi. Adsorption and depletion of polyelectrolytes in charged cylindrical system within self-consistent field theory. *Macromolecules*, 41(14):5451–5456, 2008.

[65] Q Wang, T Taniguchi, and G H Fredrickson. Self-consistent field theory of polyelectrolyte systems. *Journal of Physical Chemistry B*, 108(21):6733–6744, 2004.

[66] J. F. Joanny. Polyelectrolyte adsorption and charge inversion. *Eur. Phys. J. B*, 9:117, 1999.

[67] P. A. Pincus, C. J. Sandroff, and T. A. Witten. Polymer adsorption on colloidal particles. *J. Physique*, 45:725–729, 1984.

[68] Daniel Hone, Hong Ji, and P. A. Pincus. Polymer adsorption on rough surfaces. 1. ideal long chain. *Macromolecules*, 20:2543, 1987.

[69] E. Eisenriegler, K. Kremer, and K. Binder. Adsorption of polymer chains at surfaces: Scaling and Monte Carlo analyses. *J. Chem. Phys.*, 77:6296–6320, 1982.

[70] Melanie Brasch, Ilja K. Voets, Melissa S. T. Koay, and Jeroen J. L. M. Cornelissen. Phototriggered cargo release from virus-like assemblies. *Faraday Discuss.*, 166:47–57, 2013.

[71] S. Lindhoud S. J. Maassen, M. V. de Ruiter and J. J. L. M. Cornelissen. Minimal oligonucleotide length required for the assembly of the cowpea chlorotic mottle virus. *under review*, 2017.

[72] J. B. Bancroft. The self-assembly of spherical plant viruses. *Adv. Virus Res.*, 16:99, 1970.

[73] R. F. Bruinsma. Physics of RNA and viral assembly. *Euro. Phys. J. E*, 19:303, 2006.

[74] S. Fejer, D. Chakrabarti, and D. Wales. Emergent complexity from simple anisotropic building blocks: Shells, tubes, and spirals. *ACS nano*, 4:219, 2010.

[75] D. C. Rapaport. Self-assembly of polyhedral shells: A molecular dynamics study. *Phys Rev E*, 70:051905, 2004.

[76] Ting Chen, Zhenli Zhang, and Sharon C. Glotzer. A precise packing sequence for self-assembled convex structures. *PNAS*, 104:717, 2007.

[77] Stefan Paquay, Halim Kusumaatmaja, David J. Wales, Roya Zandi, and Paul van der Schoot. Energetically favoured defects in dense packings of particles on spherical surfaces. *Soft Matter*, 12:5708–5717, 2016.

[78] M. C. Daniel, I. B. Tsvetkova, Z. T. Quinkert, A. Murali, M. De, V. M. Rotello, C. C. Kao, and B. Dragnea. Role of Surface Charge Density in Nanoparticle-Templated Assembly of Bromovirus Protein Cages. *ACS Nano*, 4:3853, 2010.

[79] R. D. Cadena-Nava, Y. F. Hu, R. F. Garmann, B. Ng, A. N. Zelikin, C. M. Knobler, and W. M. Gelbart. Exploiting Fluorescent Polymers To Probe the Self-Assembly of Virus-like Particles. *J. Phys. Chem. B*, 115:2386, 2011.

[80] A. L. Bozic, A. Siber, and R. Podgornik. How simple can a model of an empty viral capsid be? Charge distributions in viral capsids. *J. Biol. Phys.*, 38:657, 2012.

[81] Paul van der Schoot and Roya Zandi. Impact of the topology of viral rnas on their encapsulation by virus coat proteins. *J. Biol. Phys.*, 39(2):289–299, 2013.

[82] Siyu Li, Henri Orland, and Roya Zandi. Self consistent field theory of virus assembly. *Journal of Physics: Condensed Matter*, 30(14):144002, 2018.

[83] Dawn Marshall and Anette Schneemann. Specific packaging of nodaviral rna2 requires the n-terminus of the capsid protein. *Virology*, 285(1):165 – 175, 2001.

[84] Steven B. Larson, Robert W. Lucas, and Alexander McPherson. Crystallographic structure of the t=1 particle of brome mosaic virus. *Journal of Molecular Biology*, 346(3):815 – 831, 2005.

[85] Mathijs Janssen, Andreas Härtel, and René van Roij. Boosting capacitive blue-energy and desalination devices with waste heat. *Phys. Rev. Lett.*, 113:268501, Dec 2014.

[86] T. C. Lubensky and J. Isaacson. Statistic of Lattice Animals and Dilute Branched Polymers. *Phys. Rev. A*, 20:2130, 1979.

[87] T. T. Nguyen and R. F. Bruinsma. RNA condensation and the wetting transition. *Phys. Rev. Lett.*, 97:108102, 2006.

[88] S. I. Lee and T. T. Nguyen. Radial Distribution of RNA Genomes Packaged inside Spherical Viruses. *Phys. Rev. Lett.*, 100:198102, 2008.

[89] K. Elleuch, F. Lequeux, and P. Pfeuty. Crosslink Effects on Equilibrium Polymers. *J. Phys. I France*, 5:465, 1995.

[90] Yibin Zheng and Peter C. Doerschuk. Explicit computation of orthonormal symmetrized harmonics with application to the identity representation of the icosahedral group. *SIAM Journal on Mathematical Analysis*, 32(3):538–554, 2000.

[91] Antonio Šiber and Rudolf Podgornik. Role of electrostatic interactions in the assembly of empty spherical viral capsids. *Phys. Rev. E*, 76:061906, 2007.

[92] C. L. Ting, J. Z. Wu, and Z. G. Wang. Thermodynamic basis for the genome to capsid charge relationship in viral encapsidation. *PNAS*, 108:16986, 2011.

[93] P. G. Higgs. RNA secondary structure: physical and computational aspects. *Q. Rev. Biophys.*, 33:199, 2000.

[94] Huimin Chen, Steve P. Meisburger, Suzette A. Pabit, Julie L. Sutton, Watt W. Webb, and Lois Pollack. Ionic strength-dependent persistence lengths of single-stranded rna and dna. *PNAS*, 109(3):799–804, 2012.

[95] P. Kebbekus, D. E. Draper, and P. Hagerman. Persistence length of RNA. *Biochemistry*, 34:4354, 1995.

[96] Ruth Nussinov, George Pieczenik, Jerrold R. Griggs, and Daniel J. Kleitman. Algorithms for loop matchings. *SIAM Journal on Applied Mathematics*, 35(1):68–82, 1978.

[97] J S McCaskill. The equilibrium partition function and base pair binding probabilities for RNA secondary structure. *Biopolymers*, 29(6-7):1105–1119, 1990.

[98] M. Zuker. Mfold web server for nucleic acid folding and hybridization prediction. *Nucleic Acids Res.*, 31:3406, 2003.

[99] D Schwab and R. F. Bruinsma. Flory theory of the folding of designed rna molecules. *J Phys Chem B.*, 113:3880, 2009.

[100] A. Y. Grosberg. Disordered polymers. *Physics-Uspekhi*, 40:125, 1997.

[101] Li Tai Fang, William M. Gelbart, and Avinoam Ben-Shaul. The size of RNA as an ideal branched polymer. *Journal of Chemical Physics*, 135(15):155105, 2011.

[102] Nikesh Patel, Eric C. Dykeman, Robert H. A. Coutts, George P. Lomonossoff, David J. Rowlands, Simon E. V. Phillips, Neil Ranson, Reidun Twarock, Roman Tuma, and Peter G. Stockley. Revealing the density of encoded functions in a viral rna. *Proceedings of the National Academy of Sciences*, 112(7):2227–2232, 2015.

[103] Siyu Li, Gonca Erdemci-Tandogan, Jef Wagner, Paul Van Der Schoot, and Roya Zandi. Impact of a nonuniform charge distribution on virus assembly. *Physical Review E*, 96(2):022401, 2017.

[104] A. M. Yoffe, P. Prinsen, A. Gopal, C. M. Knobler, W. M. Gelbart, and A. Ben-Shaul. Predicting the sizes of large RNA molecules. *PNAS*, 105:16153, 2008.

[105] A. Gopal, Egecioglu D.E., Yoffe A.M., Ben-Shaul A, Rao ALN, C. M. Knobler, W. M. Gelbart, and A. Ben-Shaul. Viral RNAs Are Unusually Compact. *PLoS ONE*, 9:e105875, 2014.

[106] Christian Beren, Lisa L. Dreesens, Katherine N. Liu, Charles M. Knobler, and William M. Gelbart. The effect of rna secondary structure ontheself-assembly of viral capsids. *Biophysical Journal*, 113(2):339–347, 2017.

[107] A. McPherson. Micelle formation and crystallization as paradigms for virus assembly. *BioEssays*, 27:447, 2005.

[108] Gonca Erdemci-Tandogan, Jef Wagner, Paul van der Schoot, and Roya Zandi. Role of genome in the formation of conical retroviral shells. *J. Phys. Chem. B*, 120:6298, 2016.

[109] A. Shafir, D. Andelman, and R. R. Netz. Adsorption and depletion of polyelectrolytes from charged surfaces. *J. Chem. Phys.*, 119:2355, 2003.

[110] P.-G. de Gennes. Polymers a t an Interface. 2. Interaction between Two Plates Carrying Adsorbed Polymer Layers. *Macromolecules*, 15:492, 1982.

[111] Alexander Borodavka, SurendraW. Singaram, PeterG. Stockley, WilliamM. Gelbart, Avinoam Ben-Shaul, and Roman Tuma. Sizes of long rna molecules are determined by the branching patterns of their secondary structures. *Biophysical Journal*, 111(10):2077 – 2085, 2016.

[112] A. R. Bausch, M. J. Bowick, A. Cacciuto, A. D. Dinsmore, M. F. Hsu, D. R. Nelson, M. G. Nikolaides, A. Travesset, and D. A. Weitz. Grain boundary scars and spherical crystallography. *Science*, 299(5613):1716–1718, 2003.

[113] William T. M. Irvine, Vincenzo Vitelli, and Paul M. Chaikin. Pleats in crystals on curved surfaces. *Nature*, 468(7326):947–951, December 2010.

[114] Jiying Ning, Gonca Erdemci-Tandogan, Ernest L Yufenyuy, Jef Wagner, Benjamin A Himes, Gongpu Zhao, Christopher Aiken, Roya Zandi, and Peijun Zhang. In vitro protease cleavage and computer simulations reveal the hiv-1 capsid maturation pathway. *Nature communications*, 7:13689, 2016.

[115] Jack Lidmar, Leonid Mirny, and David R Nelson. Virus shapes and buckling transitions in spherical shells. *Physical Review E*, 68(5):051910, 2003.

[116] Graziano Vernizzi and Monica Olvera de la Cruz. Faceting ionic shells into icosahedra via electrostatics. *Proceedings of the National Academy of Sciences*, 104(47):18382–18386, November 2007.

[117] L Landau and E.M. Lifshitz. *Theory of Elasticity*. Butterworth-Heinemann; 3 edition, 1985.

[118] J.F Sadoc and R. Mosseri. *Geometrical Frustration*. Cambridge University Press, 1999.

[119] David R. Nelson. Order, frustration, and defects in liquids and glasses. *Phys. Rev. B*, 28(10):5515–5535, November 1983.

[120] Alex Travesset. Nanoparticle superlattices as quasi-frank-kasper phases. *Phys. Rev. Lett.*, 119(11):115701, September 2017.

[121] D.R. Nelson. *Defects and Geometry in Condensed Matter Physics*. Cambridge Press, 2002.

[122] P. Chaikin and T. Lubensky. *Principles of condensed matter physics*. Cambridge University Press, 2003.

[123] M. Nakahara. *Geometry, Topology and Physics*. Adam Hilger, 1990.

[124] HS Seung and David R Nelson. Defects in flexible membranes with crystalline order. *Physical Review A*, 38(2):1005, 1988.

[125] S. Schneider and G. Gompper. Shapes of crystalline domains on spherical fluid vesicles. *Europhys. Lett.*, 70:136, 2005.

[126] Alexander Yu. Morozov and Robijn F. Bruinsma. Assembly of viral capsids, buckling, and the asaro-grinfeld-tiller instability. *Phys. Rev. E*, 81:041925, Apr 2010.

[127] Gregory M. Grason. Topological defects in twisted bundles of two-dimensionally ordered filaments. *PRL*, 105(4):045502, July 2010.

[128] Gregory M Grason. Defects in crystalline packings of twisted filament bundles. i. continuum theory of disclinations. *Physical Review E*, 85(3):031603, 2012.

[129] Gregory M. Grason. Colloquium: Geometry and optimal packing of twisted columns and filaments. *RMP*, 87(2):401–419, May 2015.

[130] Martin Castelnovo. Viral self-assembly pathway and mechanical stress relaxation. *Phys. Rev. E*, 95:052405, May 2017.

[131] Mark J Bowick, David R Nelson, and Alex Travesset. Interacting topological defects on frozen topographies. *Physical Review B*, 62(13):8738, 2000.

[132] M. Bowick, A. Cacciuto, D. R. Nelson, and A. Travesset. Crystalline order on a sphere and the generalized thomson problem. *Physical Review Letters*, 89(18):185502–185505, 2002.

[133] Mark J. Bowick, Angelo Cacciuto, David R. Nelson, and Alex Travesset. Crystalline particle packings on a sphere with long-range power-law potentials. *Physical Review B (Condensed Matter and Materials Physics)*, 73(2):024115–16, 2006.

[134] Luca Giomi and Mark Bowick. Crystalline order on riemannian manifolds with variable gaussian curvature and boundary. *Phys. Rev. B*, 76:054106, Aug 2007.

[135] W.T. Koiter. On the nonlinear theory of thin elastic shells. *Proc. Kon. Ned. Acad. Wetensch. B*, 69:1–54, 1966.

[136] E. Efrati, E. Sharon, and R. Kupferman. Elastic theory of unconstrained non-euclidean plates. *Journal of the Mechanics and Physics of Solids*, 57(4):762–775, April 2009.

[137] Michael Moshe, Eran Sharon, and Raz Kupferman. Elastic interactions between two-dimensional geometric defects. *Phys. Rev. E*, 92:062403, Dec 2015.

[138] Alex Travesset. Structure of curved crystals in the thermodynamic limit and the perfect screening condition. *Physical Review E*, 94:063001, Dec 2016.

[139] Siyu Li, Polly Roy, Alex Travesset, and Roya Zandi. Why large icosahedral viruses need scaffolding proteins. *Proc Natl Acad Sci USA*, 115(43):10971, October 2018.

[140] Jemal Guven, J. A. Hanna, Osman Kahraman, and Martin Michael Mller. Dipoles in thin sheets. *Eur. Phys. J. E*, 36(9), September 2013.

[141] M. Bowick and A. Travesset. The geometric structure of bond orientational order. *J. Phys. A:Math. Gen.*, 34:1535, 2001.

[142] Amir Azadi and Gregory M. Grason. Emergent structure of multidislocation ground states in curved crystals. *Phys. Rev. Lett.*, 112:225502, Jun 2014.

[143] Amir Azadi and Gregory M. Grason. Neutral versus charged defect patterns in curved crystals. *Phys. Rev. E*, 94:013003, Jul 2016.

[144] Alex Travesset. Universality in the screening cloud of dislocations surrounding a disclination. *Physical Review B (Condensed Matter and Materials Physics)*, 68(11):115421–15, 2003.

[145] Dmitri V. Talapin, Elena V. Shevchenko, Maryna I. Bodnarchuk, Xingchen Ye, Jun Chen, and Christopher B. Murray. Quasicrystalline order in self-assembled binary nanoparticle superlattices. *Nature*, 461(7266):964–967, October 2009.

[146] Sebastien J. P. Callens and Amir A. Zadpoor. From flat sheets to curved geometries: Origami and kirigami approaches. *Materials Today*, 21(3):241–264, April 2018.

[147] Donald LD Caspar and Aaron Klug. Physical principles in the construction of regular viruses. *Cold Spring Harbor Symp. Quant. Biol.*, 27:1–24, 1962.

[148] Anastasia A Aksyuk, William W Newcomb, Naiqian Cheng, Dennis C Winkler, Juan Fontana, J Bernard Heymann, and Alasdair C Steven. Subassemblies and asymmetry in assembly of herpes simplex virus procapsid. *MBio*, 6(5):e01525–15, 2015.

[149] Ali Saad, Z Hong Zhou, Joanita Jakana, Wah Chiu, and Frazer J Rixon. Roles of triplex and scaffolding proteins in herpes simplex virus type 1 capsid formation suggested by structures of recombinant particles. *Journal of virology*, 73(8):6821–6830, 1999.

[150] T. Erber and G. M. Hockney. Equilibrium configurations of n equal charges on a sphere. *Journal of Physics A: Mathematical and General*, 24(23):L1369, 1991.

[151] J. R. Morris, D. M. Deaven, and K. M. Ho. Genetic-algorithm energy minimization for point charges on a sphere. *Phys. Rev. B*, 53:R1740–R1743, Jan 1996.

[152] Graziano Vernizzi and Monica Olvera de la Cruz. Faceting ionic shells into icosahedra via electrostatics. *Proceedings of the National Academy of Sciences*, 104:18382–18386, 2007.

[153] Paul WK Rothemund. Folding dna to create nanoscale shapes and patterns. *Nature*, 440(7082):297, 2006.

[154] Zhiheng Yu, Megan J Dobro, Cora L Woodward, Artem Levandovsky, Cindy M Danielson, Virginie Sandrin, Jiong Shi, Christopher Aiken, Roya Zandi, Thomas J Hope, et al. Unclosed hiv-1 capsids suggest a curled sheet model of assembly. *Journal of molecular biology*, 425(1):112–123, 2013.

[155] TT Nguyen, RF Bruinsma, and WM Gelbart. Continuum theory of retroviral capsids. *Physical review letters*, 96(7):078102, 2006.

[156] Graziano Vernizzi, Rastko Sknepnek, and Monica Olvera De La Cruz. Platonic and archimedean geometries in multicomponent elastic membranes. *Proceedings of the National Academy of Sciences*, 108(11):4292–4296, 2011.

[157] Joshua A. Anderson, Chris D. Lorenz, and A. Travesset. General purpose molecular dynamics simulations fully implemented on graphics processing units. *Journal of Computational Physics*, 227(10):5342 – 5359, 2008.

[158] Jens Glaser, Trung Dac Nguyen, Joshua A. Anderson, Pak Lui, Filippo Spiga, Jaime A. Millan, David C. Morse, and Sharon C. Glotzer. Strong scaling of general-purpose molecular dynamics simulations on gpus. *Computer Physics Communications*, 192:97 – 107, 2015.

[159] Huixin Bao, Wolfgang Peukert, and Robin Klupp Taylor. One-pot colloidal synthesis of plasmonic patchy particles. *Advanced Materials*, 23(22-23):2644–2649, 2011.

[160] Jonas Korlach, Petra Schwille, Watt W. Webb, and Gerald W. Feigenson. Characterization of lipid bilayer phases by confocal microscopy and fluorescence correlation spectroscopy. *Proc Natl Acad Sci USA*, 96(15):8461, July 1999.

[161] Shani Guttman, Zvi Sapir, Moty Schultz, Alexander V. Butenko, Benjamin M. Ocko, Moshe Deutsch, and Eli Sloutskin. How faceted liquid droplets grow tails. *Proceedings of the National Academy of Sciences*, 113(3):493–496, January 2016.

[162] Guangnan Meng, Jayson Paulose, David R. Nelson, and Vinothan N. Manoharan. Elastic instability of a crystal growing on a curved surface. *Science*, 343(6171):634, February 2014.

[163] I. Borukhov, D. Andelman, and H. Orland. Polyelectrolyte Solutions between Charged Surfaces. *Europhys. Lett.*, 32:499, 1995.

Part V

Appendix

Appendix A

Appendix: Self consistent field theory

A.1 Self consistent field theory

In this section we derive several equations presented in Section II of the paper. Using a Hubbard-Stratanovich transformation, the partition function of Eq. 1 reads

$$\mathcal{Z} = \int \mathcal{D}w(r)\mathcal{D}\phi(r)\ e^{\log Q[iw(r)+i\tau\phi(r)]} \\ e^{\int dr\left(-\frac{1}{2u_0}w(r)^2-\frac{\beta\epsilon}{2}(\nabla\phi(r))^2+2\lambda\cosh(i\beta e\phi(r))-i\beta\rho_0(r)\phi(r)\right)} \tag{A.1}$$

where λ is the salt ion fugacity and

$$Q = \int \mathcal{D}r(s)e^{-\frac{3}{2a^2}\int_0^N ds\dot{r}^2-i\int_0^N ds(w(r(s))+\beta\tau\phi(r(s)))} \tag{A.2}$$

is the partition function of a single Gaussian chain in the external field $(iw(r) + i\beta\tau\phi(r))$. Now performing the saddle-point approximation on the two fields $w(r)$ and $\phi(r)$, we get

from Eq. A.1

$$w(r) = u_0 \frac{\delta \log Q}{\delta w(r)} \tag{A.3}$$

$$-\epsilon \nabla^2 \phi(r) = 2\lambda i e \sinh(i\beta e\phi) - i\rho_0(r) + \frac{\delta \log Q}{\delta \phi(r)} \tag{A.4}$$

At this stage, from Eqs. (A.3) and (A.4), we can anticipate that the fields $w(r)$ and $\phi(r)$ are pure imaginary and redefine $iw \to w$ and $i\phi \to \phi$.

Using standard quantum mechanical notations, we may write

$$Q = \int dr dr' \langle r|e^{-NH}|r'\rangle \tag{A.5}$$

where the Hamiltonian H is given by

$$H = -\frac{a^2}{6}\nabla^2 + (w(r) + \beta\tau\phi(r)) \tag{A.6}$$

From Eqs. (A.3) and (A.2), we have

$$\begin{aligned} \frac{\delta \log Q}{\delta w(r)} &= \frac{1}{Q}\int \mathcal{D}r(s) \int_0^N ds\ \delta(r - r(s))\ e^{-\frac{3}{2a^2}\int_0^N ds\dot{r}^2 - \int ds(w(r(s)) + \beta\tau\phi(r(s)))} \\ &= \rho(r) \end{aligned} \tag{A.7}$$

where $\rho(r)$ is the monomer density.

Using quantum mechanical notation, we have

$$\frac{\delta \log Q}{\delta w(r)} = \frac{1}{Q}\int_0^N ds \int dr_1\ dr_2 \langle r_1|e^{-(N-s)H}|r\rangle\langle r|e^{-sH}|r_2\rangle \tag{A.8}$$

Defining the propagator $q(r,s)$ as

$$q(r,s) = \frac{1}{\sqrt{Q}}\int dr' \langle r|e^{-sH}|r'\rangle \tag{A.9}$$

we have

$$\frac{\delta \log Q}{\delta w(r)} = \rho(r) = \int_0^N ds\ q(r, N-s)q(r,s) \tag{A.10}$$

Using the above equations, Eqs. (A.3), (A.4) become

$$w(r) = u_0\rho(r) \tag{A.11}$$

$$-\epsilon\nabla^2\phi(r) = -2\lambda e \sinh(\beta e\phi) + \rho_0(r) + \beta\tau\rho(r) \tag{A.12}$$

and the propagator $q(r,s)$ satisfies the diffusion equation

$$\frac{\partial q(r,s)}{\partial s} = \frac{a^2}{6}\nabla^2 q(r,s) - \left(w(r) + \beta\tau\phi(r)\right) q(r,s) \tag{A.13}$$

which can be recast in the form of the Schrödinger equation $\left(\frac{\partial}{\partial s} + H\right) q(r,s) = 0$ with the Halmitonian H given by Eq. A.6.

Numerically, we solve Eqs. (A.10), (A.11), (A.12) and (A.13) recursively until convergence, with initial condition $q(r,0) = 1/\sqrt{Q}$

A.2 Ground state dominance approximation

Expanding the partition function Q as well as the propagator q on the normalized eigenstates $|\psi_n\rangle$ with eigenvalues E_n of the Hamiltonian H

$$H|\psi_n\rangle = E_n|\psi_n\rangle \tag{A.14}$$

$$\int dr\psi_n^2(r) = 1 \tag{A.15}$$

we have

$$Q = \int drdr'\langle r|e^{-NH}|r'\rangle = \sum_n \int drdr\psi_n(r)\psi_n(r')e^{-NE_n} \tag{A.16}$$

Reducing the expansion (A.16) to the lowest eigenstates of H, we see that we can keep only the ground state ψ_0 with energy E_0, provided the first excited state ψ_1 has an

eigenvalue E_1 such that

$$N\Delta \ll 1 \tag{A.17}$$

where $\Delta = E_1 - E_0$ is the gap in the eigenvalues.

This is the so-called *Ground State Dominance* approximation (GSDA). It implies

$$Q \approx I_0^2 e^{-NE_0} \tag{A.18}$$

where $I_0 = \int dr\psi_0(r) = \sqrt{Q}e^{\frac{NE_0}{2}}$ and

$$\begin{aligned} q(r,s) &\approx \frac{1}{\sqrt{Q}} e^{-sE_0}\psi_0(r) I_0 \\ &= e^{\frac{NE_0}{2}} e^{-sE_0}\psi_0(r) \end{aligned} \tag{A.19}$$

and the density (A.10) becomes

$$\rho(r) = N\psi_0^2(r) \tag{A.20}$$

The coupled equations (A.11, A.12) can be written as

$$-E_0\psi_0(r) = \frac{a^2}{6}\nabla^2\psi_0(r) - \left(u_0 N\psi_0(r)^2 + \beta\tau\phi(r)\right)\psi_0(r) \tag{A.21}$$

$$-\epsilon\nabla^2\phi(r) = -2\lambda e \sinh(\beta e\phi) + \rho_0(r) + \beta\tau N\psi_0(r)^2 \tag{A.22}$$

Using the normalization $\sqrt{N}\psi_0(r) \to \psi_0(r)$, the above equations become the familiar Euler-Lagrangian equations [36, 103, 163]

$$-E_0\psi_0(r) = \frac{a^2}{6}\nabla^2\psi_0(r) - u_0\psi_0(r)^3 - \beta\tau\phi(r)\psi_0(r) \tag{A.23}$$

$$-\epsilon\nabla^2\phi(r) = -2\lambda e \sinh(\beta e\phi) + \rho_0(r) + \beta\tau\psi_0(r)^2 \tag{A.24}$$

with the constraint

$$N = \int \psi_0(r)^2 dr \tag{A.25}$$

A.3 Persistence length

The persistence length is the correlation length of the tangents of the polymer.

$$C(s,s') = \frac{1}{a^2}\left(< \dot{r}(s)\cdot\dot{r}(s') > - < \dot{r}(s) > \cdot < \dot{r}(s') > \right) \tag{A.26}$$

where the average is calculated with the Boltzmann weight given by the partition function Eq. A.1. Note that the true correlation length requires to use unit tangent vectors rather than $\dot{r}$. With spherical geometry we have $< \dot{r}(s) >= 0$, and the persistence length is given by

$$\begin{aligned} C(s,s') &= \frac{1}{a^2} < \dot{r}(s)\cdot\dot{r}(s') > \\ &= \frac{1}{a^2}\frac{1}{\mathcal{Z}_0}\int \mathcal{D}w(r)\mathcal{D}\phi(r)\; e^{\int dr\left(-\frac{1}{2u_0}w(r)^2 - \frac{\beta\epsilon}{2}(\nabla\phi(r))^2 + 2\lambda\cosh(i\beta e\phi(r)) - i\beta\rho_0(r)\phi(r)\right)} \\ &\quad \times \int \mathcal{D}r(s)\dot{r}(s)\dot{r}(s')e^{-\frac{3}{2a^2}\int_0^N ds\dot{r}_s^2 - \int_0^N ds(w(r(s)) + \beta\tau\phi(r(s)))} \end{aligned} \tag{A.27}$$

Fixing the fields $w(r)$ and $\phi(r)$ to their SCFT value, the above expression (A.27) simplifies to

$$\begin{aligned} C(s,s') &= \frac{1}{a^2}\frac{1}{Q}\int \mathcal{D}r_s\; \dot{r}(s)\dot{r}(s')e^{-\frac{3}{2a^2}\int_0^N ds\dot{r}_s^2 - \int_0^N ds(w(r(s)) + \beta\tau\phi(r(s)))} \\ &= \frac{1}{a^2}\frac{1}{Q}\int dr_N dr_0 dr dr' \dot{r}(s)\dot{r}(s') < r_N|e^{-(N-s)H}|r >< r|e^{-(s-s')H}|r' >< r'|e^{-s'H}|r_0 > \end{aligned} \tag{A.28}$$

where we have assumed $s > s'$. Using the correspondance principle

$$\begin{aligned} p &= \frac{1}{i}\frac{\partial}{\partial r} \\ \dot{r} &= \frac{1}{i}\frac{a^2}{3}p = -\frac{a^2}{3}\frac{\partial}{\partial r} \end{aligned} \tag{A.29}$$

which is a direct property of the Fourier transform, we obtain the persistence length as

$$\begin{aligned}
C(s,s') &= \frac{1}{a^2 Q}\int dr_N dr_0 dr dr' \left(-\frac{a^2}{3}\frac{\partial}{\partial r}\right)\left(-\frac{a^2}{3}\frac{\partial}{\partial r'}\right) \\
&\times \; < r_N|e^{-(N-s)H}|r] >< r|e^{-(s-s')H}|r' >< r'|e^{-s'H}|r_0 > \\
&= \frac{a^2}{9Q}\int dr dr' \int dr_N \left(\frac{\partial}{\partial r} < r_N|e^{-(N-s)H}|r >\right) \\
&\times \; < r|e^{-(s-s')H}|r' > \int dr_0 \left(\frac{\partial}{\partial r'} < r'|e^{-s'H}|r_0 >\right) \\
&= \frac{a^2}{9}\int dr dr' \left(\frac{\partial}{\partial r} q(r, N-s)\right) \\
&\times \; < r|e^{-(s-s')H}|r' > \left(\frac{\partial}{\partial r'} q(r', s')\right) \\
&= \frac{a^2}{9}\sum_n \int dr dr' e^{-(s-s')E_n} \\
&\times \; \left(\psi_n(r)\frac{\partial}{\partial r} q(r, N-s)\right)\left(\psi_n(r')\frac{\partial}{\partial r'} q(r', s')\right)
\end{aligned} \tag{A.30}$$

Having solved the SCFT equations, the full Hamiltonian (A.6) can be diagonalized numerically and the above formula allows to compute the full correlation function, in the SCFT approximation.

If we restrict ourselves purely to the GSDA, using Eqs. (A.18) and (A.19), we obtain

$$\begin{aligned}
C(s,s') &= \frac{a^2}{9}\int dr dr' \left(\frac{\partial}{\partial r} e^{\frac{NE_0}{2}} e^{-(N-s)E_0}\psi_0(r)\right) \\
&\times \; e^{-(s-s')E_0}\psi_0(r)\psi_0(r')\left(\frac{\partial}{\partial r'} e^{\frac{NE_0}{2}} e^{-s'E_0}\psi_0(r')\right) \\
&= \frac{a^2}{9}\int dr dr' \left(\frac{\partial}{\partial r}\psi_0(r')\right)\psi_0(r) \\
&\times \; \psi_0(r')\left(\frac{\partial}{\partial r'}\psi_0(r')\right)\frac{a^2}{9}\left(\int dr \psi_0(r)\frac{\partial}{\partial r}\psi_0(r)\right)^2 \\
&= 0
\end{aligned} \tag{A.31}$$

where we have used the fact that

$$\int \psi_0(r)\frac{\partial}{\partial r}\psi_0(r)\ dr = \frac{1}{2}\int \frac{\partial}{\partial r}\psi_0^2(r) = 0$$

Therefore, in the GSDA, the persistence length vanishes, and this is due to the fact that in this case, the chain constraint is absent.

If the system is confined in the viral shell and there is a sizeable gap, rather than staying in the ground state, we can restrict the expansion to the first excited state. Then

$$< r'|e^{-sH}|r >= e^{-sE_0}\psi_0(r)\psi_0(r') + e^{-sE_1}\psi_1(r)\psi_1(r') \tag{A.32}$$

and Eq (A.9) can be written as

$$\begin{aligned} q(r,s) &= \frac{1}{\sqrt{Q}}\int dr_0 < r|e^{-sH}|r_0 > \\ &= \frac{1}{\sqrt{Q}}\left(e^{-sE_0}\psi_0(r)\int dr_0\psi_0(r_0) + e^{-sE_1}\psi_1(r)\int dr_0\psi_1(r_0)\right) \\ &= \frac{1}{\sqrt{Q}}\left(e^{-sE_0}I_0\psi_0(r) + e^{-sE_1}I_1\psi_1(r)\right) \end{aligned} \tag{A.33}$$

where $I_0 = \int dr\ \psi_0(r)$, and $I_1 = \int dr\ \psi_1(r)$. Plugging this result into Eq. A.30, the

persistence length is therefore

$$
\begin{aligned}
C(s,s') &= \frac{a^2}{9Q}\sum_{n=0}^{1}\int dr_s dr_{s'} e^{-(s-s')E_n} \\
&\times \left(\psi_n(r_s)\frac{\partial}{\partial r_s}\left(e^{-(N-s)E_0}I_0\psi_0(r_s) + e^{-(N-s)E_1}I_1\psi_1(r_s)\right)\right) \\
&\times \left(\psi_n(r_{s'})\frac{\partial}{\partial r_{s'}}\left(e^{-s'E_0}I_0\psi_0(r_{s'}) + e^{-s'E_1}I_1\psi_1(r_{s'})\right)\right) \\
&= \frac{a^2}{9Q}\left(e^{-(s-s')E_0}e^{-(N-(s-s'))E_1}I_1^2\left(\int dr\psi_0(r)\frac{\partial}{\partial r}\psi_1(r)\right)^2\right. \\
&\quad \left. + e^{-(s-s')E_1}e^{-(N-(s-s'))E_0}I_0^2\left(\int dr\psi_1(r)\frac{\partial}{\partial r}\psi_0(r)\right)^2\right) \\
&= A\left(e^{-(s-s')\Delta}\left(\int dr\psi_1(r)\frac{\partial}{\partial r}\psi_0(r)\right)^2\right. \\
&\quad \left. + e^{-(N-(s-s'))\Delta}\left(\frac{I_1}{I_0}\right)^2\left(\int dr\psi_0(r)\frac{\partial}{\partial r}\psi_1(r)\right)^2\right) \qquad \text{(A.34)}
\end{aligned}
$$

where we have used $\int \psi_0(r)\frac{\partial}{\partial r}\psi_0(r)\ dr = 0$, $A = \frac{a^2}{9}\frac{1}{Q}e^{-NE_0}I_0^2$, and $\Delta = E_1 - E_0$ which is the energy gap. So for $1 << s - s' << N$, we can read off the persistence length as

$$l_p = \frac{1}{\Delta} \qquad \text{(A.35)}$$

Appendix B

Appendix: Covariant theory

B.1 The Seung-Nelson result as a function of area

Seung-Nelson [124] quote, for a flat disclination

$$\frac{F}{Ys^2R^2} = 0.008 \ . \tag{B.1}$$

The radius is given by $R = na$, where n is an integer and a is the lattice constant. A more precise calculation computes this coefficient as 0.00785 [144]. This is a numerical calculation considering a pentagonal shape crystal containing $5n^2$ triangles. Each trianlge has an area $\frac{\sqrt{3}}{4}a^2$, hence

$$\frac{F}{YArea} = 0.008 \left(\frac{\pi}{3}\right)^2 /(5\sqrt{3}/4) \approx 0.00405 \ , \tag{B.2}$$

or 0.00400 with the more precise value [144]. This is the coefficient used in Eq. 5.81.

B.2 Geometry, curvature, vielbeins and the definition of the stress tensor

It should be noticed that the stress tensor, defined by Eq. 5.19 is in general different than the one defined in standard textbooks, such as Landau and Lifshitz, which we denote as $\hat{\sigma}^{\alpha\beta}$. We now show the relation between both tensors. For that purpose, we introduce the Vielbeins $e^{\alpha}{}_{\mu}$, defined as

$$\begin{aligned} g_{\mu\nu} &= e^{\alpha}{}_{\mu} e^{\beta}{}_{\mu} \delta_{\alpha\beta} \\ \delta_{\alpha\beta} &= e_{\alpha}{}^{\mu} e_{\beta}{}^{\mu} g_{\mu\nu} \end{aligned} \tag{B.3}$$

Then, there is the relation

$$\hat{\sigma}^{\alpha\beta} = e^{\alpha}{}_{\mu} e^{\beta}{}_{\nu} \sigma^{\mu\nu} \ . \tag{B.4}$$

The advantage of $\hat{\sigma}^{\alpha\beta}$ is that the units of all the components are the same. This is not the case for $\sigma^{\mu\nu}$. Obvious to say that all physical quantities have the same dimensions in either form.

Also, the line tension term Eq. 5.22 is simplified by

$$\int_{\partial\mathcal{B}} ds = \int_{\partial\mathcal{B}} \sqrt{g} dl = \int_{\partial\mathcal{B}} dx^{\mu} g_{\mu\nu} t^{\nu} \ , \tag{B.5}$$

where $t^{\nu} = \frac{1}{\sqrt{g}} \frac{dx^{\mu}}{dl}$ for any parameterization $x^{\mu}(l)$. Here t^{μ} is the unit tangent vector to the curve defining the boundary. Note that

$$g = g_{\mu\nu} \frac{dx^{\mu}}{dl} \frac{dx^{\nu}}{dl} \tag{B.6}$$

and $dx^\mu = \sqrt{g} t^\mu dl$. The variation of this term gives

$$\begin{aligned}\int_{\partial\mathcal{B}} dx^\mu \delta g_{\mu\nu} t^\nu &= -\int_{\partial\mathcal{B}} dx^\mu (\nabla_\nu \xi_\mu + \nabla_\mu \xi_\nu) t^\nu \\ &= \int_{\partial\mathcal{B}} dx^\mu (\xi_\mu \nabla_\nu + \xi_\nu \nabla_\mu) t^\nu \\ &= \int_{\partial\mathcal{B}} dx^\mu \nabla_\mu t^\nu \xi_\nu \ , \end{aligned} \tag{B.7}$$

where $dx^\mu \xi_\mu = 0$ as the vector ξ^μ is perpendicular to t^μ. Note that the vector

$$n_\rho = \sqrt{g} \epsilon_{\mu\rho} t^\mu \ , \tag{B.8}$$

is a unit vector, perpendicular to t^μ.

The variation in Eq. B.7 refers to $\delta g_{\alpha\beta}$ with the implicit condition $\delta \bar{g}_{\alpha\beta} = 0$, while the variation leading to Eq. 5.20 is with respect to $\delta \bar{g}_{\alpha\beta}$ with $\delta g_{\alpha\beta} = 0$. One notes, however, that the general transformation

$$\begin{aligned}\delta g_{\alpha\beta} &= \nabla_\alpha \xi_\beta + \nabla_\beta \xi_\alpha \\ \delta \bar{g}_{\alpha\beta} &= \bar{\nabla}_\alpha \xi_\beta + \bar{\nabla}_\beta \xi_\alpha \ , \end{aligned} \tag{B.9}$$

encodes a simple reparamaterization and therefore, under this transformation any term F_a appearing in the energy should satisfy

$$\delta F_a = \delta_g F_a + \delta_{\bar{g}} F_a = 0 \ , \tag{B.10}$$

hence, the correct variation, with respect to $\bar{g}_{\alpha\beta}$ picks up a minus sign, as compared with Eq. B.7,

$$\delta F_l = -\int_{\partial\mathcal{B}} dx^\mu \nabla_\mu t^\nu \xi_\nu \ , \tag{B.11}$$

as used in the main text.

B.3 Incompatibility metric approximations

B.3.1 Incompatibility metric approximation: target frame

The second order in the expansion Eq. 5.38 is given by

$$\begin{aligned} g^{(2)}_{\alpha\beta} &= -\frac{2}{Y}\left(g_{\alpha\beta}\Delta\chi^{(2)} - (1+\nu_P)\nabla_\alpha\nabla_\beta\chi^{(2)}\right) \\ &- \frac{2}{Y}\left(g_{\alpha\beta}g^{\rho\gamma}\Gamma^{\mu(1)}_{\rho\gamma} - (1+\nu_P)\Gamma^{\mu(1)}_{\alpha\beta}\right)\nabla_\mu\chi^{(1)} \\ &- \frac{1}{2}g^{(1)}_{\alpha\beta}g^{\gamma\sigma}g^{(1)}_{\gamma\sigma} \end{aligned} \tag{B.12}$$

Obviously, the expansion can be continued to all orders, and in this way a perturbative solution to Eq. 5.35 and Eq. 5.36 can be found. The goal is now to derive an explicit equation for $\chi^{(i)}$, as shown below.

B.3.2 Incompatibility metric approximation: reference frame

The second order in Eq. 5.49 can also be computed as:

$$\begin{aligned} \bar{g}^{(II)}_{\alpha\beta} &= \frac{2}{Y}\left(\bar{g}_{\alpha\beta}\bar{\Delta}\chi^{(II)} - (1+\nu_P)\bar{\nabla}_\alpha\bar{\nabla}_\beta\chi^{(II)}\right) \\ &+ \frac{1}{2}\bar{g}^{(I)}_{\alpha\beta}\bar{g}^{\gamma\sigma}\bar{g}^{(I)}_{\gamma\sigma} \end{aligned} \tag{B.13}$$

B.3.3 First order solution: target frame

We will compute the Ricci tensor $\bar{R}_{\sigma\nu} = \bar{R}^{\rho}_{\sigma\rho\nu}$, which from Eq. B.52 is

$$\bar{R}_{\sigma\nu} = R_{\sigma\nu} + \nabla_\mu\Gamma^{\mu(1)}_{\nu\sigma} - \nabla_\nu\Gamma^{\mu(1)}_{\mu\sigma} \ . \tag{B.14}$$

The first term is obtained from Eq. 5.40, Eq. B.50 and Eq. B.52, leading to

$$\begin{aligned} -Y\nabla_\mu\Gamma^{\mu(1)}_{\nu\sigma} &= \nabla_\sigma\nabla_\nu\Delta\chi^{(1)} - (1+\nu_P)g^{\mu\gamma}\nabla_\mu\nabla_\nu\nabla_\sigma\nabla_\gamma\chi^{(1)} \\ &+ \nabla_\nu\nabla_\sigma\Delta\chi^{(1)} - (1+\nu_P)g^{\mu\gamma}\nabla_\mu\nabla_\sigma\nabla_\nu\nabla_\gamma\chi^{(1)} \\ &- g_{\sigma\nu}\Delta^2\chi^{(1)} + (1+\nu_P)g^{\mu\gamma}\nabla_\mu\nabla_\gamma\nabla_\nu\nabla_\sigma\chi^{(1)} \end{aligned} \tag{B.15}$$

This is simplified by using Eq. B.38 and Eq. B.39

$$\begin{aligned} g^{\mu\gamma}\nabla_\mu\nabla_\gamma\nabla_\nu\nabla_\sigma\chi^{(1)} &= g^{\mu\gamma}\nabla_\mu\nabla_\nu\nabla_\gamma\nabla_\sigma\chi^{(1)} \\ &- g^{\mu\gamma}\nabla_\mu\left(R^\lambda{}_{\sigma\gamma\nu}\nabla_\lambda\chi^{(1)}\right) \end{aligned} \tag{B.16}$$

and

$$\begin{aligned} g^{\mu\gamma}\nabla_\mu\nabla_\sigma\nabla_\nu\nabla_\gamma\chi^{(1)} &= g^{\mu\gamma}\nabla_\sigma\nabla_\mu\nabla_\nu\nabla_\gamma\chi^{(1)} \\ &- g^{\mu\gamma}R^\lambda{}_{\nu\mu\sigma}\nabla_\lambda\nabla_\gamma\chi^{(1)} \\ &- g^{\mu\gamma}R^\lambda{}_{\gamma\mu\sigma}\nabla_\nu\nabla_\lambda\chi^{(1)} \ . \end{aligned} \tag{B.17}$$

One more application of Eq. B.39 converts Eq. B.17 into

$$\begin{aligned} g^{\mu\gamma}\nabla_\mu\nabla_\sigma\nabla_\nu\nabla_\gamma\chi^{(1)} &= g^{\mu\gamma}\nabla_\sigma\nabla_\nu\nabla_\mu\nabla_\gamma\chi^{(1)} \\ &- g^{\mu\gamma}\nabla_\sigma\left(R^\lambda{}_{\gamma\mu\nu}\nabla_\lambda\chi^{(1)}\right) \\ &- g^{\mu\gamma}R^\lambda{}_{\nu\mu\sigma}\nabla_\lambda\nabla_\gamma\chi^{(1)} \\ &- g^{\mu\gamma}R^\lambda{}_{\gamma\mu\sigma}\nabla_\nu\nabla_\lambda\chi^{(1)} \ . \end{aligned} \tag{B.18}$$

Using the expression of the Riemann tensor in two dimensions Eq. B.44, we obtain

$$\begin{aligned} g^{\mu\gamma}R^\lambda{}_{\nu\mu\sigma}\nabla_\lambda\nabla_\gamma\chi^{(1)} &= Kg_{\nu\sigma}\Delta\chi^{(1)} - K\nabla_\sigma\nabla_\nu\chi^{(1)} \\ g^{\mu\gamma}R^\lambda{}_{\gamma\mu\sigma}\nabla_\nu\nabla_\lambda\chi^{(1)} &= -K\nabla_\nu\nabla_\sigma\chi^{(1)} \ . \end{aligned} \tag{B.19}$$

and

$$g^{\mu\gamma}\nabla_\sigma\left(R^\lambda{}_{\gamma\mu\nu}\nabla_\lambda\chi^{(1)}\right) = -\nabla_\sigma K\nabla_\nu\chi^{(1)} - K\nabla_\sigma\nabla_\nu\chi^{(1)}. \tag{B.20}$$

Also

$$\begin{aligned} g^{\mu\gamma}\nabla_\mu\left(R^\lambda{}_{\sigma\gamma\nu}\nabla_\lambda\chi^{(1)}\right) &= g_{\sigma\nu}g^{\mu\lambda}\nabla_\mu K\nabla_\lambda\chi^{(1)} \\ &- \nabla_\sigma K\nabla_\nu\chi^{(1)} \\ &+ g_{\sigma\nu}K\Delta\chi^{(1)} \\ &- K\nabla_\sigma\nabla_\nu\chi^{(1)} \end{aligned} \tag{B.21}$$

Collecting all these terms, Eq. B.15

$$\begin{aligned} -Y\nabla_\mu\Gamma^{\mu(1)}_{\nu\sigma} &= 2\nabla_\sigma\nabla_\nu\chi^{(1)} - g_{\sigma\nu}\Delta^2\chi^{(1)} - \\ &- (1+\nu_P)\Big[\nabla_\sigma\nabla_\nu\Delta\chi^{(1)} + 2K\nabla_\sigma\nabla_\nu\chi^{(1)} + \\ &+ g_{\sigma\nu}g^{\mu\lambda}\nabla_\mu K\nabla_\lambda\chi^{(1)}\Big] \end{aligned} \tag{B.22}$$

The next quantity to compute is

$$\begin{aligned} -Y\nabla_\nu\Gamma^{\mu(1)}_{\mu\sigma} &= \nabla_\nu\nabla_\sigma\Delta\chi^{(1)} - (1+\nu_P)g^{\mu\gamma}\nabla_\nu\nabla_\mu\nabla_\sigma\nabla_\gamma\chi^{(1)} \\ &+ 2\nabla_\nu\nabla_\sigma\Delta\chi^{(1)} - (1+\nu_P)g^{\mu\gamma}\nabla_\nu\nabla_\sigma\nabla_\mu\nabla_\gamma\chi^{(1)} \\ &- \nabla_\nu\nabla_\sigma\Delta\chi^{(1)} + (1+\nu_P)g^{\mu\gamma}\nabla_\nu\nabla_\mu\nabla_\gamma\nabla_\sigma\chi^{(1)} \end{aligned} \tag{B.23}$$

that immediately leads to

$$-Y\nabla_\nu\Gamma^{\mu(1)}_{\mu\sigma} = 2\nabla_\sigma\nabla_\nu\Delta\chi^{(1)} - (1+\nu_P)\nabla_\nu\nabla_\sigma\chi^{(1)} \tag{B.24}$$

Therefore, the Ricci tensor is

$$\begin{aligned}\bar{R}_{\sigma\nu} &= R_{\sigma\nu} + \frac{1}{Y}\Big(g_{\sigma\nu}\Delta^2\chi^{(1)} + \\ &+ (1+\nu_P)\left[2K\nabla_\sigma\nabla_\nu\chi^{(1)} + g_{\sigma\nu}g^{\mu\lambda}\nabla_\mu\chi^{(1)}\nabla_\lambda K\right]\Big) \end{aligned} \tag{B.25}$$

Finally, the scalar curvature is obtained as the trace of the Ricci tensor, hence

$$\bar{K} = K + \frac{1}{Y}\left(\Delta^2\chi^{(1)} + 2K\Delta\chi^{(1)} + (1+\nu_p)g^{\mu\lambda}\nabla_\mu K\nabla_\lambda\chi^{(1)}\right) . \tag{B.26}$$

B.4 Elastic energy in the target frame

Our starting point is Eq. 5.43, which for the sake of reference we repeat here:

$$\begin{aligned}F &= \frac{1}{2Y}\int d^2u\sqrt{g}\left[(\Delta\chi^{(1)})^2 + \right. \\ &+ \left.\frac{(1+\nu_P)}{g}\epsilon^{\alpha\sigma}\epsilon^{\rho\beta}\nabla_\alpha\nabla_\beta\chi^{(1)}\nabla_\rho\nabla_\sigma\chi^{(1)}\right]. \end{aligned} \tag{B.27}$$

We now focus on the second term. Using Eq. 5.30 this term becomes

$$\epsilon^{\alpha\sigma}\epsilon^{\rho\beta}\nabla_\alpha\nabla_\beta\chi^{(1)}\nabla_\rho\nabla_\sigma\chi^{(1)} = g\left[\nabla_\alpha\nabla_\beta\chi^{(1)}\nabla^\alpha\nabla^\beta\chi^{(1)} - (\Delta\chi^{(1)})^2\right] . \tag{B.28}$$

Making further use of Eq. B.36, allows to prove the following identity

$$\begin{aligned}&\sqrt{g}T^{\alpha\beta}\nabla_\alpha\nabla_\beta\chi^{(1)} \\ =\ &\partial_\alpha\left(\sqrt{g}T^{\alpha\beta}\nabla_\beta\chi^{(1)}\right) - \sqrt{g}\nabla_\alpha T^{\alpha\beta}\nabla_\beta\chi^{(1)} \\ =\ &\partial_\alpha\left(\sqrt{g}T^{\alpha\beta}\nabla_\beta\chi^{(1)}\right) - \sqrt{g}\nabla_\alpha(g^{\alpha\beta}\Delta\chi^{(1)})\nabla_\beta\chi^{(1)} - \\ -\ &\sqrt{g}Kg^{\beta\alpha}\nabla_\alpha\chi^{(1)}\nabla_\beta\chi^{(1)} \end{aligned} \tag{B.29}$$

where $T^{\alpha\beta} = \nabla^\alpha \nabla^\beta \chi^{(1)}$. Note that

$$\begin{aligned}
\nabla_\alpha T^{\alpha\beta} &= \nabla_\alpha g^{\alpha\rho} g^{\beta\nu} \nabla_\rho \nabla_\nu \chi^{(1)} = g^{\beta\nu} g^{\alpha\rho} \nabla_\alpha \nabla_\rho \nabla_\nu \chi^{(1)} \\
&= g^{\beta\nu} g^{\alpha\rho} \nabla_\nu \nabla_\alpha \nabla_\rho \chi^{(1)} - g^{\beta\nu} g^{\alpha\rho} R^\lambda{}_{\rho\alpha\nu} \nabla_\lambda \chi^{(1)} \\
&= g^{\beta\alpha} \nabla_\alpha \Delta \chi^{(1)} + K g^{\beta\alpha} \nabla_\alpha \chi^{(1)} \qquad \text{(B.30)}
\end{aligned}$$

Here, we have used the identity Eq. B.40.

Using the same operations, it is

$$\begin{aligned}
&\sqrt{g} \nabla_\alpha (g^{\alpha\beta} \Delta \chi^{(1)}) \nabla_\beta \chi^{(1)} \\
&= \partial_\alpha \left(\sqrt{g} \Delta \chi^{(1)} g^{\alpha\beta} \nabla_\beta \chi^{(1)} \right) - \sqrt{g} (\Delta \chi^{(1)})^2 \ . \qquad \text{(B.31)}
\end{aligned}$$

Hence, the second term in Eq. B.27 becomes

$$-\frac{1+\nu_p}{2Y} \int d^2u \sqrt{g} K g^{\alpha\beta} \nabla_\alpha \chi^{(1)} \nabla_\beta \chi^{(1)} \qquad \text{(B.32)}$$

plus a total derivative

$$\begin{aligned}
&\frac{1+\nu_p}{2Y} \int d^2u \partial_\alpha \left[\sqrt{g} \left(T^{\alpha\beta} \nabla_\beta - \Delta \chi^{(1)} g^{\alpha\beta} \nabla_\beta \right) \chi^{(1)} \right] \\
= \ &-\frac{1+\nu_p}{2Y} \int d^2u \partial_\alpha \left[\sqrt{g} \sigma^{\alpha\beta} \nabla_\beta \chi^{(1)} \right] \ , \qquad \text{(B.33)}
\end{aligned}$$

where use has been made of the definition of the stress tensor, see Eq. 5.42. The above integral contributes only at the boundary, leading to the contribution

$$-\frac{1+\nu_p}{2Y} \oint dx^\rho \sqrt{g} \epsilon_{\rho\alpha} \sigma^{\alpha\beta} \nabla_\beta \chi^{(1)}. \qquad \text{(B.34)}$$

For a spherical cap, the above equation is

$$\frac{1+\nu_p}{2Y} \oint d\theta \sqrt{g} \sigma^{r\beta} \nabla_\beta \chi^{(1)}. \qquad \text{(B.35)}$$

and therefore, in the absence of line tension vanishes by the boundary condition $\sigma^{r\beta} = 0$, $\beta = r, \theta$ at the boundary.

B.5 General formulas in Riemannian geometry

B.5.1 Useful identities

The following results apply for any metric $g_{\mu\nu}$ in any dimension, unless further restrictions are stated.

$$\frac{1}{2}\partial_\mu(\log g) = \Gamma^\rho_{\mu\rho} \ . \tag{B.36}$$

The last equation can be written also as

$$\frac{1}{\sqrt{g}}\partial_\mu(\sqrt{g}) = \Gamma^\rho_{\mu\rho} \ . \tag{B.37}$$

Another relation involving Christoffel symbols is

$$g^{\rho\gamma}\Gamma^\nu_{\rho\gamma} = -\frac{1}{\sqrt{g}}\partial_\gamma(\sqrt{g}g^{\gamma\nu}) \ . \tag{B.38}$$

The following relation, involving the Riemann tensor is

$$[\nabla_\mu, \nabla_\nu]V^\rho = R^\rho{}_{\lambda\mu\nu}V^\lambda \ . \tag{B.39}$$

The same relation exists for forms as well, namely

$$[\nabla_\mu, \nabla_\nu]W_{\rho\gamma} = -R^\lambda{}_{\rho\mu\nu}W_{\lambda\gamma} - R^\lambda{}_{\gamma\mu\nu}W_{\rho\lambda} \tag{B.40}$$

Finally, the Ricci and scalar curvature are defined as

$$R_{\mu\nu} = R^\lambda{}_{\mu\lambda\nu} \qquad R = g^{\mu\nu}R_{\mu\nu} \tag{B.41}$$

The equations from here onwards are valid in two dimensions only:

$$\frac{1}{g}\epsilon^{\alpha\rho}\epsilon^{\mu\nu} = g^{\alpha\mu}g^{\rho\nu} - g^{\alpha\nu}g^{\rho\mu} \ . \tag{B.42}$$

$$g^{\alpha\beta} = \frac{1}{g}\epsilon^{\alpha\rho}\epsilon^{\beta\sigma}g_{\rho\sigma} \ . \tag{B.43}$$

And, the Riemann tensor is

$$R_{\rho\lambda\mu\nu} = K\left(g_{\rho\mu}g_{\lambda\nu} - g_{\rho\nu}g_{\lambda\mu}\right) \ , \tag{B.44}$$

where $K = R/2$ is the Gaussian curvature.

B.5.2 Expansion around a given metric

From the incompatibility expansion Eq. 5.38 it is

$$\bar{\Gamma}^{\rho}_{\mu\alpha} = \Gamma^{\rho}_{\mu\alpha} + \eta\Gamma^{\rho(1)}_{\mu\alpha} + \eta^2\Gamma^{\rho(2)}_{\mu\alpha} + \cdots \tag{B.45}$$

here, the η value is just a formal quantity that allows to keep track of the different orders in the expansion.

The compatibility of the connection with the metric implies

$$\begin{aligned} \nabla_\mu g_{\alpha\beta} &= 0 \\ \bar{\nabla}_\mu \bar{g}_{\alpha\beta} &= 0 \end{aligned} \tag{B.46}$$

This last equation, in explicit terms is

$$\bar{\nabla}_\mu \bar{g}_{\alpha\beta} = \frac{\partial \bar{g}_{\alpha\beta}}{\partial x_\mu} - \bar{\Gamma}^{\rho}_{\mu\alpha}\bar{g}_{\rho\beta} - \bar{\Gamma}^{\rho}_{\mu\beta}\bar{g}_{\alpha\rho} = 0. \tag{B.47}$$

Introducing the expansion Eq. B.45 into the previous equation leads to

$$\begin{aligned} \nabla_\mu g_{\alpha\beta} + \eta\left(\nabla_\mu g^{(1)}_{\alpha\beta} - \Gamma^{\rho(1)}_{\mu\alpha}g_{\rho\beta} - \Gamma^{\rho(1)}_{\mu\beta}g_{\alpha\rho}\right) \quad + \\ \eta^2\left(\nabla_\mu g^{(2)}_{\alpha\beta} - \Gamma^{\rho(2)}_{\mu\alpha}g_{\rho\beta} - \Gamma^{\rho(2)}_{\mu\beta}g_{\alpha\rho} - \Gamma^{\rho(1)}_{\mu\alpha}g^{(1)}_{\rho\beta} - \Gamma^{\rho(1)}_{\mu\beta}g^{(1)}_{\alpha\rho}\right) \end{aligned} \tag{B.48}$$

which immediately leads to the identities

$$\begin{aligned}
\nabla_\mu g^{(1)}_{\alpha\beta} - \Gamma^{\rho(1)}_{\mu\alpha} g_{\rho\beta} - \Gamma^{\rho(1)}_{\mu\beta} g_{\alpha\rho} &= 0 \\
\nabla_\mu g^{(2)}_{\alpha\beta} - \Gamma^{\rho(2)}_{\mu\alpha} g_{\rho\beta} - \Gamma^{\rho(2)}_{\mu\beta} g_{\alpha\rho} - \Gamma^{\rho(1)}_{\mu\alpha} g^{(1)}_{\rho\beta} - \Gamma^{\rho(1)}_{\mu\beta} g^{(1)}_{\alpha\rho} &= 0
\end{aligned}$$

with solutions

$$\Gamma^{\rho(1)}_{\mu\alpha} = \frac{g^{\rho\beta}}{2}\left(\nabla_\mu g^{(1)}_{\alpha\beta} + \nabla_\alpha g^{(1)}_{\beta\mu} - \nabla_\beta g^{(1)}_{\mu\alpha}\right) \tag{B.49}$$

and

$$\Gamma^{\rho(2)}_{\mu\alpha} = \frac{g^{\rho\beta}}{2}\left(\nabla_\mu g^{(2)}_{\alpha\beta} + \nabla_\alpha g^{(2)}_{\beta\mu} - \nabla_\beta g^{(2)}_{\mu\alpha}\right) - g^{\rho\beta}\Gamma^{\gamma(1)}_{\mu\alpha} g^{(1)}_{\gamma\beta} \tag{B.50}$$

These expressions allow to compute the Riemann tensor, defined from

$$\bar{R}^\rho{}_{\sigma\mu\nu} = \partial_\mu \bar{\Gamma}^\rho_{\nu\sigma} - \partial_\nu \bar{\Gamma}^\rho_{\mu\sigma} + \bar{\Gamma}^\rho_{\mu\lambda}\bar{\Gamma}^\lambda_{\nu\sigma} - \bar{\Gamma}^\rho_{\nu\lambda}\bar{\Gamma}^\lambda_{\mu\sigma} \ . \tag{B.51}$$

Inserting the terms in Eq. B.49 and Eq. B.50 after some algebra it leads to

$$\begin{aligned}
\bar{R}^\rho{}_{\sigma\mu\nu} &= R^\rho{}_{\sigma\mu\nu} + \eta\left(\nabla_\mu \Gamma^{\rho(1)}_{\nu\sigma} - \nabla_\nu \Gamma^{\rho(1)}_{\mu\sigma}\right) + \\
&+ \eta^2\left(\nabla_\mu \Gamma^{\rho(2)}_{\nu\sigma} - \nabla_\nu \Gamma^{\rho(2)}_{\mu\sigma} + \Gamma^{\rho(1)}_{\mu\lambda}\Gamma^{\lambda(1)}_{\nu\sigma} - \Gamma^{\rho(1)}_{\nu\lambda}\Gamma^{\lambda(1)}_{\mu\sigma}\right) \ .
\end{aligned} \tag{B.52}$$

The Ricci tensor is

$$\begin{aligned}
\bar{R}_{\sigma\nu} &= R_{\sigma\nu} + \eta\left(\nabla_\mu \Gamma^{\mu(1)}_{\nu\sigma} - \nabla_\nu \Gamma^{\mu(1)}_{\mu\sigma}\right) + \\
&+ \eta^2\left(\nabla_\mu \Gamma^{\mu(2)}_{\nu\sigma} - \nabla_\nu \Gamma^{\mu(2)}_{\mu\sigma} + \Gamma^{\mu(1)}_{\mu\lambda}\Gamma^{\lambda(1)}_{\nu\sigma} - \Gamma^{\mu(1)}_{\nu\lambda}\Gamma^{\lambda(1)}_{\mu\sigma}\right) \ .
\end{aligned} \tag{B.53}$$

Appendix C

Appendix: Elastic energy for spherical cap

C.1 Elastic energy in continuum model

In this section we provide the detailed calculations for the elastic energy term(F_c^l) in continuum model, Eqs. 10 and 11 given in the text. We define the elastic free energy as

$$F_c^l = \frac{1}{2K_0}\int d^2\mathbf{x}\sqrt{g}\,(\Delta\chi)^2 \ , \tag{C.1}$$

where $g_{\mu\nu}$ is the metric of the surface. The Laplacian(Δ) is then defined as $\frac{1}{\sqrt{g}}\partial_\mu\left(g^{\mu\nu}\partial_\nu\right)$. For a spherical surface (Fig. C.1), the metric tensor and the laplacian operator are $ds^2 = dr^2 + R^2\sin^2(\frac{r}{R})d\phi^2$ and $\Delta = \frac{1}{\sin(\frac{r}{R})}\partial_r\left(\sin(\frac{r}{R})\partial_r\right) + \frac{1}{R^2\sin^2(\frac{r}{R})}\partial_{\phi\phi}$, respectively. The Airy Stress function χ satisfies

$$\frac{1}{K_0}\Delta^2\chi(\mathbf{x}) = s(\mathbf{x}) - K(\mathbf{x}). \tag{C.2}$$

with $s(\mathbf{x}) = \sum_{i=1}^{N} \frac{q_i}{\sqrt{g}} \delta(\mathbf{x} - \mathbf{x}_i)$ the disclination density and $K(\mathbf{x}) = \frac{1}{R^2}$ gaussian curvature. We seek the solutions of χ subject to the stress free boundary conditions, $\sigma^{rr} = \sigma^{\phi r} = 0$. Following the defination of the stress tensor, the boundary conditions are then

$$\sigma^{rr} = \frac{1}{R} \cot(\frac{r}{R}) \partial_r \chi + \frac{1}{R^2 \sin^2(\frac{r}{R})} \partial_{\phi\phi} \chi = 0 \tag{C.3}$$

$$\sigma^{\phi r} = -\frac{1}{R \sin(\frac{r}{R})} \partial_r \left(\frac{1}{R \sin(\frac{r}{R})} \partial_\phi \chi \right) = 0 \tag{C.4}$$

at $r = R\theta_m = R_m$.

Constructing the green function

$$\Delta^2 G(\mathbf{x}, \mathbf{x}_i) = \frac{1}{\sqrt{g}} \delta(\mathbf{x} - \mathbf{x}_i), \tag{C.5}$$

subject to the dirichlet ($G(R_m, r_i) = 0$) and stress free boundary conditions given in Eqs. (C.3) and (C.4), we find the airy stress function can be written as the integral of the green function with the source field

$$\begin{aligned} \chi(\mathbf{x}) &= K_0 \int d^2\mathbf{x}' \; G(\mathbf{x}, \mathbf{x}') \left(s(\mathbf{x}') - K(\mathbf{x}') \right) \\ &= K_0 R^2 \left(\sum_{i=1}^{N} q_i G(\mathbf{x}, \mathbf{x}_i) - \int d^2\mathbf{x}' \; G(\mathbf{x}, \mathbf{x}') \right) \\ &= K_0 R^2 \left(\sum_{i=1}^{N} q_i G(\mathbf{x}, \mathbf{x}_i) - \Omega(\mathbf{x}) \right), \end{aligned} \tag{C.6}$$

where $\mathbf{x}$ has been rescaled in the unit of R and $\Omega(\mathbf{x}) \equiv \int d^2\mathbf{x}' \; G(\mathbf{x}, \mathbf{x}')$. Thus we have

$$\Delta^2 \Omega(\mathbf{x}) = 1. \tag{C.7}$$

Integrating the free energy in Eq. (C.1) by parts and using the green function G, we find

$$\begin{aligned} F_c^l &= \frac{K_0 R^2}{2} \int d^2\mathbf{x} d^2\mathbf{y} \left[(K(\mathbf{x}) - s(\mathbf{x}))G(\mathbf{x},\mathbf{y})(K(\mathbf{y}) - s(\mathbf{y})) \right] \\ &= \frac{K_0 R^2}{2} \left(\int d^2\mathbf{x}\ \Omega(\mathbf{x}) - \sum_{i=1}^{N} 2q_i\ \Omega(\mathbf{x}_i) + \sum_{i=1}^{N}\sum_{j=1}^{N} q_i q_j G(\mathbf{x}_i,\mathbf{x}_j) \right) \\ &= E_0(\theta_m) + \sum_{i=1}^{N} q_i \hat{E}_{0d}(\mathbf{x}_i,\theta_m) + \sum_{i=1}^{N}\sum_{j=1}^{N} q_i q_j \hat{E}_{dd}(\mathbf{x}_i,\mathbf{x}_j,\theta_m) \\ &= E_0(\theta_m) + \sum_{i=1}^{N} E_{0d}(\mathbf{x}_i,\theta_m) + \sum_{i=1}^{N} E_{self}(\mathbf{x}_i) + \sum_{i=1}^{N}\sum_{j>i}^{N} E_{dd}(\mathbf{x}_i,\mathbf{x}_j) \end{aligned} \tag{C.8}$$

where the first term in Eq. (C.8) describes the gaussian curvature self energy, the second term corresponds to disclination-gaussian curvature interaction, the third term denotes disclination self-energy and the last term is the disclination-disclination interaction energy. In the next section we solve the green function $G(\mathbf{x}_i,\mathbf{x}_j)$ and $\Omega(\mathbf{x})$ for when there exists only one disclination at the center of a spherical cap and then solve it for when it is placed off center.

C.1.1 Center Disclination

We solve Eqs. (C.5)-(C.7) for a radially symmetric system when we only have one disclination at the center of a spherical cap ($r_i = 0$). We find

$$2\pi G(r,0) = \mathrm{Li}_2(-\tan^2(\frac{r}{2})) + \log(1+\tan^2(\frac{r}{2}))\log(\tan(\frac{r}{2})) + u \tag{C.9}$$

$$\Omega(r) = \mathrm{Li}_2(-\tan^2(\frac{r}{2})) + \frac{1}{2}\log(1+\tan^2(\frac{r}{2}))^2 + u \tag{C.10}$$

where Li_2 is a polylogarithm $\mathrm{Li}_2(x) = \sum_{n=1}^{\infty} \frac{x^n}{n^2}$ and u, the homogeneous solution of biharmonic equation $\Delta^2 u = 0$, is given by

$$u = C + D \log(1 + \tan^2(\frac{r}{2})) \tag{C.11}$$

Applying the boundary conditions Eqs. (C.3)-(C.4), $G(\theta_m, 0) = 0$ and $\Omega(\theta_m) = 0$, we find

$$\begin{aligned} 2\pi G(r,0) =& \mathrm{Li}_2(-\tan^2(\frac{r}{2})) + \log(1+\tan^2(\frac{r}{2}))\log(\tan(\frac{r}{2})) \\ &+ 2\log(\cos(\frac{r}{2}))\left(\cot^2(\frac{\theta_m}{2})\log(\cos(\frac{\theta_m}{2})) + \log(\sin(\frac{\theta_m}{2}))\right) \\ &- \mathrm{Li}_2(-\tan^2(\frac{\theta_m}{2})) - \log(1+\tan^2(\frac{\theta_m}{2}))\log(\tan(\frac{\theta_m}{2})) \\ &- 2\log(\cos(\frac{\theta_m}{2})\left(\cot^2(\frac{\theta_m}{2})\log(\cos(\frac{\theta_m}{2})) + \log(\sin(\frac{\theta_m}{2}))\right) \end{aligned} \tag{C.12}$$

and

$$\begin{aligned} &\Omega(r) \\ &= \mathrm{Li}_2(-\tan(\frac{r}{2})^2) + \frac{1}{2}\log(1+\tan^2(\frac{r}{2}))^2 + \log(1+\tan^2(\frac{r}{2}))\cot^2(\frac{\theta_m}{2})\log(1+\tan^2(\frac{\theta_m}{2})) \\ &- \mathrm{Li}_2(-\tan(\frac{\theta_m}{2})^2) - \frac{1}{2}\log(1+\tan^2(\frac{\theta_m}{2}))^2 - \log(1+\tan^2(\frac{\theta_m}{2}))\cot^2(\frac{\theta_m}{2})\log(1+\tan^2(\frac{\theta_m}{2})) \end{aligned} \tag{C.13}$$

We will employ the expressions for $G(r,0)$ and $\Omega(r)$ to calculate the free energy of the system given in Methods section.

C.1.2 Off-center disclination

We now consider an off-center disclination. In this case, the gaussian curvature contribution $\Omega(r)$ remains as in the previous section but the green function $G(\mathbf{x}, \mathbf{x}_i)$ can be

obtained using the function Γ as follows,

$$\Delta\Gamma(\mathbf{x},\mathbf{x}_i) = \frac{1}{\sqrt{g}}\delta(\mathbf{x}-\mathbf{x}_i) \tag{C.14}$$

$$\Delta G(\mathbf{x},\mathbf{x}_i) = \Gamma(\mathbf{x},\mathbf{x}_i). \tag{C.15}$$

Expressing $\Gamma(\mathbf{x},\mathbf{x}_i)$ as the sum of eigenstates, we have

$$2\pi\Gamma(\mathbf{x},\mathbf{x}_i) = \log(\tan(\frac{r_>}{2})) - \sum_{n=1}^{\infty}\frac{1}{n}\frac{\tan^n(\frac{r_<}{2})}{\tan^n(\frac{r_>}{2})}\cos(n\phi), \tag{C.16}$$

which we insert in Eq. (C.15). Then we find

$$\begin{aligned}
&2\pi G(\mathbf{x},\mathbf{x}_i)\\
=&\mathrm{Li}_2(-\tan^2(\frac{r_>}{2})) + \log(\tan(\frac{r_>}{2}))\left(\log(1+\tan^2(\frac{r_>}{2})) + \log(1+\tan^2(\frac{r_<}{2})\right)\\
&+\sum_{n=1}^{\infty}\frac{1}{n}\left(\frac{1}{n}\frac{\tan^n(\frac{r_<}{2})}{\tan^n(\frac{r_>}{2})} - H_n(\cot(\frac{r_>}{2}))\tan^n(\frac{r_<}{2}) - \cot^n(\frac{r_>}{2})H_n(\tan(\frac{r_<}{2}))\right)\cos(n\phi)\\
&+U(\mathbf{x})
\end{aligned} \tag{C.17}$$

where $r_<$ and $r_>$ correspond to min(r,r_i) and max(r,r_i) respectively. The function $U(\mathbf{x})$ denotes the homogenous solution of biharmonic(Δ^2) operator,

$$U(\mathbf{x}) = c_0 + d_0\log(1+\tan(\frac{r}{2})^2) + \sum_{n=1}^{\infty}\frac{1}{n}\left(c_n\tan(\frac{r}{2})^n + d_nH_n(\tan(\frac{r}{2}))\right)\cos(n\phi) \tag{C.18}$$

with H_n the basis function of the biharmonic operator that is given by

$$H_n(x) = \frac{x^{2+n}}{n}\left(\frac{1}{1+x^2} - \frac{1}{1+n}{}_2F_1\left(2,1+n,2+n,-x^2\right)\right), \tag{C.19}$$

where ${}_2F_1$ is the hypergeometric function with $\frac{1}{1+n}{}_2F_1(2,1+n,2+n,x) = \sum_{i=0}^{\infty}\frac{i+1}{n+i+1}x^i$. Applying the boundary conditions Eqs. (C.3)-(C.4) and $G(\theta_m,r_i)=0$, we obtain the coef-

ficients in Eq. (C.18) as

$$
\begin{aligned}
d_0 &= -\log(b) + \frac{1}{2}\left(1+b^{-2}\right)\log\left(\frac{1+b^2}{1+x\rho^2}\right) \\
c_0 &= -\mathrm{Li}_2(-b^2) - \log(b)\left(\log(1+b^2)+\log(1+x\rho^2)\right) - d_0\log(1+b^2) \\
d_n &= \frac{1-\left(1+b^{-2}\right)x\rho^{-n}nH_n(x\rho)}{1-(1+b^{-2})\,b^{-n}nH_n(b)}\left(\frac{x\rho}{b}\right)^n b^{-n} \\
c_n &= \frac{b^{-2n}}{n\left(b^{2+n}-(1+b^2)nH_n(b)\right)} \\
&\quad\left(x\rho^n\Big(-b^{2+n}+nH_n(b)+b^n nH_n(b^{-1})\left(b^{2+n}-(1+b^2)nH_n(b)\right)\Big)+b^{2+n}nH_n(x\rho)\right)
\end{aligned}
\tag{C.20}
$$

where $b=\tan(\frac{\theta_m}{2})$ and $x\rho=\tan(\frac{r_i}{2})$.

C.2 Energy contourPlots

Using $G(\mathbf{x},\mathbf{x}_i)$ and $\Omega(\mathbf{x})$ in Eqs. (C.17) and (C.13) respectively, we calculate the elastic energies due to the Gaussian curvature-disclination interaction (E_{0d}) and disclination self-energy (E_{self}) as given in Eq. (C.8). The contourplot of the elastic free energy for E_{0d} and E_{self} as a function of the location of the disclination in the shell is illustrated in Fig. C.2. Similar to the 1-D case shown in Fig. 3, the minimum energy due to disclination-Gaussian interaction is at the center of the shell Fig. C.2(a) and related to the disclination self-energy is at the edge Fig. C.2(b). While the Gaussian curvature attracts the disclination to the center of the shell, the defect self-energy pushes it towards the boundary. The addition of these two interactions gives rise to a minimum energy, which is off the center of the shell. Figure C.2(c) illustrates the contourplot of the energy of the interaction between two disclinations (E_{dd}). The first disclination (the white ball in Fig. C.2(c)) is placed at the

minimum of $E_{0d} + E_{self}$ but the second one is located at the minimum of $E_{0d} + E_{self} + E_{dd}$. While the curvature-disclination interaction and disclination self-energy determine the number of pentamers in the growing shell, the repulsion between the disclinations distribute them at the vertices of an icosahedron. In this work, we calculated the interaction of Gaussian curvature with disclination and disclination self-energy in the presence of an edge for the first time.

C.3 Bending and stretching energies

Figure C.3 illustrates the bending energy vs. the number of trimers. While there is a huge drop in the stretching energy for the formation of each pentamer (Fig.5), we see almost no difference in the bending energy between the formation of a pentamer and a hexamer as the shell grows. Note that the drops in the stretching energy other than the marked ones in Fig. 5 indicate the positions in which three or four trimers buckle out making the system ready for the assembly of a pentamer. At the later steps, when one or two trimers will be added to the growing pentamers, the stretching energy further decreases in the marked drops, revealing the formation of a complete pentamer.

We emphasize that at large FvK (γ), the triangles remain more or less equilateral during the growth process but the shell easily bends away from the preferred curvature. In fact the magnitude of bending energy is one order of magnitude larger than stretching energy because of the deviation of dihedral angle between the proteins from the preferred one. In the simulations the bending energy was necessary to facilitate the buckling of pentamers at the right position.

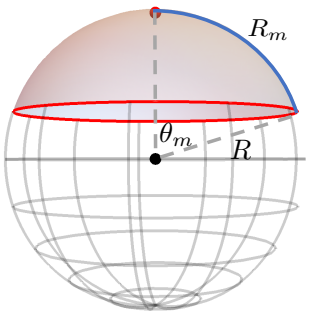

Figure C.1: A spherical cap with geodesic size R_m and radius R, the cap center is marked as a red dot on the top.

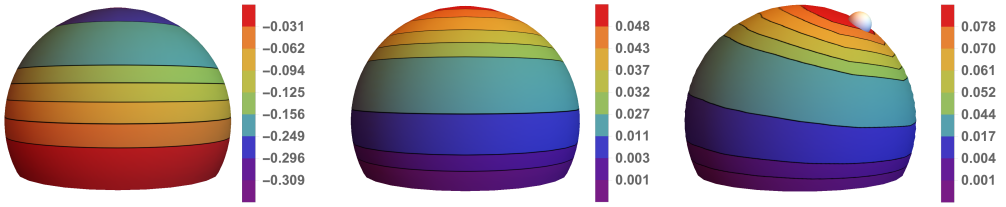

(a) E_{0d}, equation (C.8) (b) E_{self}, equation (C.8) (c) E_{dd}, equation (C.8)

Figure C.2: The contourplots of (a) Gaussian Curvature-Disclination interaction energy; (b) Disclination self-energy; (c) Disclination interaction energy.

In the absence of bending rigidity, the pentamers became deformed to release their stress to their neighboring hexamers. It is interesting to note that in our system when the spontaneous radius is much smaller than the core radius, the difference between the bending energy for a pentamer and a hexamer is not considerable. We find that at high γ the bending energy does not play any roles in the preference between pentamers and hexamers in the shell and the location of pentamers are completely controlled by the stretching energy as it is the case in the elasticity theory.

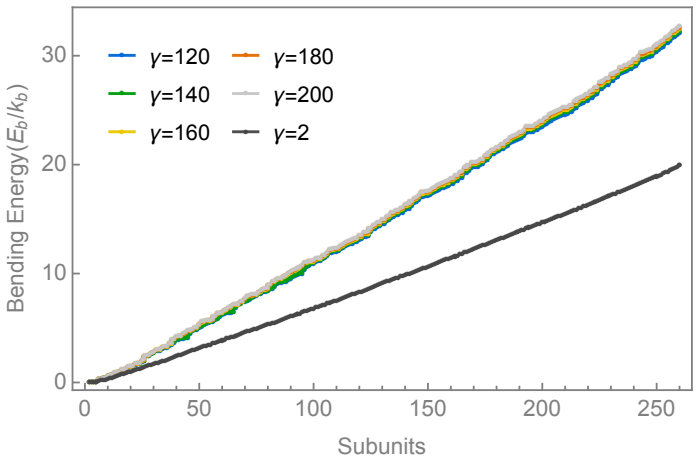

Figure C.3: The bending energy of a T=13 shell as a function of triangular subunits.